

# **Morphological and Structural Modification of Silicon, Titanium and Iron Oxides by Plasma Enhanced Chemical Vapor Deposition for Solar Water Splitting**

## **Inaugural-Dissertation**

zur Erlangung des Doktorgrades

der Mathematisch-Naturwissenschaftlichen Fakultät

der Universität zu Köln



vorgelegt von

**Myeongwhun Pyeon**

aus Yeonggwang, Süd Korea

Köln, 2018

Die vorliegende Arbeit wurde im Zeitraum von April 2014 bis October 2018 am Lehrstuhl für Anorganische und Materialchemie an der Universität zu Köln unter Anleitung von Prof. Dr. Sanjay Mathur angefertigt.

Berichterstatter: Prof. Dr. Sanjay Mathur  
Prof. Dr. Mathias Wickleder  
Prof. Dr. Taejin Hwang

Vorsitzender: Prof. Dr. Klas Lindfors

Tag der mündlichen Prüfung: 23.11.2018

*Dedicated to my parents*





## Acknowledgement

I thank Prof. Dr. Sanjay Mathur for his admission to PhD study in AK Mathur. He has been providing me priceless opportunities and encouragement not only as a supervisor but also as a mentor. I believe that great atmosphere in the working group reflects his warmth and friendly eagerness for discussing with students. In the same breath, my special gratitude goes to Prof. Dr. Taejin Hwang whom I respect in scientific and in philosophical standpoints. I owe him lots of patience he made to educate and to inspire me. I appreciate Prof. Dr. Mathias Wickleder for being an examiner willingly of my thesis despite very late request. It is my great honor to have Prof. Dr. Sanjay Mathur (supervisor), Prof. Dr. Taejin Hwang (co-supervisor) and Prof. Dr. Mathias Wickleder (examiner) as a committee for my PhD defense.

Dr. Yakup Gönüllü deserves to be highly acknowledged who was willing to be a friend of people working in the group rather than a colleague or a leader. His organization skill and scientific experience on PECVD and metal oxides helped me plan experimental works and sorting data well in the beginning of my study. I appreciate Dr. Ashish Lepcha for his hospitality and sacrifice he showed whenever I need some help, which let me feel like home and keep up with my works throughout my stay in AK Mathur. His invitations to dinner were always great where we could build intimate relationship having nice conversation on daily life, cultural background and of course research works, etc. Besides, I would like to thank Dr. Corinna Hegemann, Dr. Lisa Czypiel and Dr. Thomas Fischer for their dedication to organization.

Specifically in research works, Dr. Meng Wang was an outstanding researcher who led me to the concept of PEC water splitting. Thanks to him, I could reach the field with fewer obstacles. I also must acknowledge Dr. Meenal Deo and Mr. Mehmet Gürsoy who actively participated in the subgroup, called plasma group. Dr. Deo supported my works by advising on scientific and technical aspects with full of responsibility. Mr. Gürsoy who has excellent understanding on PECVD shared his precious experience and knowledge with us, which led to meaningful achievement in magnets-assisted PECVD for  $\text{Fe}_2\text{O}_3$  and  $\text{SiO}_x$  films. Moreover, I would like to thank Dr. Tero-Petri Ruoko who introduced a new and a strong tool to verify kinetics of photocarriers which is TAS (transient absorption spectroscopy). Based on his experience and specialty on TAS, we could obtain better insights and possibility for further works in PEC water splitting. All of these collaborative works were realized by being active international characteristics of the working group. An additional remark goes to Ms. Nürgül Tosun who arranged microscopic analyses, Ms. Ruth Bruker for contribution to SEM images with full of skills and experience, technicians working in the Werkstatt (it is so shameful for me not to know

their names) for fabricating experimental equipment with excellence and Mr. Mustafa Demirbilek the Werkmeister for maintaining facilities.

I can't miss to mention about friends working together under the name of AK Mathur especially in the plasma lab. Mr. Alexander Möllmann and Mr. Danny Bialuschewski perform excellent works based on their enthusiasm and hard working. In addition, I should express my gratitude to Dr. Jennifer Leduc, Ms. Aida Raauf, Mr. Eunhwan Jung, Rishabh Garg, Senol Öz, Karim Arroub, Ufuk Atamtürk, and Daniel Stadler for having fun and serious conversation which was one of the most important aspects staying abroad. I also admire their attitude to integrate people into the group without any prejudice, which I could feel comfortable and rely on them. Although I can't name the entire group members, I must show my best respect to colleagues who volunteer to operate analytic tools, study themselves about the machines and support the others. And I would like to acknowledge the members who sacrificed and volunteered to take responsibilities for inner/outer events that impressed numerous people. Within those scientific activities, I witnessed a lot of positive aspects of colleagues like integration, altruism and self-motivation, which affected me.

Most of all, my family, the reason why I am, I thank you.

## Abstract

This study focuses on the synthesis and modification of silicon, titanium and iron oxides using PECVD (plasma enhanced chemical vapor deposition). The motivation for this work resulted from the urgent need for alternative energy solutions and demand for functional coatings. More detailed, thin films of semiconducting metal oxides ( $\alpha$ -Fe<sub>2</sub>O<sub>3</sub>, TiO<sub>2</sub>) were prepared and modified to be applied for photoelectrochemical (PEC) water splitting (WS) that has been regarded as a promising approach to eco-friendly generation of hydrogen from sea water. Main efforts were put into the improvement of the PEC performance, represented by photocurrent density and onset potential in linear scan voltammetry by three experimental strategies.

The first strategy was to fabricate heterojunctions, consisting of Fe<sub>2</sub>O<sub>3</sub> (representing  $\alpha$ -Fe<sub>2</sub>O<sub>3</sub>, hematite) and TiO<sub>2</sub>. A distinctive structure of heterojunction photoelectrodes was fabricated by employing a striped metal mask during PECVD, in order to achieve macrostructuring. Double-layered TiO<sub>2</sub>//Fe<sub>2</sub>O<sub>3</sub>:FTO electrodes with striped structures of TiO<sub>2</sub> and triple-layered Fe<sub>2</sub>O<sub>3</sub>//TiO<sub>2</sub>//Fe<sub>2</sub>O<sub>3</sub>:FTO electrodes with orthogonal cross-bar structures were produced. Although neither the double nor triple layered electrodes showed enhanced PEC performances compared to single-layered Fe<sub>2</sub>O<sub>3</sub> photoanodes, most likely due to increased interfacial recombination, patterned double and triple heterojunction photoelectrodes showed increased photocurrent densities of approximately 17 % and 56 %, respectively, compared to the unpatterned ones (0.58 mA/cm<sup>2</sup> for the double layer and 0.25 mA/cm<sup>2</sup> for the triple layer at 1.23 V vs. reversible hydrogen electrode (RHE)). This could be attributed to the coexistence of Fe<sub>2</sub>O<sub>3</sub> and TiO<sub>2</sub> with characteristic surface morphology in contact with electrolyte as well as to unintentional elemental doping. In addition to the planar heterojunction, hematite nanorods synthesized by a hydrothermal route were covered with PECVD grown TiO<sub>2</sub>. It appeared that TiO<sub>2</sub> nanoparticles were homogeneously deposited onto hematite nanorods, forming a core-shell structure with a Fe<sub>2</sub>O<sub>3</sub>-TiO<sub>2</sub> heterojunction. The highest photocurrent density (0.74 mA/cm<sup>2</sup> at 1.5 V vs. RHE) was obtained from a Fe<sub>2</sub>O<sub>3</sub>-TiO<sub>2</sub> photoanode where the deposition time for TiO<sub>2</sub> was 30 min, while the pristine hematite nanorods and the PECVD grown TiO<sub>2</sub> (30 min) photoanodes exhibited 0.19 mA/cm<sup>2</sup> and 0.04 mA/cm<sup>2</sup>, respectively, under similar electrochemical conditions.

Secondly, PECVD was utilized not only to produce hematite thin film but also to alter surface chemical states by post-deposition treatment of films with oxygen plasma, followed by rapid thermal treatment (referred as “short annealing” in the main text). Oxygen plasma treatments led to significant changes in the microstructure of hematite surfaces, exhibiting that growth of

particles was promoted as the treatment duration increased. Moreover, XPS (X-ray photoelectron spectroscopy) analysis used to investigate the surface chemical states, showed a shift to lower binding energies, suggesting an interaction of Fe atoms with surface adsorbed oxygen species. These altered chemical states at the hematite surface seemed to be responsible for the onset potential shift in anodic direction that indicates sluggish oxidation on the surface, which was corroborated by TAS (transient absorption spectroscopy). However, upon the rapid thermal treatment, recovery in chemical shift was observed, indicating rearrangement of surface states and suggesting that chemisorbed oxygen is not an integral part of the hematite lattice. More interestingly, the onset potential moved back to the level of the untreated photoanode. It strongly indicates that the surface chemical states are highly influential forwards water oxidation at the photoanode/electrolyte interface in PEC water splitting reaction. Furthermore, an increased photocurrent density of up to 2-fold was observed from the sample treated with both oxygen plasma and short annealing compared to the pristine hematite photoanode.

The third approach involved modulation of plasma using external magnetic fields in PECVD processes based on the assumption that plasma confinement would affect the deposition kinetics. As a result, morphology and crystallinity of the hematite films remarkably varied depending on the characteristics of applied magnetic fields such as magnetic polarity and geometry of magnetic flux. In this study, two types of magnets having different geometry, i.e. rod-type and disk-type, were employed and the investigation was conducted to evaluate the influence of magnetic fields. The hematite film deposited under the repulsive magnetic field induced by the rod-type magnets produced hematite particles orthogonally grown to the substrate, leading to a porous structure while the one produced under the attractive field showed a densely packed surface and a suppressed (110) crystalline plane, revealed by XRD (X-ray diffraction) analysis. Likewise, when the hematite films were grown in the presence of magnet stacks (3 disk-type magnets), more compact surfaces were obtained than the reference hematite sample. Moreover, in terms of crystallinity, samples grown in repulsive and attractive arrangement of magnets exhibited (104) plane became dominant with decreased signal of the (110) plane. When those hematite films were evaluated for PEC water splitting, the ones deposited under magnetic fields regardless of types of magnets used, generated more photocurrent density than the reference hematite photoanode did. Thus, the effectiveness of magnet-assisted PECVD for modulating hematite films was verified as a potential strategy to improve the functional performance of photoanode materials. In another set of experiment, PECVD processes with hexamethyldisiloxane ( $C_6H_{18}OSi_2$ , HMDSO) for the deposition of  $SiO_2$ -like ( $SiO_x$  or  $SiOC$ ) films was conducted. It was revealed that the deposition rate and surface hydrophobicity of  $SiO_x$

was increased with magnet-assisted PECVD. A higher water contact angle was attributed to increased surface roughness and surface carbon content revealed by AFM (atomic force microscopy) and XPS, respectively.



## Kurzzusammenfassung

Diese Arbeit konzentriert sich auf die Synthese und Modifizierung von Silizium-, Titan- und Eisenoxiden mithilfe von PECVD (Plasma-gestützte chemische Gasphasenabscheidung), um den Bedarf an alternativen Energielösungen abzudecken, sowie die Anforderungen an funktionellen Beschichtungen zu untersuchen. Im Detail wurden dünne Filme aus halbleitenden Metalloxiden ( $\alpha$ - $\text{Fe}_2\text{O}_3$ ,  $\text{TiO}_2$ ) hergestellt und modifiziert, um sie für die photoelektrochemische (PEC) Wasserspaltung (WS) zu verwenden, die als vielversprechender Ansatz zur umweltfreundlichen Wasserstoffherzeugung ausgehend von Meerwasser angesehen wird. Im Fokus stand die Verbesserung der PEC-Leistung basierend auf der Photostromdichte und dem Onset-Potential in der linearen Scan-Voltammetrie, welches durch drei experimentelle Strategien überprüft werden sollte.

Die erste Strategie war die Herstellung von Heteroübergängen, bestehend aus  $\text{Fe}_2\text{O}_3$  ( $\alpha$ - $\text{Fe}_2\text{O}_3$ , Hämatit) und  $\text{TiO}_2$ . Photoelektroden mit Makrostrukturierung und einem Heteroübergang wurden hergestellt, indem eine gestreifte Metallmaske während des PECVD-Prozesses verwendet wurde. Eine doppelschichtige  $\text{TiO}_2//\text{Fe}_2\text{O}_3$ :FTO-Elektrode mit einer Streifenstruktur aus  $\text{TiO}_2$  und eine dreischichtige  $\text{Fe}_2\text{O}_3//\text{TiO}_2//\text{Fe}_2\text{O}_3$ :FTO-Elektrode mit orthogonaler Crossbar-Struktur wurden hergestellt. Obwohl weder die Doppel- noch die Dreifachschicht eine verbesserte PEC-Leistung im Vergleich zu einer monolagigen  $\text{Fe}_2\text{O}_3$ -Photoanode aufwiesen, zeigten die strukturierten Doppel- und Dreifach-Heteroübergangs-Photoelektroden eine erhöhte Photostromdichte bei 1,23 V gegenüber einer reversiblen Wasserstoffelektrode (RHE) von etwa 17% und 56% im Vergleich zu den unstrukturierten ( $0,58 \text{ mA/cm}^2$  für die Doppelschicht und  $0,25 \text{ mA/cm}^2$  für die Dreifachschicht). Dies könnte auf die Koexistenz von  $\text{Fe}_2\text{O}_3$  und  $\text{TiO}_2$  mit der charakteristischen Oberflächenmorphologie im Kontakt mit dem Elektrolyten sowie auf die unbeabsichtigte Elementdotierung zurückgeführt werden. Zusätzlich zum planaren Heteroübergang wurden Hämatit-Nanostäbe, die auf hydrothermale Weg synthetisiert wurden, mit PECVD-gewachsenem  $\text{TiO}_2$  bedeckt. Es zeigte sich, dass  $\text{TiO}_2$ -Nanopartikel homogen auf Hämatit-Nanostäbchen abgeschieden wurden und eine Kern-Schalen-Struktur von  $\text{Fe}_2\text{O}_3$ - $\text{TiO}_2$ -Heteroübergängen gebildet wurden. Die höchste Photostromdichte ( $0,74 \text{ mA/cm}^2$  bei 1,5 V gegen RHE) wurde mit einer  $\text{Fe}_2\text{O}_3$ - $\text{TiO}_2$ -Photoanode erhalten, wobei die Abscheidungszeit für  $\text{TiO}_2$  30 Minuten betrug, während die unbehandelten Hämatit-Nanostäbe und die PECVD-hergestellten  $\text{TiO}_2$ -Photoanoden (30 min) nur  $0,19 \text{ mA/cm}^2$  bzw.  $0,04 \text{ mA/cm}^2$  unter ähnlichen elektrochemischen Bedingungen zeigten.

Zweitens wurde die PECVD auch zur Veränderung der chemischen Oberflächenzustände durch

Nachbehandlung von Filmen mit Sauerstoffplasma eingesetzt. Das Sauerstoffplasma führte zu einer signifikanten Veränderung der Mikrostruktur an der Hämatitoberfläche, was zeigte, dass das Wachstum von Partikeln mit zunehmender Behandlungsdauer gefördert wurde. Darüber hinaus zeigten chemische Zustände, die durch XPS (Röntgenphotoelektronenspektroskopie) detektiert wurden, eine Verschiebung zu einer niedrigeren Bindungsenergie, was auf eine Wechselwirkung von Fe-Atomen mit oberflächenadsorbierten Sauerstoffspezien hindeutet. Diese veränderten chemischen Zustände der Hämatitoberfläche scheinen für die Verschiebung des Anfangspotentials in anodischer Richtung verantwortlich zu sein, was auf eine träge Oxidation an der Oberfläche hindeutet, welches durch TAS (Transiente Absorptionsspektroskopie) bestätigt wurde. Bei der schnellen thermischen Nachbehandlung wurde jedoch eine Erholung der chemischen Verschiebung beobachtet, was auf eine Umordnung der Oberflächenzustände hindeutet und nahelegt, dass chemisorbierter Sauerstoff kein integraler Bestandteil des Hämatitgitters ist. Interessanterweise bewegte sich das Anfangspotential wieder auf das Niveau der unbehandelten Photoanode. Es zeigt stark an, dass die chemischen Zustände der Oberfläche einen starken Einfluss auf die Wasseroxidation an der Photoanoden/Elektrolyt-Grenzfläche in der PEC-Wasserspaltungsreaktion haben. Darüber hinaus wurde eine erhöhte Photostromdichte von bis zu dem 2-fachen Wert der Probe beobachtet, die sowohl mit Sauerstoffplasma als auch mit kurzem Tempern behandelt wurde, verglichen mit der ursprünglichen Hämatit-Photoanode.

Der dritte Ansatz umfasste die Modulation von Plasma unter Verwendung von externen Magnetfeldern in den PECVD-Prozessen basierend auf der Annahme, dass die Plasmaeingrenzung die Ablagerungskinetik beeinflussen würde. Als ein Ergebnis variierten die Morphologie und die Kristallinität der Hämatitfilme bemerkenswert in Abhängigkeit von den Eigenschaften der angelegten Magnetfelder, wie der magnetischen Polarität und der Geometrie des magnetischen Flusses. In dieser Studie wurden zwei Arten von Magneten mit unterschiedlichen Geometrien, d. h. Stab- und Scheiben-Typ, verwendet, und die Untersuchung wurde durchgeführt, um den Einfluss von Magnetfeldern zu bewerten. Die Abscheidung, welche unter dem von den stabförmigen Magneten induzierten abstoßenden Magnetfeld durchgeführt wurde, erzeugte Hämatitpartikel, die orthogonal zum Substrat gewachsen waren, was zu der Bildung einer porösen Struktur führte, während bei dem Anziehungsfeld eine dicht gepackte Oberfläche mit unterdrückter (110)-Kristallebene entstand, welches durch XRD Analyse (Röntgenbeugung) gezeigt wurde. Wenn die Hämatitfilme in Gegenwart von Magnetstapeln (3 Scheibenmagnete) gezüchtet wurden, wurden in ähnlicher Weise kompaktere Oberflächen erhalten als bei der Referenz-Hämatitprobe. Im Hinblick auf die Kristallinität zeigten Proben, die in einer abstoßenden und anziehenden Anordnung von Magneten gewachsen waren eine



dominantere (104)-Ebene und ein verringerten Signal in der (110)-Ebene. Diese Hämatitfilme wurde mittels PEC-Wasserspaltung untersucht und die Elektroden, welche unter Magnetfeldern (unabhängig von der Art der verwendeten Magnete) abgeschieden wurden, wiesen eine höhere Photostromdichte als die der Referenz-Hämatit-Photoanode auf. Daher wurde die Wirksamkeit der magnetunterstützten PECVD zur Modulation von Hämatitfilmen als eine mögliche Strategie zur Verbesserung der funktionellen Leistungsfähigkeit von Photoanodenmaterialien verifiziert. In einer anderen Versuchsreihe wurde ein PECVD-Prozess mit Hexamethyldisiloxan für einen  $\text{SiO}_2$ -ähnlichen ( $\text{SiO}_x$  oder  $\text{SiOC}$ ) Film durchgeführt. Es zeigte sich, dass die Ablagerungsrate und Oberflächenhydrophobie von  $\text{SiO}_x$  mit magnetunterstütztem PECVD erhöht wurde. Ein höherer Wasserkontaktwinkel wurde der erhöhten Oberflächenrauigkeit und dem Oberflächenkohlenstoffgehalt zugeschrieben, die durch AFM (Rasterkraftmikroskopie) bzw. XPS detektiert wurden.



# Table of Contents

1	Introduction.....	1
1.1	Chemical vapor deposition (CVD).....	4
1.2	Plasma enhanced chemical vapor deposition (PECVD).....	7
1.2.1	Plasma characteristics .....	7
1.2.2	Gas phase plasma-chemical reactions .....	8
1.2.3	Surface reactions in PECVD .....	13
1.2.4	Applications of PECVD grown thin films.....	13
1.3	Metal oxides .....	17
1.3.1	Functional metal oxides synthesized by a variety of routes .....	17
1.3.2	Targeted applications of PECVD metal oxides.....	18
1.4	Photoelectrochemical (PEC) water splitting .....	19
1.4.1	Mechanism and background.....	19
1.4.2	State-of-the-art and literature survey .....	21
1.5	Hydrophobic coatings .....	24
1.5.1	Mechanism and background.....	24
1.5.2	State-of-the-art and literature survey .....	25
2	Synthesis of heterojunction $\text{Fe}_2\text{O}_3$ - $\text{TiO}_2$ films .....	29
2.1	Motivation and background.....	29
2.1.1	Design of heterojunction $\text{Fe}_2\text{O}_3$ - $\text{TiO}_2$ photoelectrodes for PEC water splitting .....	29
2.1.2	Core-shell structured heterojunction of $\text{Fe}_2\text{O}_3$ - $\text{TiO}_2$ photoelectrodes .....	39
3	Surface modification of hematite films by post-treatments .....	43
3.1	Motivation and background .....	43
3.1.1	Post-synthesis treatment of hematite via oxygen plasma.....	43

3.1.2	Post-synthesis treatment of hematite via argon plasma.....	52
4	In-situ modulation of thin film growth by external magnetic fields .....	57
4.1	Motivation and background.....	57
4.1.1	Effect of magnetic fields on a magnetic oxide (hematite) .....	58
4.1.2	Effect of magnetic fields on a non-magnetic oxide ( $\text{SiO}_x$ ) .....	70
5	Experimental .....	77
5.1	Synthesis of heterojunction $\text{Fe}_2\text{O}_3$ - $\text{TiO}_2$ films.....	77
5.1.1	Design of heterojunction $\text{Fe}_2\text{O}_3$ - $\text{TiO}_2$ photoelectrodes for PEC water splitting .....	77
5.1.2	Core-shell structured heterojunction of $\text{Fe}_2\text{O}_3$ - $\text{TiO}_2$ photoelectrodes .....	78
5.2	Surface modification of hematite films by post-treatment.....	79
5.2.1	Post-treatments of hematite films via oxygen/argon plasma and short annealing.....	79
5.3	In-situ modification of metal oxides via magnetic field assisted PECVD .....	79
5.3.1	Effect of magnetic fields on hematite photoelectrodes for PEC water splitting .....	79
5.3.2	Effect of magnetic fields on surface functionality of $\text{SiO}_x$ films .....	82
5.4	Characterization methods .....	82
6	Summary and outlook .....	85
7	References.....	89
8	Indices.....	101
8.1	Figures index.....	101
8.2	Schemes index .....	103
8.3	Tables index .....	104
9	Appendix .....	107
9.1	Abbreviations (in order of appearance).....	107
9.2	Lebenslauf.....	109
9.3	Publication list .....	110

9.4	Presentations.....	111
	Erklärung.....	113

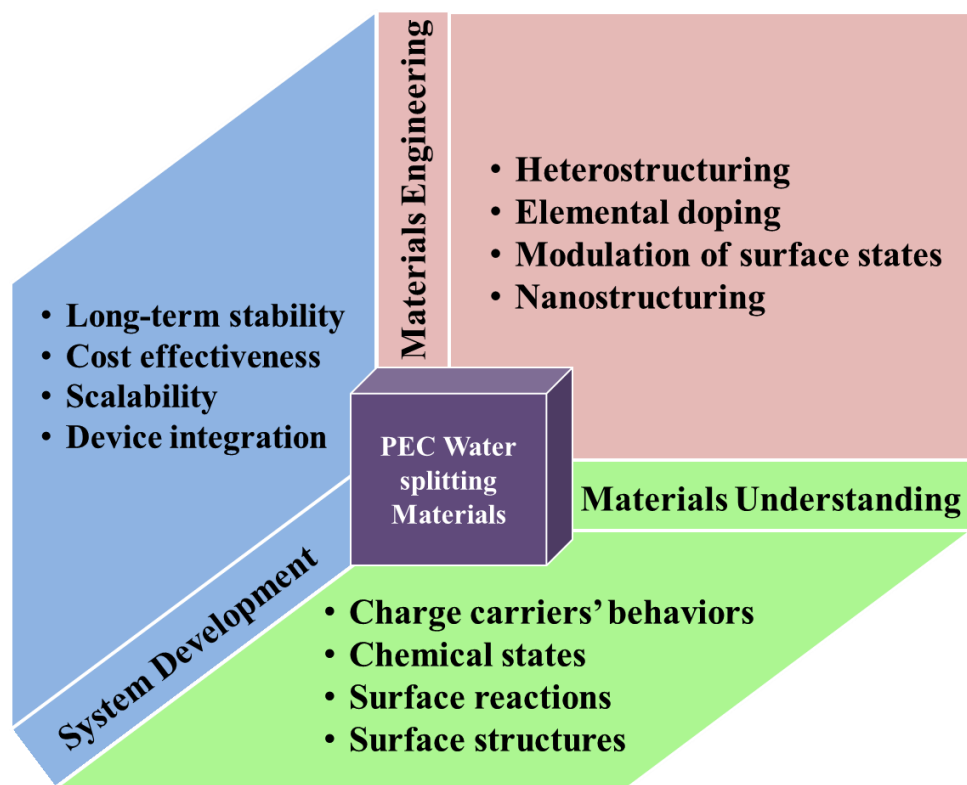


## 1 Introduction

Hydrogen both in industry and research fields has drawn tremendous attention as a promising alternative energy carrier, which enables to store and to distribute sustainable energy sources. Due to its abundance in nature and production of carbon-free by-products, development of technologies attracts and motivates research fields to realize “Hydrogen Economy”<sup>1</sup> in the future.

Currently, over 95 % of hydrogen is produced from fossil-fuels such as natural gas, oil or coal worldwide. For example, hydrogen production in US mainly relies on steam methane reforming and the annual production exceeded 5,000 tons in the industrial marketplace.<sup>2</sup> Upon increasing concern about reducing carbon-based by-products to decelerate air pollution, a breakthrough in development of hydrogen production became an utmost topic.

Solar energy-driven splitting of water is one of the promising methodologies, which utilizes semiconducting materials. The term photoelectrochemical (PEC) water splitting that is widely used is derived from its concept that charge carriers “photo”generated by solar irradiation are involved to “electrochemical” redox reactions that split water molecules into hydrogen and oxygen. To realize an efficient PEC water splitting system, it is necessary to address several prerequisites in materials selection. Since the PEC water splitting system consists of photoelectrodes in contact with aqueous electrolyte under solar irradiation, chemical stability is highly required. The reason for using aqueous electrolyte is due to the fact that pure water with high electrical resistance impedes protons and hydroxide ions to be mobile enough. Typical electrolytes can have wide range of pH.<sup>3</sup> In terms of electronic structures, photoelectrode materials need to possess appropriate energy band gap ( $E_g$ ) to efficiently absorb solar irradiation and their band edges (valence and conduction bands) should position properly (Detailed discussion will be given in 1.4). Scheme 1 depicts several aspects to be considered for development of new photoelectrode materials for PEC water splitting, which describes that the successful expansion in development of the optimum photoelectrodes relies on interplay between understanding, engineering the materials and development of PEC systems.



**Scheme 1 Complex interplay of material properties and device integration in the development of new materials for photoelectrochemical water splitting (PEC-WS) reactions.**

Works in this thesis mainly deal with deposition and modification of metal oxides synthesized by PECVD for PEC water splitting. Thanks to intense efforts delivered in the working group, a major part of works is focused on modification strategy to verify effectiveness of several idea-based approaches on targeted functionalities (PEC water splitting and hydrophobicity for  $\alpha$ - $\text{Fe}_2\text{O}_3$  (hematite) and  $\text{SiO}_x$ , respectively) utilizing a PECVD technique. Thus, this report consists of general descriptions of CVD (chemical vapor deposition) that will provide background information starting from a mechanism of gas phase reactions to form thin films. Then, this will be extended into the PECVD that is one of the modified forms of a conventional thermal CVD. The section providing introduction to PECVD highlights from fundamental plasma chemistry which is essential in plasma reactions to applications of exemplary PECVD grown films. In addition to process-related aspects, following sections will cover the specific applications of PEC water splitting and surface hydrophobicity, which point out state-of-the-art of each application and challenges. Prior to discussions on mechanistic characteristics of gas phase chemical deposition, a comparison of some processes for thin film fabrication is provided in the following sections.

Among a number of processes to produce functional coatings in research and in industry,



PECVD is widely known as an advantageous technique that overcomes several limitations which wet-chemical processes and other gas phase depositions such as PVD (physical vapor deposition) and thermal CVD have faced in synthesis of thin films. For instance, PECVD is a favorable method to deposit thin films on a wide range of substrates including temperature sensitive substrate, e.g. polymer that is not applicable to unmodified CVD due to high temperature process. Besides, substrates with sophisticated geometry can be used in PECVD owing to isotropic chemical reaction in plasma whereas films formation in thermal CVD takes place along a direction of precursor transport, which limits the use of substrates with a complex 3-D structure. Table 1 provides a list of characteristics of typical methods used for film fabrication.<sup>4,5</sup>

**Table 1 A comparison list of various techniques applied for fabrication of thin films.**

Wet-chemical process	PVD	CVD	PECVD
<ul style="list-style-type: none"> <li>• Cost effective</li> <li>• Ease of synthesis for phase pure and composite materials</li> <li>• Low temperature process</li> </ul>	<ul style="list-style-type: none"> <li>• Atomic scale control</li> <li>• No need for toxic precursors</li> </ul>	<ul style="list-style-type: none"> <li>• Favorable for thick films</li> <li>• Not required post-thermal treatment</li> <li>• Simultaneous deposition of multiple precursors</li> </ul>	<ul style="list-style-type: none"> <li>• Low process temperature</li> <li>• Free of substrate selection</li> <li>• High deposition rate</li> <li>• Unique chemical properties of the films</li> <li>• Wide range of precursors</li> <li>• Controllability of film morphology</li> </ul>
<ul style="list-style-type: none"> <li>• Multiple deposition steps required (e.g. spin/dip coatings)</li> <li>• Additional preparation of coating solutions</li> </ul>	<ul style="list-style-type: none"> <li>• High vacuum required</li> <li>• Low deposition rate</li> <li>• Post heat treatment required</li> <li>• Line-of-sight</li> </ul>	<ul style="list-style-type: none"> <li>• Toxic precursors</li> <li>• High process temperature</li> <li>• Substrates limitation</li> </ul>	<ul style="list-style-type: none"> <li>• Expensive</li> <li>• Complex design of precursor feeding apparatus</li> <li>• Residual stress on films</li> <li>• Complicated optimization of process parameters</li> <li>• Amorphous coatings</li> </ul>

Practically, in preparation of photoelectrodes (thin films) for PEC water splitting, facileness and effectiveness of utilizing PECVD process are quite obvious. Especially, while nanoparticles in suspension to be deposited on substrates require additional consideration for film stability, PECVD usually guarantees formation of highly adhesive films on various substrates. This is crucial for films used in PEC water splitting application that the films are immersed in acidic/base aqueous solution under illumination with simulated solar light. Peeling-off of the material from the substrate is of course not preferable. This issue is not about photochemical stability of the material such as dissolution in non-neutral aqueous solution but about process related one.

In the last part of this section, PEC water splitting and hydrophobic coatings will be addressed as specific applications of PECVD metal oxides, which account for main results and discussion of this report.

In Chapter 2, syntheses and characterizations of multi-layered metal oxides consisting of  $\text{Fe}_2\text{O}_3$  and  $\text{TiO}_2$  are presented, which were developed for PEC water splitting. A distinguished study

plan in this report was set to investigate the effect of macropatterning on fabrication of multi-layered heterojunction of  $\text{Fe}_2\text{O}_3/\text{TiO}_2$  by employing a featured mask. Owing to the designed mask, a simple pattern of stripes could be fabricated on substrate (see Scheme 4). From sequential deposition and annealing, double and triple layers with patterns could be fabricated and photoresponses of these heterostructured photoanodes were evaluated and compared with ones without patterns. In addition to planar heterojunctions, 1D (1-dimensional) core-shell heterostructures of  $\text{Fe}_2\text{O}_3\text{-TiO}_2$  were fabricated and their structural effects on PEC water splitting performance were evaluated. Tandem synthesis routes including hydrothermal synthesis and PECVD were employed to fabricate hematite nanorods covered by  $\text{TiO}_2$  shell.

In Chapter 3, chemical modification of as-synthesized hematite films was demonstrated by plasma treatment followed by thermal treatment steps. Actually, this work was derived from several tryouts that focused on PECVD  $\text{SnO}_2$  on hematite film for temperature-driven diffusion of Sn atoms both from top and bottom (substrate) to modulate electronic properties of hematite. We observed that hematite films with additional PECVD of tin(IV) tert-butoxide ( $\text{Sn}[\text{OC}(\text{CH}_3)_3]_4$ ) exhibited superior current-voltage (I-V) characteristics than pure PECVD hematite films despite no sign of  $\text{SnO}_2$  deposition in the reaction chamber. Tracking back to the synthesis procedure, a set of experiment was designed without applying precursor, i.e. only introducing plasma with oxygen gas, for the PECVD process. Characterization of morphology, topology, crystallinity, and chemical states as well as evaluation of the modified hematite films in PEC performance is reported.

In Chapter 4, in-situ modulation of growth of metal oxides ( $\text{Fe}_2\text{O}_3$  and  $\text{SiO}_x$ ) was performed by applying magnetic fields in PECVD processes. Commercially available magnets with two distinguished geometries (rod-type and disk-type) were employed and experimental setup for PECVD was designed accordingly. There was obvious distortion of plasma during processes due to magnets. Influence of the plasma confined by magnets was investigated and their properties were evaluated.

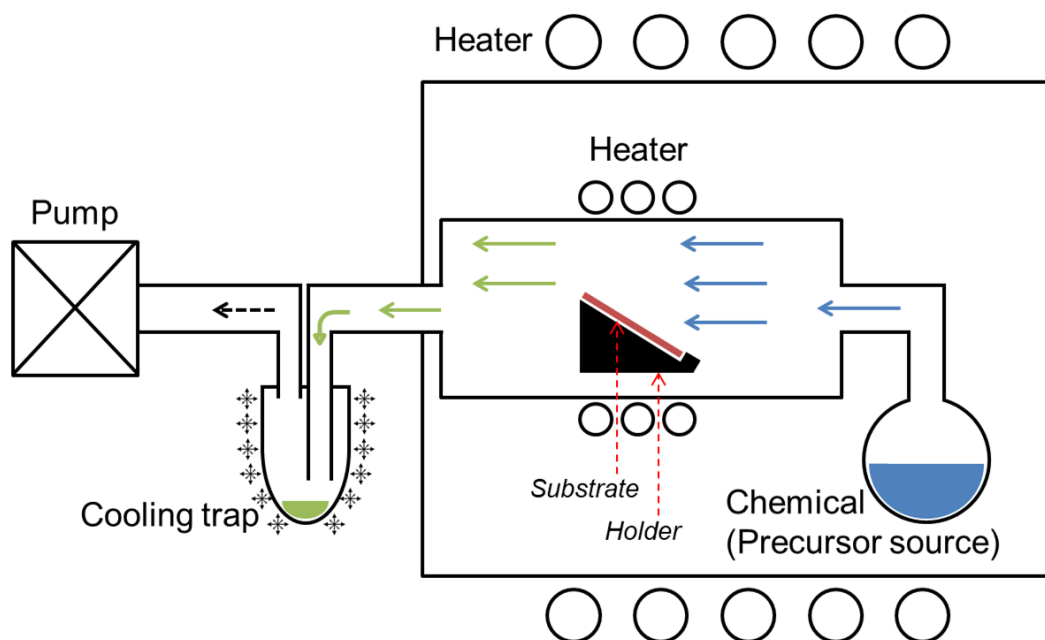
Experimental procedures taken to realize ideas are given in Chapter 5. This Chapter includes materials used, process parameters of PECVD and supplementary Schemes and Tables for clearer descriptions of actual processes.

## 1.1 Chemical vapor deposition (CVD)

Among various material processing means, CVD is a well-established technique that enables to mainly produce thin solid films and is complex involving gas phase chemical reactions and

surface reactions. In terms of processing environment, it is distinguished from solution-based chemical processes since chemical reactions to deposit solid films are initiated in the gas phase. When utilizing liquid or solid precursors in CVD, therefore, significant consideration of precursor choice is required. It leads to great efforts to balance volatility and stability of precursors in molecular design. It can also be differentiated from PVD with respect to type of driving force to activate raw materials and kinetics in film formation. While CVD includes substantial chemical reactions for producing thin films, PVD does not but relies largely on physical kinetics in an operation. Briefly, a target material (source) gets evaporated by various means of energy input such as ion beam, electron beam, plasma, and pulsed laser. Then this vaporized particles become condensed on the electrode to form desired films.<sup>6,7</sup> Scheme 2 illustrates a thermal CVD system that represents a typical set-up of CVD equipment.

The horizontal reaction tube (typically quartz) is placed in an oven that is facilitated for heating up chemical (typically, several hundreds of degrees Celsius) and isolating the reaction tube to sustain steady transport of precursor to the substrate. When the precursor takes sufficient thermal energy, it starts to be transported into the reaction tube in a gas phase. Decomposition of precursor molecules takes place driven by thermal energy near the substrate which is locally heated in the reaction tube. Physical/chemical phenomena to form solid films on the substrate can be categorized in several steps:<sup>8</sup> 1) thermally activated precursor molecules react each other in the gas stream, 2) reactive molecular species diffuse through boundary layer and get adsorbed onto the substrate surface, 3) the adsorbed reactants further react with other adsorbent molecules and diffuse on the surface until they lose their energy, 4) nucleation and growth of reactants takes place where they became stable, 5) when the reactants on the substrate still have too high energy or failed to react with other molecules they get desorbed and involved into the out gas stream. The unreacted molecules (marked in green arrows in Scheme 2) should be collected before they reach a pump by cooling traps.



**Scheme 2 An illustration of a typical thermal CVD system.**

There are some variations of CVD that can be classified with respect to several aspects.<sup>9</sup> The first aspect to categorize types of CVD is energy source to decompose precursor molecules. As already introduced plasma enhanced CVD (PECVD) utilizes reactive ions and electrons to drive chemical reaction of precursor fragmentation. Plasma-assisted CVD can be further divided into MWCVD (microwave plasma-assisted CVD) and RPECVD (remote plasma enhanced CVD) depending on energy source addressed to generate plasma and structure of PECVD system, respectively. On the other hand, input energy in photo-assisted CVD is light (photons). The light is irradiated either to precursor molecules or to a substrate for in-situ modification of film growth. Like PECVD, the photo-assisted CVD can be potentially applied to low temperature deposition. The second aspect would be operation condition, represented by a level of vacuum. APCVD (atmospheric pressure CVD) is widely used in industry for large scale and mass production of especially glass coatings due to unnecessariness of vacuum system. Considering characteristics of CVD, the APCVD requires extra attention that unwanted chemical reaction could be involved in an ambient pressure, which leads to development of low pressure gas phase deposition having favorable control in composition and uniformity of films. Typically, LPCVD (low-pressure CVD) and UHVCVD (ultrahigh vacuum CVD) are classified as modern CVD that are operated at sub-atmospheric condition and below  $10^{-6}$  Pa ( $\sim 10^{-8}$  torr), respectively.<sup>10–12</sup> Moreover, a physical status of precursor vapor also assorts CVD types. When the chemical source exhibits insufficient vapor pressure, it can be transported to a substrate with help of ultrasonification. The resultant precursor can form liquid/gas aerosol, named as AACVD (aerosol-assisted CVD). Often

chemicals of liquid phase can be directly injected into a specially designed chamber that enables to vaporize them (direct liquid injection CVD, DLICVD). Then the precursor vapor is eventually transported to a conventional CVD reaction chamber. Figure 1 presents a classification diagram of CVDs as a summary.

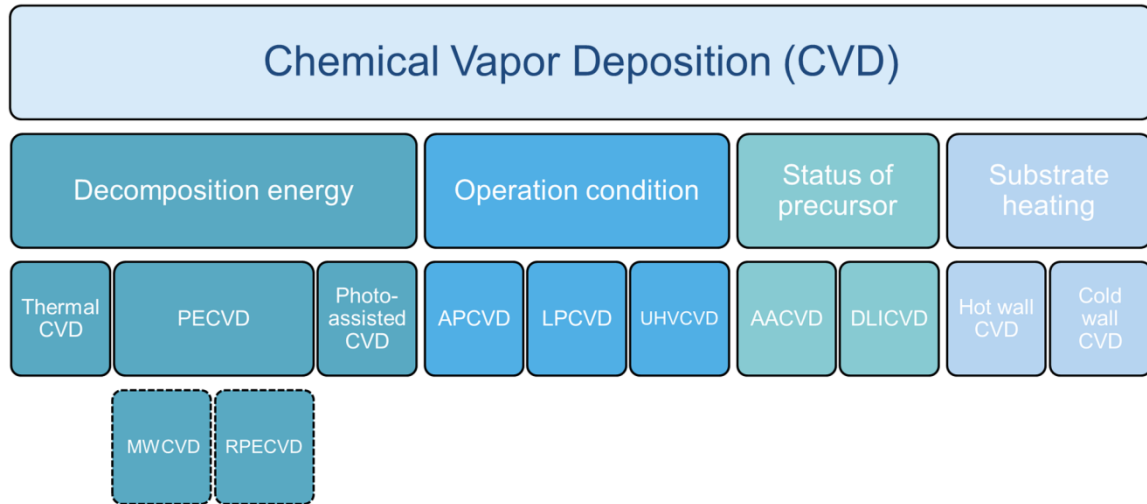


**Figure 1 Classification of various CVD processes.**

## 1.2 Plasma enhanced chemical vapor deposition (PECVD)

### 1.2.1 Plasma characteristics

Plasma enhanced chemical vapor deposition (PECVD or PACVD as plasma-assisted CVD)<sup>13,14</sup> is a mature methodology to produce various types of films that manifest characteristic chemical and/or physical properties both in industry and in academia. As the name implies, plasma is involved in a gas phase chemical deposition. Plasma is the fourth status of matter and the term was originally introduced by an American chemist/physicist Irving Langmuir in 1928, where it was defined as a region containing balanced charges of ions and electrons.<sup>15</sup> Consequently, the resultant space charge is very small due to similar amount of ions in the ionized gas and electrons.

Plasma can be artificially generated by input of energy to ionize gas, producing charged ions and electrons. In general, electric current as energy source is applied to gas that is heated to certain extent since thermal energy is insufficient to discharge gas molecules to form the fourth status of matter. Once the gas molecule is discharged, positive charges and electrons are pulled to a cathode and to an anode, respectively. During this stage, enormous amount of collisions takes place between these charged particles and the number of charged particles rapidly increases due to increased ionization. The ionization of gas medium consists of excitation and relaxation (de-

excitation) of electrons, leading to radiation of characteristic light, which is why color of plasma glow varies depending on the type of plasma forming gas. This ionized gas provides energy to dissociate molecules and promote reaction between molecules and substrate, subsequently forming films in PECVD.

The early demonstration of plasma was dedicated by Sir William Crookes who developed a “glow discharge tube” in 1879.<sup>16,17</sup> He built a glass tube retaining high vacuum and supply electrical current throughout the tube. The actual apparatus designed consists of a metal disk in the middle of the tube that is negatively polarized and two other poles connected to positive terminal that are placed end-to-end of the tube. Upon supplying electrical current along the wire, “dark space” is formed near the both surfaces of the metal disk in the middle. Moreover, one can observe thickness of “dark space” changes as the extent of vacuum varies. This dark space became renowned later as term “plasma” by Langmuir as mentioned above. Prof. Crookes believed that this behavior of dark space reflects mean free path of molecules. When the molecules are in high vacuum, (in other words, very small number of molecules) the length of their mean free path becomes so large that these molecules travel with exceedingly high velocity (energy). However, in the opposite case, molecules have a lot more chance to collide each other with insufficient energy. It, consequently, led to variation in thickness of the dark space depending on vacuum. Of course, characteristics of the molecules in high vacuum should not be regarded ordinarily since these molecules (preferred terminology by Prof. Crookes was gaseous residue) behave differently compared with gas in an ambient condition.

### 1.2.2 Gas phase plasma-chemical reactions

There are chemically active components in plasma-chemical processes and each component plays its characteristic role in a specific process. The chemical reactions in plasma involve ionization/recombination, excitation/relaxation, association/dissociation, and charge transfer. Since these reactions occur between plasma species such as electrons, ions, atoms, molecules, and radicals simultaneously, it is not simple to establish PECVD modeling. Nevertheless, brief introduction to elementary chemical reactions<sup>18</sup> in plasma will be given to understand what happens in the artificial plasma for thin film growth.

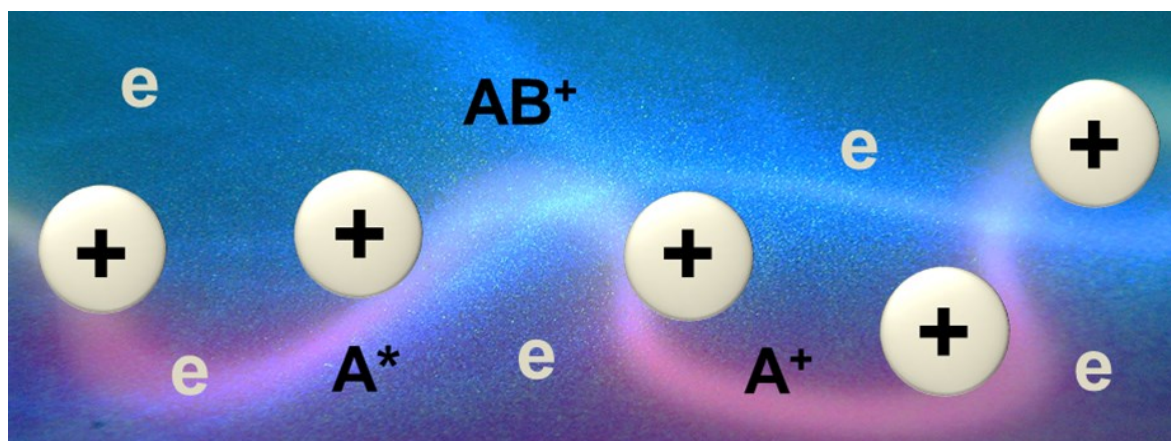
Electrons are usually the first component receiving energy from electric field and initiate chemical reactions with high energy due to small mass and high mobility. This makes a term electron energy distribution function (EEDF,  $f(E)$ ) important to estimate rates of plasma-chemical reactions, which represents the probability density for an electron to have energy  $E$  and can be described as following;

$$f(E) = 2\sqrt{E/\pi(kT_e)^3} \exp(-E/kT_e),$$

where  $k$  is a Boltzmann constant and  $T_e$  is the electron temperature.

The EEDF is largely influenced by the frequency of electric field applied to generate plasma ( $f = \omega/2\pi$ ) in case the field is generated by AC (alternating current). Since the higher frequency, in general, yields higher power efficiency, degrees of ionization and dissociation become more effective in microwave (MW,  $f = 2.45$  GHz) than in radio frequency (RF,  $f = 13.56$  MHz) PECVD.<sup>19</sup>

Moreover, ions (much heavier than electrons) also affect significantly plasma-chemical kinetics due to their high energy. Atoms and radicals contribute to plasma-chemical reactions through taking part in a number of plasma-stimulated processes (e.g. O atoms and OH radicals for oxidation process). Photons generated during plasma-chemical reaction can also play a key role such as plasma light source and UV sterilization of water.<sup>20–23</sup>



**Scheme 3 A scheme of reactive species generated in plasma.**

The first elementary plasma-chemical reaction to be considered is ionization. Ionization is a process that neutral atoms and molecules lose their electrons upon application of external field, producing positive ions. Within ionization, it can be subdivided into several groups depending on plasma-chemical systems as following (Table 2).

1) Direct ionization of neutral and unexcited atoms, radicals, or molecules by single collision with an electron: electrons with high energy collide with other components, which results in non-dissociative or dissociative ionization depending on electron energy (i.e. non-dissociative ionization takes place when “electron energy  $\geq$  ionization potential” and dissociative ionization takes place when “electron energy  $\gg$  ionization potential”).

2) Ionization by heavy particles that involves collision of ion-molecule or ion-atom: very high kinetic energy is required for ions and neutrals to be able to provide ionization (10-100 keV), which is  $\sim 10^3$  more than the ionization potential. If a metastable atom  $A^*$  possesses higher electron excitation energy than the ionization potential of another atom B, collision between these two components lead to ionization process. Another case is associative ionization taking place even though the total electron excitation energy is insufficient. The associative ionization occurs through formation of molecular ion ( $AB^+$ ).

3) Photo-ionization of neutral species: when photon with certain wavelength ( $\lambda$ ) is irradiated on neutral particles A in plasma, A can be ionized. The photon wavelength providing ionization is determined by the equation,  $\lambda \text{ (nm)} = 1,240/I \text{ (eV)}$ , where  $I$  is ionization potential of A. For effective ionization,  $\lambda$  should be usually  $< 100 \text{ nm}$  that is in ultraviolet range.<sup>18</sup>

**Table 2 Classification of ionization processes in plasma (An atomic radical is presented as  $A^*$ ).**

Types of ionizations	Chemical reactions
Direct ionization	$e + AB \rightarrow AB^+ + e + e$ (non-dissociative ionization)
	$e + AB \rightarrow A + B^+ + e + e$ (dissociative ionization)
Ionization by heavy particles	$A^* + B \rightarrow A + B^+ + e$ (Penning ionization)
	$A^* + B \rightarrow AB^+ + e$ (Associative ionization)
	$A^+ + BC \rightarrow AB^+ + C$ (ionization by interchange)
Photo-ionization	$h\nu + A \rightarrow A^+ + e$

Specifically, positive ions play an important role in plasma-chemical reaction. As a counter reaction of ionization, recombination takes place when an electron collides with a positive ion. Since this electron-ion recombination is an exothermic process, there should be certain channels to release energies during the process. The released energy from the recombination contributes to the following reactions.

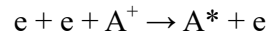
1) Dissociative electron-ion recombination: from the direct impact of electron to a positively charged gas molecule, the released energy from the recombination contributes to dissociation of



an intermediate molecule and to excitation of the dissociated products.



2) Three-body electron-ion recombination: excess energy goes to the kinetic energy of a free electron that participates in the recombination. This additional electron support efficiently the recombination and is much more favorable than ions and neutrals do since those heavy species are unable to accumulate energy fast enough in their kinetic energy. Like the earlier case, the released energy is used to excite the neutralized gas atom.



3) Radiative electron-ion recombination: the recombination energy of electron-ion can yield an intermediate state of an atom and the energy is released in the form of light.

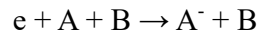


Likewise, negative ions take part in some elementary plasma-chemical reactions either by being collided with other charged particles or by being produced as following.

1) Dissociative electron attachment: dissociation of molecules (reactants) occurs through an intermediate species, initiated by electron impact. The intermediate excited state is not stable so reverse auto-detachment of electron can occur when it does not receive enough energy from electron for dissociation.



2) Three-body electron attachment: when electron collides with two atoms, one of the atoms can be ionized becoming a negative ion. This reaction can occur where the electrons have not enough energy to dissociate molecules and it is a main channel to consume electrons. This makes the three-body electron attachment important in atmospheric discharges.

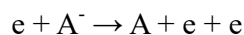


3-1) Associative electron detachment: a reverse reaction of dissociative electron attachment.

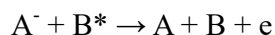


3-2) Electron impact detachment: a negative ion is relaxed by losing its additional electron due to electron impact. This reaction is important when the degree of ionization is high in plasma since the influence of forming of neutral particles by losing electrons would be more sensitive where

there is a plenty of negative ions.



3-3) Detachments driven by collisions between excited particles: when two excited particles collide, electron is detached from a negative ion and the other particle (electronically excited) becomes relaxed. This process occurs when the radical ( $B^*$ ) has higher electronic excitation energy than the electron affinity of A.



In addition to charged particles (electrons and ions), behaviors of neutral species need to be considered since they also play a critical role in a specific condition. These processes take place in various forms such as vibrational excitation, rotational excitation, electronic excitation, and dissociation of molecules by electron impact. Especially for dissociation of molecules, Fridman classified it into 5 groups depending on detailed mechanisms involved and obviously intermediates with varied electronic energy are formed in each mechanism.<sup>18</sup> Giving a general description, the mechanisms can be classified by the excited states from their ground states. Mechanism A and E include excitations to the repulsive states by direct electron impact. The repulsive state is at which molecules are unstable so their potential energy curves do not exhibit minimum points and consequently spontaneous dissociation of molecules occurs. In contrast, when molecules are excited to the attractive states, their energy curves show minimum points and the molecules are stable being combined. However, in plasma environment, energies of molecules excited to attractive states exceed dissociation energy, which leads to dissociation of molecules into fragments. Table 3 lists five mechanisms of dissociation of neutral molecules by electron impact.

**Table 3 Dissociation mechanisms of neutral molecules.**

Dissociation mechanisms	Excited states	Chemical reactions	Remarks
A	Repulsive	$e + AB \rightarrow (AB^-)^*_{rep} \rightarrow A^- + B$	Electron energy $\gg$ Dissociation energy
B	Attractive	$e + AB \rightarrow (AB^-)^*_{att} \rightarrow A^- + B$	Energy of the excited states $>$ Dissociation energy
C	Attractive	$e + AB \rightarrow (AB^-)^*_{att} + h\nu \rightarrow A^- + B$	Radiative transition of the excited states
D	Attractive	$e + AB \rightarrow (AB^-)^*_{att} \rightarrow (AB^-)^*_{rep} \rightarrow A^- + B^*$	Radiationless transition from the attractive states to the repulsive states
E	Repulsive	$e + AB \rightarrow (AB^-)^*_{rep} \rightarrow A^- + B^*$	Highest electron energy required for excitation ensuring dissociation

Now one can expect a counter reaction of the excitation of neutral molecules, which can be described as relaxation. In most of cases, relaxation of molecules is related with surface reaction, determining whether if nucleation/growth of films that are initiated by stabilized species will be taken place or desorption of the species with insufficiently stable molecules will occur. Plasma-chemical reactions with surfaces will be discussed in the following section.

### 1.2.3 Surface reactions in PECVD

From a variety of gas-phase reactions, excited (electronically, vibrationally and rotationally) particles that are transferred to an exposed surface further experience chemical reactions along the surface, which leads to film formation. There exists an interface at the surface in contact with plasma, called plasma sheath. The plasma sheath is electrically non-neutral unlike plasma bulk, which leads to floating potential ( $V_f$ ) within the sheath and its thickness depends on the average electron energy and electron density. Positive ions are diffused through this plasma sheath due to difference between the plasma potential ( $V_p$ ) and  $V_f$  and accelerated to the substrate with a maximum kinetic energy of  $E_{i,max} = e|V_p - V_B| + \Delta E/2$ , where  $V_B$  is biased voltage to the substrate and  $\Delta E/2$  is the term for periodic modulation of the sheath voltage in case, which is dependent on the frequency of plasma power.<sup>19</sup>

### 1.2.4 Applications of PECVD grown thin films

PECVD has emerged as a technology to produce films, overcoming some limitations of conventional gas phase deposition techniques. Thin films with diverse properties such as optical, mechanical, electrical, and thermal properties can be fabricated by PECVD processes.<sup>19</sup> This has led to increased interest in PECVD technique to enhance coating properties for various applications as shown in Table 4.

**Table 4 Various applications of PECVD functional coatings (adapted from Ref.<sup>19</sup>).**

Applications	Examples of devices and film systems
Microelectronics and microsystems	<ul style="list-style-type: none"> <li>• Transistors</li> <li>• Microelectromechanical systems (MEMS)</li> </ul>
Optics, photonics, telecommunications and informative technologies	<ul style="list-style-type: none"> <li>• Optical interference filters (including antireflective (AR) coatings)</li> <li>• Ophthalmic lenses</li> <li>• Optical waveguides</li> <li>• Displays (including barrier coatings)</li> <li>• Decorative (protective) coatings</li> <li>• Optical coatings on plastics</li> <li>• Protective coatings for storage media</li> </ul>
Aerospace and outer space	<ul style="list-style-type: none"> <li>• Protective coatings against solid particle erosion and corrosion</li> <li>• Protection against space environment (atomic oxygen, radiation, thermal cycling, charge accumulation)</li> </ul>
Automotive	<ul style="list-style-type: none"> <li>• Protective coatings for engine components (low friction and wear)</li> <li>• Protective coatings for light assemblies (corrosion resistance)</li> <li>• Protective coatings for fuel distribution (permeation barriers)</li> </ul>
Energy generation and saving	<ul style="list-style-type: none"> <li>• Photovoltaics (amorphous and polycrystalline silicon, AR coatings)</li> <li>• Protective coatings for fuel cells</li> <li>• Corrosion-resistant coatings</li> <li>• Self-cleaning (photocatalytic) surfaces</li> <li>• Smart windows</li> </ul>
Biomedical and pharmaceutical	<ul style="list-style-type: none"> <li>• Protective coatings for implants</li> <li>• Protective coatings for surgical tools</li> <li>• Biocompatible coatings</li> </ul>
Sensors	<ul style="list-style-type: none"> <li>• Miniaturized microphone (mechanoacoustic effects)</li> <li>• Gas and vapor sensors (electrical, optical, and structure-related effects)</li> </ul>
Manufacturing	<ul style="list-style-type: none"> <li>• Protective coatings on cutting tools (high-speed machining, dry machining, machining of nonferrous metals/nonmetals, and composites)</li> <li>• Anti-sticking coatings (e.g. molds)</li> </ul>
Textiles	<ul style="list-style-type: none"> <li>• Hydrophobic coatings</li> <li>• Antiseptic textiles</li> </ul>
Packaging	<ul style="list-style-type: none"> <li>• Barriers against gas and vapor permeation coatings on flexible substrates</li> </ul>

For example, DLC (diamond-like carbon) coating that has been applied to biomedical engineering, optical lenses, silicon solar cells, and so on due to its superior surface characteristics is one of widely spreading thin film systems in industry.<sup>24</sup> DLC forms hybridization of  $sp^2$  (graphitic type) and  $sp^3$  (diamond type). The extent of  $sp^3$  and hydrogenation determines its property, which categorizes DLC into *a*-C (hydrogen-free DLC), *a*-C:H (hydrogenated DLC), *ta*-C (tetrahedral amorphous carbon), and *ta*-C:H (hydrogenated tetrahedral amorphous carbon).<sup>25</sup> By modulating process parameters in PECVD, nature of DLC coatings can be modified and their

properties can be improved.<sup>26–29</sup> Since L. Holland and S. M. Ohja<sup>30</sup> reported about “carbonaceous” coatings through radio frequency (r.f.) plasma consisting of butane ( $C_4H_{10}$ )/Ar. W. Milne<sup>31</sup> demonstrated thin film deposition of polycrystalline diamond through decomposition of  $CH_4$ /Ar gas mixture in r.f. plasma. Following research works have been conveyed and developed for diamond-like coatings that exhibit high resistivity ( $\sim 10^{12} \Omega \cdot cm$ )<sup>32</sup> and refractive index (2.4–2.9).<sup>31</sup> Furthermore, sometimes PECVD for DLC coatings can be combined with other techniques to incorporate dopants such as Fe, Ti, Mo, and W for improving lubrication properties, electrical conductivity, corrosion resistance, and thermal stability.<sup>33–35</sup> Hence, the physical/chemical properties of the resultant coatings can vary by modulating bias voltage, temperature, amount of reactive gas, type of accompanying gases (e.g. Ar,  $H_2$ , He,  $N_2$ ), and a ratio of gas mixture.<sup>36,37</sup> Table 5 lists DLC coatings produced by PECVD.

**Table 5 Various DLC coatings produced by PECVD.**

Materials	Reactive/ additive gases	Control parameters	Target properties	Ref.
<i>a</i> -C:H	$CH_4$ /Ar, He, $N_2$	r.f. power	Electrical resistivity, hardness, friction coefficient	38
Polycrystalline diamond	$CH_4$ /Ar	r.f. power	-	31
<i>a</i> -C:H	$C_2H_2$	Deposition temperature	Electrical conductivity, optical absorption coefficient	39
<i>a</i> -C:H	$C_2H_2/H_2$ , He	Deposition temperature	Adhesion, wear/dielectric strength	40
Ag-DLC	$CH_4$	-	Bactericidal activity	41
Ti doped <i>a</i> -C:H	$CH_4/H_2$ +Ar	-	-	42
<i>a</i> -C:H	$CH_4$ /Ar +HMDSO	r.f. power, HMDSO/ $CH_4$	Microhardness, elastic modulus	43
F doped DLC	$C_2H_2$ /Ar+ $CF_4$	Flow rate of $CF_4$	Protein absorption	44

Another well studied system with PECVD represents silicon-based materials that can be implemented by introducing certain silicon precursors along with additive gases, like hydrocarbons, nitrogen and oxygen to achieve required phases.<sup>45</sup> Silicon carbide (SiC) has been renowned for its excellent mechanical properties and produced in industrial scale since late 1800s to be used as an abrasive. Shortly afterwards, it was used in the first radios as a detector, which opened up an electrical application of SiC followed by demonstration of LEDs (light-

emitting diodes). In addition, SiC can be applied as a protective coating to prevent MEMS (micro-electromechanical systems) from corrosion thanks to its chemical inertness.<sup>46–48</sup> Most frequently, mass production of SiC powders have been conveyed through solid-phase reaction (Acheson method), and yet there are alternative processes to obtain pure SiC or to hybridize with other materials being suggested.<sup>49–52</sup> PECVD is advantageous to synthesize SiC films at low temperature (200 °C) whereas high process temperature of 1500–1600 °C is typically required in the thermal CVD, utilizing silane and hydrocarbons as silicon and carbon precursors, respectively.<sup>53,54</sup> Early studies on PECVD of SiC films have focused on syntheses of polycrystalline/amorphous (*a*-SiC:H) films and their mechanical, electrical and optical properties, depending on various PECVD parameters.<sup>55–57</sup> Moreover, a recent report showed that the silane plasma fragments (SiH<sub>3</sub> and SiH<sub>2</sub>) exhibited selective kinetics towards Si-H termination sites to grow Si in PECVD. A DFT (density functional theory) calculation utilized in the study provides energy barriers of the plasma fragments throughout the reaction pathways, which allowed to estimate and to determine which bonding is favorable for each fragment. It appeared that both silyl (SiH<sub>3</sub>) and silylene (SiH<sub>2</sub>) favor to abstract H from Si-H bondings rather than from C-H bondings although their reaction mechanisms differ. This is intriguing that plasma environment under controlled conditions is not indiscriminate unlike general assumption.<sup>58</sup> Table 6 provides various SiC coatings prepared by PECVD.

**Table 6 Silicon carbide films prepared by PECVD.**

Materials	Reactive/additive gases	Control parameters	Target properties	Ref.
SiC	SiH <sub>4</sub> , C <sub>2</sub> H <sub>4</sub> /Ar	Deposition temperature, power density, SiH <sub>4</sub> /C <sub>2</sub> H <sub>4</sub> ratio	Mechanical properties (intrinsic and thermal stress, tensile stress, Young's modulus), optical properties (refractive index)	59
<i>a</i> -SiC:H	SiH <sub>4</sub> , CH <sub>4</sub> /Ar	-	Dielectric properties (dielectric constant/loss, breakdown voltage)	60
<i>a</i> -SiC	SiH <sub>4</sub> , CH <sub>4</sub>	r.f. power density	Electrical resistivity, Chemical resistivity (dissolution rate), Biocompatibility	53
<i>a</i> -Si <sub>x</sub> C <sub>1-x</sub> :H	SiH <sub>4</sub> , CH <sub>4</sub>	Deposition temperature	-	61
SiC	SiH <sub>4</sub> , CH <sub>4</sub>	-	Optoelectronic properties (refractive index, absorbance)	62

$a\text{-SiC}_x\text{:H}$	$\text{SiH}_4$ , $\text{CH}_4$	$\text{CH}_4/\text{SiH}_4$ ratio, deposition temperature, r.f. power density	Optoelectronic properties (optical band gap, refractive index)	63
$a\text{-SiC:H}$	$\text{CH}_3\text{SiCl}_3$	Substrate temperature	Mechanical properties (nanohardness, elastic modulus, abrasive wear resistance)	64
$a\text{-Si}_x\text{C}_{1-x}\text{:H}$	$\text{SiH}_4$ , $\text{C}_2\text{H}_2$	$\text{SiH}_4/\text{C}_2\text{H}_2$ flow rate	Oxidation behavior in $a\text{-Si}_x\text{C}_{1-x}\text{:H}$ films	65

The last category of materials would be metal oxides that can be synthesized by PECVD. Due to high feasibility of employing appropriate chemicals as metal sources (e.g. organometallics), PECVD has been regarded as a promising approach to fabrication of metal oxide thin films. Further description on metal oxides will be given in the following section to highlight their properties in detail.

### 1.3 Metal oxides

Metal oxides form the largest group in ceramic materials and exhibit several superior properties such as chemical inertness, high temperature properties and high electrical resistivity (except for some oxides like indium oxide and tin oxide).<sup>66</sup> Possibilities to tune their properties have been attracting researchers' tremendous interest for many application areas. There have been a remarkable number of investigations on metal oxides in various application aspects, which reflects their importance and opens up new prospects. Especially, transition metal oxides possess unusual properties due to the unique nature of the outer *d*-electrons. Representative properties of the transition metal oxides can be classified as:<sup>67</sup> 1) electronic properties arisen from charge density waves (e.g.  $\text{K}_{0.3}\text{MoO}_3$ ), charge ordering (e.g.  $\text{Fe}_3\text{O}_4$ ) and defect ordering (e.g.  $\text{Ca}_2\text{Mn}_2\text{O}_5$ ,  $\text{Ca}_2\text{Fe}_2\text{O}_5$ ), 2) magnetic properties from ferromagnetism (e.g.  $\text{CrO}_2$ ,  $\text{La}_{0.5}\text{Sr}_{0.5}\text{MnO}_3$ ) to antiferromagnetism (e.g.  $\text{NiO}$ ,  $\text{LaCrO}_3$ ), 3) switchable orientation states as in ferroelectric (e.g.  $\text{BaTiO}_3$ ,  $\text{KNbO}_3$ ) and ferroelastic (e.g.  $\text{Gd}_2(\text{MoO}_4)_3$ ) materials.

#### 1.3.1 Functional metal oxides synthesized by a variety of routes

Various synthesis methods have been developed to produce metal oxides having desired chemical, physical, and morphological features for various applications. Fabrication of metal oxide thin films can be classified into two main groups: wet (solution-based) processes and dry (vapor-based) processes. Dip-coating,<sup>68</sup> electrospinning,<sup>69</sup> spray coating,<sup>70</sup> and doctor blading<sup>71</sup> can be given as examples of the solution-based techniques. Table 7 lists a recent progress on metal oxide films deposited by wet-chemical processes for applications.

**Table 7 A list of metal oxides synthesized by wet-chemical processes for applications.**

Deposition methods	Materials	Applications	Ref.
Dip-coating	Graphene-Mn <sub>3</sub> O <sub>4</sub> Graphene-Fe <sub>2</sub> O <sub>3</sub>	Lithium-ion battery	72
	TiO <sub>2</sub>	Electrochromic	73
	Graphene oxide	Electrical devices	74
Electro-spinning	La <sub>0.88</sub> Sr <sub>0.12</sub> MnO <sub>3</sub>	Biosensor	75
	Fe <sub>3</sub> O <sub>4</sub>	Biosensor	76
	ZnO	Hybrid solar cell	77
Spray coating	Fe <sub>2</sub> O <sub>3</sub>	Catalytic oxygen evolution and gas sensing	78
	Cu <sub>2</sub> O	Thin-film transistor	79
	Indium-gallium-zinc-oxide (IGZO)	Thin-film transistor	80
Doctor-blading	SnO <sub>2</sub> -ZnO	Dye-sensitized solar cell	81
	ZnO and Al doped ZnO	Polymer solar cell	82
	TiO <sub>2</sub> and ZnO	Dye-sensitized solar cell	83

Despite relative simplicity of the wet processes compared with gas phase deposition, contact with chemical solvents throughout the process can be undesirable. Besides, liquid phase solvents such as polymer binders usually need to be removed. In technical point of view, it can be difficult to handle particles with sizes of less than 100  $\mu\text{m}$  for producing fine films because strong liquid surface tension forces could cause sticking between particles, leading to agglomeration of particles.<sup>84,85</sup> Also, some fragile substrates can be damaged with aggressive solvents used in wet processes. The homogeneous transfer of solvents into corrugated parts of the geometrically complex substrates can be challenging due to the surface tension of liquids, which resulted in poor coating conformity.<sup>86</sup> On the other hand, PECVD offers superior performance in production of conformal coatings thanks to isotropic nature of plasma where concurrent chemical reactions take place. Plasma-driven chemical reactions are effective as long as the transfer of precursor into the reaction chamber is guaranteed.

### 1.3.2 Targeted applications of PECVD metal oxides

The properties of the metal oxides can be engineered through (nano)structuring to take



advantages of featured morphology depending on their applicable area. A dedicated article by Ren *et al.*<sup>87</sup> reviewed ordered mesoporous metal oxides and their applications. They successfully covered a variety of metal oxides with mesoporous structures from synthesis and preparation of the materials to applications in energy conversion, storage, catalysis, sensing, adsorption and separation.

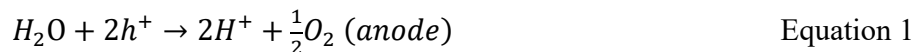
Nanostructured 1D metal oxides for photodetectors have been discussed by Zhai *et al.*<sup>88</sup> 1D nanostructures are regarded as ideal systems for investigating fundamental phenomena in nanoscale and studying aspect ratio dependence of properties of metal oxide materials for expected applications. In this comprehensive review article, photoresponse of 1D metal oxides including ZnO, SnO<sub>2</sub>, Cu<sub>2</sub>O, Ga<sub>2</sub>O<sub>3</sub>, Fe<sub>2</sub>O<sub>3</sub>, In<sub>2</sub>O<sub>3</sub>, CdO, and CeO<sub>2</sub> are introduced and the state-of-the-art of photodetector research is provided. There are other strategies to modify metal oxide materials for targeted applications, for instance, engineering of band structure, defects and crystallinity.<sup>89-91</sup>

## 1.4 Photoelectrochemical (PEC) water splitting

### 1.4.1 Mechanism and background

There is no doubt on critical necessity for development of environmentally friendly and sustainable energy even without mentioning numerical statistics on global energy crisis due to increased demand for energy.<sup>92</sup> Therefore, producing alternative energies that can compete with fossil fuels has been of a great counterdemand. As hydrogen is suggested as a promising alternative energy source, PEC water splitting (also referred to photocatalytic water splitting) to dissociate water into hydrogen and oxygen by facilitating solar energy seems to be attractive. Figure 2 shows a graphical demonstration of a typical three-electrode PEC cell.

Fundamental background of PEC water splitting will be introduced by describing a typical PEC system consisting of anode and cathode. These electrodes are immersed in aqueous solution (weak acidic or alkaline solutions). For a practical use, pure water is not applicable due to very low ionic conductivity ( $>0.05 \mu\text{S}\cdot\text{cm}^{-1}$ )<sup>91</sup> that protons are not mobile enough to participate in redox reactions. (refer to Equation 1-3).



A target material that can be either an anode or and cathode or both should exhibit

semiconducting property to generate charge carriers (electrons and holes) upon light irradiation. As seen in the previous equations, a water splitting reaction takes place through exchange of the photo-excited charge carriers. Therefore, it is necessary to wire the electrodes externally. Moreover, minimum electrical potential of 1.23 eV is required to sustain reversible reactions since water splitting is an uphill reaction, which can be aided either by physically wiring electrodes or by combining with photovoltaics. Note, however, that one must consider energy losses arising from each electrode, aqueous electrolyte and wiring. It leads to higher operation potential of 1.6-1.9 V to obtain hydrogen from water required.<sup>93,94</sup>

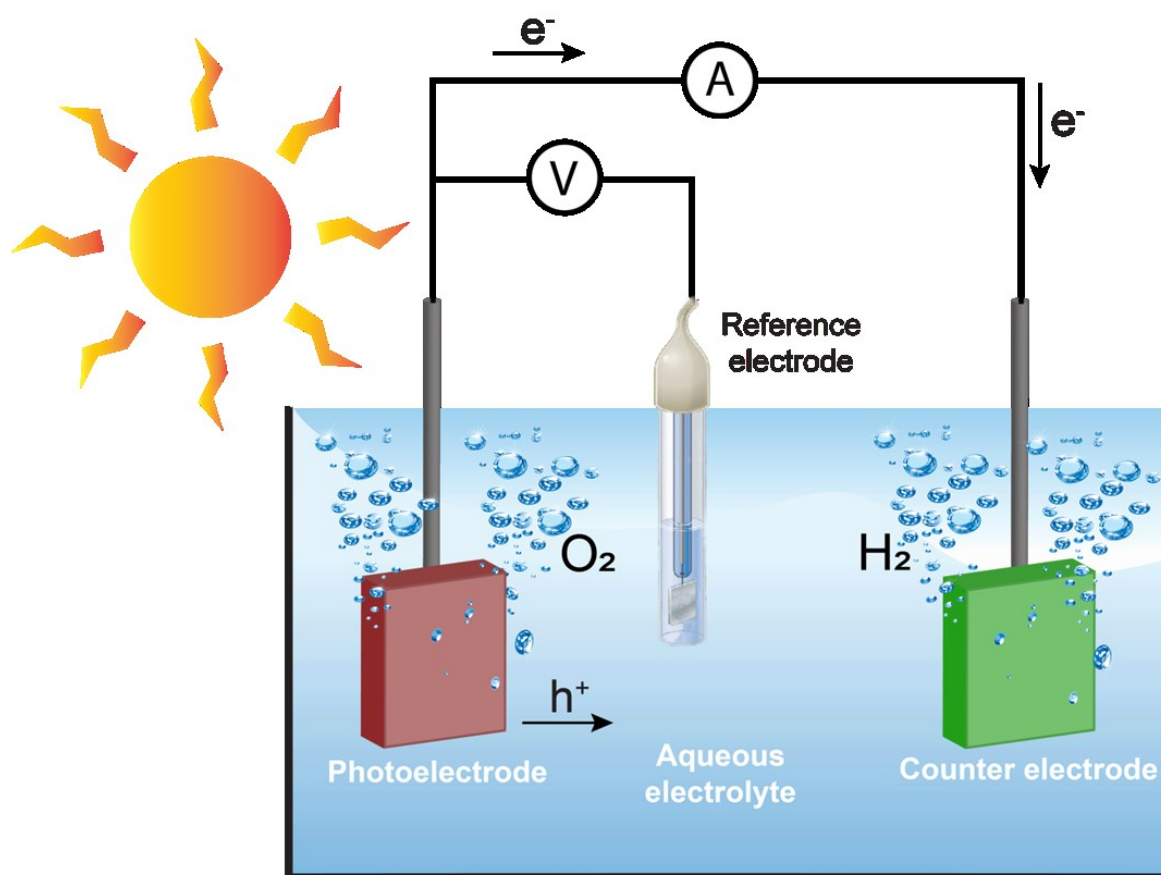


**Figure 2** A typical PEC system consisting of three electrodes showing production of hydrogen and oxygen.

There are sequential steps involved in a PEC system in which water is split into hydrogen and oxygen:<sup>91</sup> I) Formation of interface between a semiconductor and aqueous electrolyte, II) Photon absorption and charge (electron-hole pair) generation, III) Charge separation and transport, and IV) Charge extraction and formation of electrochemical product.

When a semiconductor (e.g. n-type) is in contact with aqueous electrolyte conduction and valence band of the semiconductor exhibit upward bending until it reaches thermodynamic

equilibrium with the electrolyte (see Figure 3b). Under illumination, Fermi level of the semiconductor splits into electron ( $E_{f,e}$ ) and hole quasi-Fermi level ( $E_{f,h}$ ) due to generation of excess charge carriers (Figure 3c). The difference between electron and hole quasi-Fermi level is an electrochemical potential ( $\Delta\mu$ ) and it should straddle redox potential of water (reversible potential, 1.23 eV) including overpotential losses at the cathode and the anode. Holes drive oxidation reaction at the semiconductor-electrolyte interface (Equation 1) whereas electrons transported to the counter electrode (Pt) reduce proton into hydrogen (Equation 2).

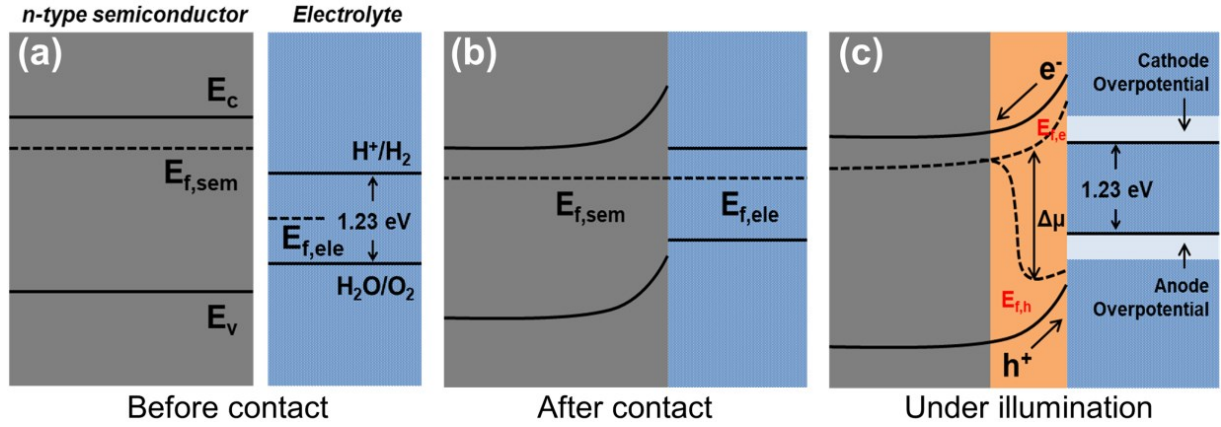


**Figure 3 Illustrations of semiconductor-electrolyte interfaces at stages of (a) before contact, (b) after contact and (c) under illumination.**

Metal oxide semiconductors are considered attractive photoelectrodes due to their outstanding (photo)electrochemical stability, favorable band edge positions and wide distribution of band gaps.<sup>95,96</sup> However, promising metal oxides for PEC water splitting derived mainly from transition metals ( $TiO_2$ ,  $WO_3$ ,  $Fe_2O_3$ ,  $NiO$ , etc.) have suffered from large band gaps and low electrical conductivity.<sup>97</sup> Thus, many efforts to tackle these challenges have been made.

PEC performance is evaluated by measuring current at applied potential under illumination, called photocurrent. As seen in Equation 2, 1 mole of hydrogen molecule ( $H_2$ ) is produced by consumption of 2 electrons, which leads to a relation between rate of hydrogen production ( $R_{H_2}$ ,  $s^{-1}$ ) and photocurrent ( $I_{ph}$ ,  $A = C/s$ ) as  $R_{H_2} = I_{ph}/2e$ .<sup>91</sup>

#### 1.4.2 State-of-the-art and literature survey

A very first demonstration on hydrogen evolution out of aqueous electrolyte was delivered by Fujishima and Honda in 1972.<sup>98</sup> They developed the idea to employ electrochemical splitting of water from the fact that an electrochemical route enables to dissociate water with potential of  $>1.23$  V (equivalent to  $\sim 1000$  nm) whereas direct decomposition of water is only possible by radiation with very short wavelength ( $<190$  nm). When  $TiO_2$  (n-type semiconductor, rutile single

crystalline) was irradiated with light, anodic current began to flow at wavelength  $<415$  nm which is equivalent to the band gap of  $\text{TiO}_2$  ( $\sim 3.0$  eV) and saturation of the current was observed at positive potential. It indicates the reaction at  $\text{TiO}_2$  is related to holes generated at the valence band of  $\text{TiO}_2$  by irradiation. Furthermore, they built an electrochemical cell consisting of a platinum electrode connected externally with the  $\text{TiO}_2$  electrode. When  $\text{TiO}_2$  was irradiated, current flowed from the platinum electrode to  $\text{TiO}_2$ , which evidences photoexcited electrons at the conduction band of  $\text{TiO}_2$  are directed to the platinum, ultimately reduce protons into hydrogen. Thus, decomposition of water is completed by redox reactions at the compartmented electrodes.

Following research works on PEC water splitting did not only develop new materials but also revealed thermodynamic limitations. Based on these efforts, successive strategies to overcome the limitations have been suggested, which includes fabrication of heterojunction for efficient charge separation, elemental doping to improve electrical conductivity, nanostructuring, and defects engineering (Table 8).

**Table 8 Metal oxides synthesized by various methods for PEC water splitting with their performances.**

Materials	Precursors	Methods	Feature and evaluation	Ref.
ZnO	ZnO target	RF sputtering	<ul style="list-style-type: none"> <li>Superior PEC response from ZnO nanorods (<math>\text{Ar}/\text{O}_2</math>) to that from ZnO films (Ar)</li> </ul>	99
$\text{TiO}_2$	$\text{Ti}(\text{OC}_3\text{H}_7)_4$	Sol-gel	<ul style="list-style-type: none"> <li>Higher photocurrent density from <math>\text{TiO}_2</math> nanowires than that from <math>\text{TiO}_2</math> thin films</li> </ul>	100
$\text{TiO}_2$	$\text{TiCl}_4$ , $\text{TiCl}_3$	Modified hydrothermal synthesis	<ul style="list-style-type: none"> <li>Photocurrent density at 1.23 V vs. RHE;</li> <li><math>0.34 \text{ mA cm}^{-2}</math> (<math>\text{TiO}_2</math> NWs), <math>0.75 \text{ mA cm}^{-2}</math> (<math>\text{TiO}_2</math> HNWs), <math>1.21 \text{ mA cm}^{-2}</math> (<math>\text{TiO}_2</math> HHNWs)</li> </ul>	101
$\text{ZnO}/\text{BiVO}_4$	$\text{Zn}(\text{NO}_3)_2/\text{Bi}(\text{NO}_3)_3 \cdot 5\text{H}_2\text{O}$ , $\text{NH}_4\text{VO}_3$	CBD/SILAR	<ul style="list-style-type: none"> <li>Photocurrent density at 1.2 V vs. Ag/AgCl;</li> <li><math>0.42 \text{ mA cm}^{-2}</math> (ZnO NRs), <math>1.72 \text{ mA cm}^{-2}</math> (ZnO NRs/<math>\text{BiVO}_4</math>)</li> </ul>	102
$\text{WO}_3/\text{BiVO}_4$	$\text{C}_{10}\text{H}_{25}\text{O}_5\text{W}/\text{Bi}(\text{NO}_3)_3$ , $\text{NH}_4\text{VO}_3$	Spin coating	<ul style="list-style-type: none"> <li>Photocurrent density at 1.23 V vs. RHE;</li> <li><math>0.35 \text{ mA cm}^{-2}</math> (<math>\text{BiVO}_4</math>), <math>0.25 \text{ mA cm}^{-2}</math> (<math>\text{WO}_3</math>), <math>1.0 \text{ mA cm}^{-2}</math> (<math>\text{WO}_3/\text{BiVO}_4</math>)</li> </ul>	103

$\text{Fe}_2\text{O}_3$	$\text{Fe}(\text{CO})_5$	RF-PECVD	<ul style="list-style-type: none"> <li>• Plasma power dependent PEC performance</li> <li>• Photocurrent density at 0.9 V vs. SCE;</li> <li>• <math>180 \mu\text{A cm}^{-2}</math> (50 W), <math>740 \mu\text{A cm}^{-2}</math> (75 W), <math>1098 \mu\text{A cm}^{-2}</math> (100 W), <math>451 \mu\text{A cm}^{-2}</math> (150 W)</li> </ul>	104
H: $\text{Fe}_2\text{O}_3$	$\text{Fe}(\text{CO})_5$	RF-PECVD	<ul style="list-style-type: none"> <li>• Reduction of <math>\text{Fe}_2\text{O}_3</math> using <math>\text{H}_2</math> plasma (hydrogenated <math>\alpha\text{-Fe}_2\text{O}_3</math>)</li> <li>• Optical absorption shift (<math>E_g = 1.51 \text{ eV}</math>)</li> <li>• Better PEC performance from hydrogenated <math>\alpha\text{-Fe}_2\text{O}_3</math></li> </ul>	105
$\text{Fe}_2\text{O}_3/\text{TiO}_2$	$\text{FeCl}_3/\text{Ti}(\text{OC}_3\text{H}_7)_4$	Hydrothermal/RF-PECVD	<ul style="list-style-type: none"> <li>• Conformal growth of <math>\text{TiO}_2</math> shell on <math>\text{Fe}_2\text{O}_3</math> nanorods</li> <li>• Linear increase in thickness of nanorod composites as a function of <math>\text{TiO}_2</math> deposition time</li> <li>• The highest photocurrent density (<math>900 \mu\text{A cm}^{-2}</math> at 0.6 V vs. SCE) from <math>\text{Fe}_2\text{O}_3/\text{TiO}_2</math> (30 min)</li> <li>• <math>\text{Fe}_2\text{O}_3</math> nanorods (<math>175 \mu\text{A cm}^{-2}</math>), <math>\text{TiO}_2</math> film (<math>50 \mu\text{A cm}^{-2}</math>)</li> </ul>	106
$\text{Fe}_2\text{O}_3/\text{TiO}_2$	$\text{Fe}(\text{CO})_5$	RF-PECVD	<ul style="list-style-type: none"> <li>• Role of graphene in a heterojunction <math>\text{Fe}_2\text{O}_3/\text{TiO}_2</math></li> <li>• Optimized position of few-layer graphene as FTO/<math>\text{Fe}_2\text{O}_3</math>/FLG/<math>\text{TiO}_2</math></li> </ul>	107

The following section briefly reviews the efforts made in our working group since those works initially motivated a large part of this report. The first report on synthesis of hematite films using PECVD opened up possibility of utilizing metal oxide films for photoelectrochemical (PEC) water splitting in Cologne.<sup>104</sup> Deposition of iron(0) pentacarbonyl ( $\text{Fe}(\text{CO})_5$ ) was carried out using capacitively coupled PECVD and crystalline hematite films were produced by post-deposition annealing at 500 °C. The hematite films were evaluated by 3-electrode system with aqueous 1 M NaOH solution under simulated solar illumination to verify their PEC activity. Depending on r.f. power induced during PECVD, photocurrent generated under the illumination varied, which became a milestone of following works on the fabrication of hematite films via PECVD and their applicability in PEC water splitting. Later, facile modification of hematite films via hydrogen plasma treatment was delivered.<sup>105</sup> It revealed that Fe:O stoichiometry was modulated, leading to variation in donor density. Moreover, the modified electronic properties of hematite films, including band gap and charge carrier density led to enhanced PEC performance. In the second phase of hematite based PEC water splitting, more sophisticated strategies based

on conceptual ideas were carried out. These efforts have been conveyed either by demonstrating multilayer of  $\text{Fe}_2\text{O}_3/\text{TiO}_2$  via PECVD/ALD, respectively, or by elemental co-doping of In and Sn simultaneously. The former study deals with systematic procedure seeking to producing efficient hematite photoanode through controls of PECVD parameters such as annealing temperature and deposition time.<sup>108</sup> Apart from this optimization part, intrinsic challenge of hematite as a photoanode was subject to being tackled by adding up a very thin  $\text{TiO}_2$  layer on hematite. Although energy band alignment of  $\text{Fe}_2\text{O}_3$  and  $\text{TiO}_2$  does not absolutely favor charge separation, energy band of hematite enclosed by  $\text{TiO}_2$  seemed to be effective for fast depletion of electrons, leading to suppression of surface recombination with holes. The latter case reported intentional co-doping of In and Sn.<sup>109</sup> Atomic diffusion of Sn from a FTO (fluorine doped tin oxide) substrate to hematite film is well known phenomenon, which influences on optical and electrical properties.<sup>110,111</sup> Synergetic effect induced by additional incorporation of In has been proven in this study. Thanks to these early hard works and dedication, further effort could be put into the topic and inevitably this research report lies on extension of the early efforts.

## 1.5 Hydrophobic coatings

### 1.5.1 Mechanism and background

Among various functionalities of materials, producing hydrophobic surface is of great interests in industry due to a wide range of applications such as water repellent fabric/umbrellas, anti-icing, self-cleaning windows, etc.<sup>112</sup> Hydrophobicity can be realized both by chemical modification and by structural engineering of surface in contact with water (lotus effect). The classical description and classification can be expressed by Young's equation as illustrated in Figure 4.<sup>113,114</sup>

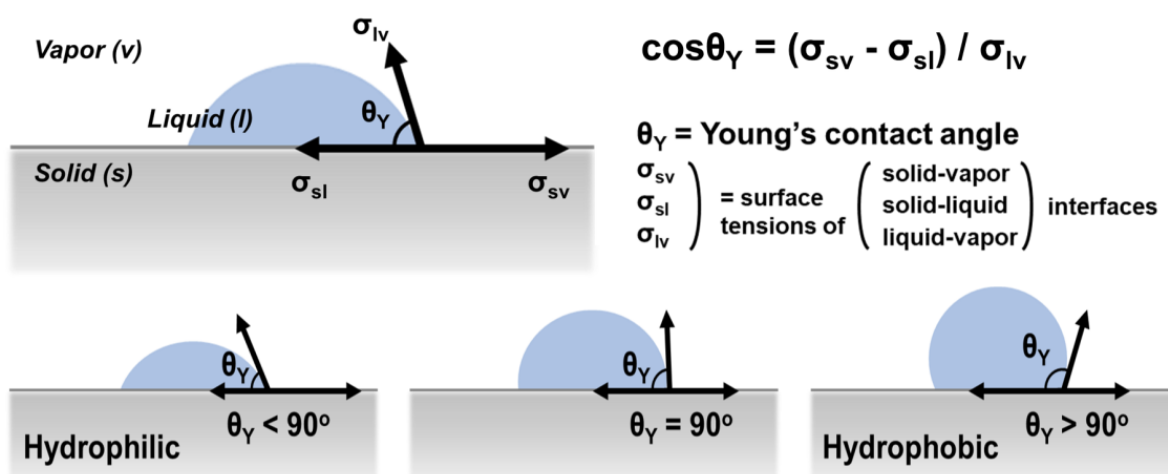


**Figure 4** A diagram with Young's equation for determination of surface hydrophobicity.

Surface hydrophobicity is determined by the water contact angle ( $\theta_Y$ ) where  $\theta_Y < 90^\circ$  for hydrophilic,  $\theta_Y > 90^\circ$  for hydrophobic and  $\theta_Y > 150^\circ$  for superhydrophobic. As can be seen in the equation in Figure 4, droplet tends to wet when the surface tension of solid-vapor interface is higher than that of solid-liquid interface whereas the droplet is repelled from the surface in the inverse case. If the surface tension of solid-vapor interface becomes so low that the contact angle exceeds  $150^\circ$ , we call the status of the surface superhydrophobic. Later, this classical description of surface hydrophobicity was further developed and modified by investigation on micro-nanostructured surface where the interfacial area between water droplet and the host surface is significantly reduced. Although both Wenzel's model<sup>115</sup> and Cassie-Baxter model<sup>116</sup> describe the contact angle of a droplet on non-smooth surface, the former deals with the droplet completely wetting on the rough surface while the latter postulates the droplet sitting on the textured surface (see Figure 5). It led to modified equations to obtain apparent contact angles with consideration of geometric factors, i.e. “ $r$ ” in Wenzel's equation as the proportion between the actual area and the projected area and “ $\phi$ ” in Cassie-Baxter model as the area portion of the solid in contact with the liquid.

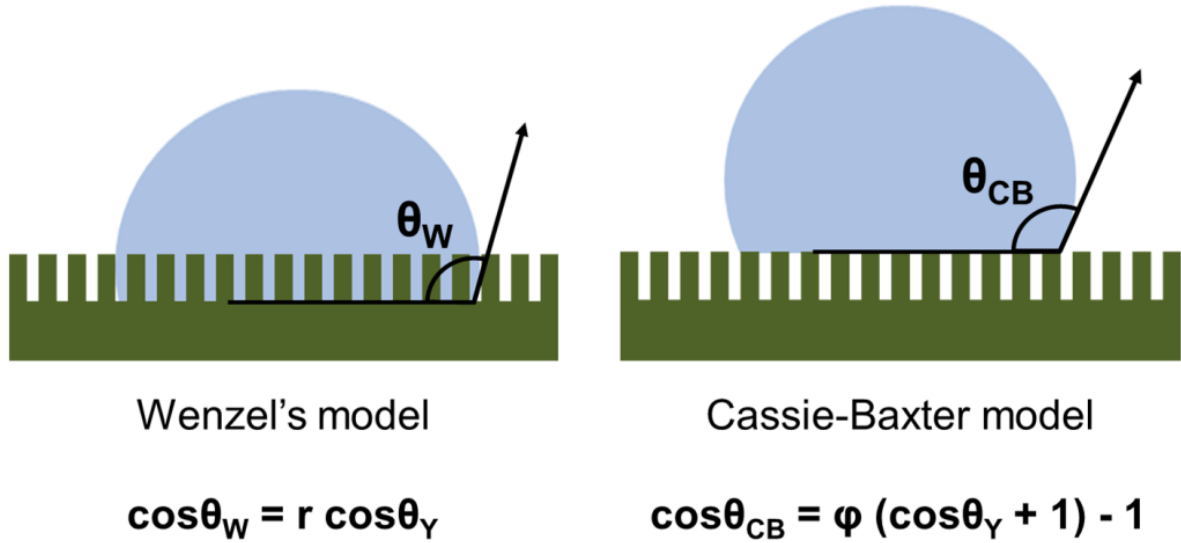


**Figure 5** Contact angle determination on a rough surface in (left) Wenzel's model and (right) Cassie-Baxter model.

### 1.5.2 State-of-the-art and literature survey

As hinted above, the combination of increasing surface roughness and lowering surface energy is the most common approach to producing superhydrophobic surfaces. Micro- or nanoscaled roughness coated with low surface energy metal oxides such as  $\text{SiO}_2$  or fluoropolymers can achieve hydrophobic surfaces. Especially, PECVD grown  $\text{SiO}_2$  or  $\text{SiO}_2$ -like films have been

widely applied to the applications. As an example, Palumbo *et al.*<sup>117</sup> firstly etched PC (polycarbonate) surfaces with O<sub>2</sub> plasma that led to nanotexturing of the polycarbonate surface. The structural geometry varied depending on the O<sub>2</sub> treatment durations and r.f. powers and the textured surface with O<sub>2</sub> plasma exhibited superhydrophobic nature, and then HMDSO was decomposed by a radio frequency-PECVD and its composites were deposited onto the textured PC. The resultant films were determined as hydrophobic SiOC and hydrophobic SiO<sub>x</sub> depending on additive gas in the plasma processes. Interestingly, hydrophilicity of the PC surface that was coated with SiO<sub>x</sub> increased for the precedently textured with O<sub>2</sub> plasma compared to the untextured surface. Moreover, when SiOC coated surface was compared with CF<sub>x</sub> coated one, slightly higher water contact angle with lower hysteresis was obtained. This work does not only stress out that the PECVD Si-based compounds are promising for achieving hydrophobic and hydrophilic surfaces but also that the structuring of the surface could additionally boost the functionalities. Another detailed demonstration on correlation between chemical and morphological states of silica was delivered by Hnilica *et al.*<sup>118</sup> They deposited SiO<sub>x</sub> ( $x \approx 2$ ) films having low carbon content using microwave plasma assisted atmospheric pressure PECVD. The structure of the SiO<sub>x</sub> film was complex 3D (3-dimensional) topography, exhibiting branched tree-like morphology. The film was superhydrophobic with contact angle exceeding 150°. To elucidate the structuring effect, contact angle was measured by using diiodomethane (CH<sub>2</sub>I<sub>2</sub>) that is non-polar liquid. It turned out that the contact angle obtained from various samples produced by varying deposition parameters exhibited from 0° to 122°, which indicates structural modulation has also strong influence on surface hydrophobicity of SiO<sub>2</sub>-like films along with their chemical nature. Pan *et al.* produced hydrophilic SnO<sub>2</sub> nanowires and hydrophobic SnO<sub>2</sub>@SnO<sub>2</sub> heterostructures. Then, SiO<sub>x</sub> film was deposited on the heterostructures using HMDSO via PECVD to produce superhydrophobic surface.<sup>119</sup>

Nguyen *et al.*<sup>120</sup> firstly increased the surface roughness with silver particles, after that SiO<sub>x</sub> layer was deposited by PECVD on the rough surface. Then, modifying the surface with 1H,1H,2H,2H-perfluorodecyltrichlorosilane to obtain superhydrophobic surface. In another study, micro-patterned GaAs (gallium arsenide) wafer was coated with SiO<sub>2</sub> via PECVD by Liu *et al.*<sup>121</sup> When obtained surface was heated, surface transited from Wenzel state to superhydrophobic Cassie state, which is desired for self-cleaning applications.



**Table 9 Metal oxides synthesized by PECVD for obtaining hydrophobic surfaces.**

Materials	Precursors	Techniques	Structure	Feature and evaluation	Ref.
SiO <sub>x</sub>	HMDSO	RF-PECVD	Nano-structured	Transparent superhydrophobic surfaces	117
SiO <sub>x</sub>	TTMS (C <sub>12</sub> H <sub>36</sub> O <sub>4</sub> Si <sub>5</sub> )	AP-PECVD	Nano-structured	Nanostructured superhydrophobic surfaces	118
SiO <sub>x</sub>	HMDSO	PECVD	Film	After PECVD coating of SiO <sub>x</sub> , switching from superhydrophilic to superhydrophobic	119
SiO <sub>x</sub>	SiH <sub>4</sub> /N <sub>2</sub> O	PECVD	Nano-structured	Apart from superhydrophobicity, the surfaces show high oleophobic properties	120
SiO <sub>2</sub>	SiH <sub>4</sub> /N <sub>2</sub> /N <sub>2</sub> O	PECVD	Film	Transited from the Wenzel state to the Cassie state	121
ZnO	ZnO NPs in n-octane	Aerosol-assisted atmospheric PECVD	Hierarchical micro/nano-structured	Advancing and receding water contact angles higher than 160°	122



## 2 Synthesis of heterojunction Fe<sub>2</sub>O<sub>3</sub>-TiO<sub>2</sub> films

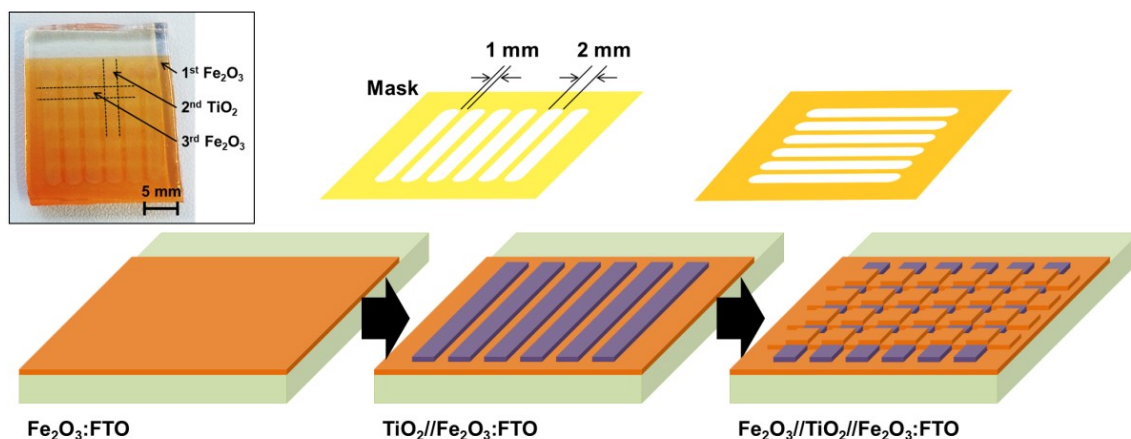
### 2.1 Motivation and background

Among a variety of means for producing efficient photoelectrodes for PEC water splitting, heterostructuring has been drawing tremendous attention and has enabled better understanding on physical phenomena taking place in the system. Dass *et al.*<sup>123</sup> described a mechanism of bi-layered photoelectrodes in PEC water splitting and reviewed various metal oxide as well as sulfide semiconductors. Theoretically speaking, it seems to be effective to fabricate heterojunction semiconductors to take advantages of reducing electron-hole recombination thanks to efficient charge separation. Thus, the key issue in heterostructuring lies on selection of semiconductors, which determines whether if their electronic structures are favorable for the photocarriers to be transported to each direction or not upon contact. Fe<sub>2</sub>O<sub>3</sub> and TiO<sub>2</sub> are of interesting candidates to construct heterojunction (n-n type semiconductor) despite unfavorable alignment of valence bands. Fe<sub>2</sub>O<sub>3</sub> (especially hematite) exhibits 1.9-2.2 eV of band gap which allows visible light absorption and TiO<sub>2</sub> is known as a good electron conducting material.<sup>124-126</sup> Moreover, PECVD processes to synthesize structured Fe<sub>2</sub>O<sub>3</sub> and TiO<sub>2</sub> are already well established.<sup>127-130</sup> Mathur *et al.*<sup>108</sup> have reported Fe<sub>2</sub>O<sub>3</sub>/TiO<sub>2</sub> heterostructure for PEC water splitting, which offered interfacial insight in the junction of the heterostructure.

Extending the concept of heterostructuring, a new strategy was tested to realize a unique structure of heterojunction photoelectrode with multiple surfaces and interfaces by macroscopic patterning. Furthermore,  $\beta$ -FeOOH nanorods were synthesized by a hydrothermal method and core-shell structured Fe<sub>2</sub>O<sub>3</sub>-TiO<sub>2</sub> heterojunction was constructed by depositing TiO<sub>2</sub> with PECVD. The latter strategy aimed for synergetic effect of 1D nanostructure and heterojunction on photoactivity for PEC water splitting.

#### 2.1.1 Design of heterojunction Fe<sub>2</sub>O<sub>3</sub>-TiO<sub>2</sub> photoelectrodes for PEC water splitting

In this section, fabrication of double and triple heterojunctions of metal oxides was realized by employing a featured mask (see Scheme 4). As a representative structure of patterned multilayered metal oxides, the initial layer of Fe<sub>2</sub>O<sub>3</sub> was fully covered on FTO substrate then, deposition of TiO<sub>2</sub> and Fe<sub>2</sub>O<sub>3</sub> with the mask was conducted (assigned as Fe<sub>2</sub>O<sub>3</sub>//TiO<sub>2</sub>//Fe<sub>2</sub>O<sub>3</sub>:FTO). The PECVD parameters of each process were adopted and modified based on the earlier studies. Confined boundaries of TiO<sub>2</sub> and Fe<sub>2</sub>O<sub>3</sub> layers were obtained, indicating successful PECVD process with the patterning mask had been achieved (see the inset of Scheme 4).



**Scheme 4** A schematic procedure of the preparation steps to fabricate a patterned  $\text{Fe}_2\text{O}_3$ - $\text{TiO}_2$  multilayer with inset presenting a photograph of the  $\text{Fe}_2\text{O}_3$ // $\text{TiO}_2$ // $\text{Fe}_2\text{O}_3$ :FTO photoelectrode.

Surface morphologies of the patterned areas are shown in Figure 6. It appears that the formation of hematite film derived from PECVD follows particulate-like growth rather than forming smooth and compact structure (Figure 6d). This porous hematite film has been often reported as a result of APCVD of  $\text{Fe}(\text{CO})_5$ .<sup>125,131,132</sup> When the second layer of  $\text{TiO}_2$  was deposited on the first  $\text{Fe}_2\text{O}_3$  layer porosity of the films seems to decrease by filling up inter-granular gaps (Figure 6c). It implies the growth of  $\text{TiO}_2$  film takes places in a distinguished manner, compared with that of  $\text{Fe}_2\text{O}_3$ . The third layer of  $\text{Fe}_2\text{O}_3$  exhibited again porous surface structure both on  $\text{Fe}_2\text{O}_3$  (Figure 6b) and on  $\text{TiO}_2$  (Figure 6a). However, the size of primary particles consisting of agglomerates on  $\text{Fe}_2\text{O}_3$  layer is smaller than that of ones observed on  $\text{TiO}_2$  (2nd) layer despite their analogous porosity. It is possibly due to difference of surface energy and morphology between  $\text{Fe}_2\text{O}_3$  and  $\text{TiO}_2$  films that affects nucleation and growth in PECVD process, which leads to dissimilar morphology of  $\text{Fe}_2\text{O}_3$  film on top. Thus, formation of a multilayer film with cross-bar structure was successfully achieved and each surface has its characteristic morphology.

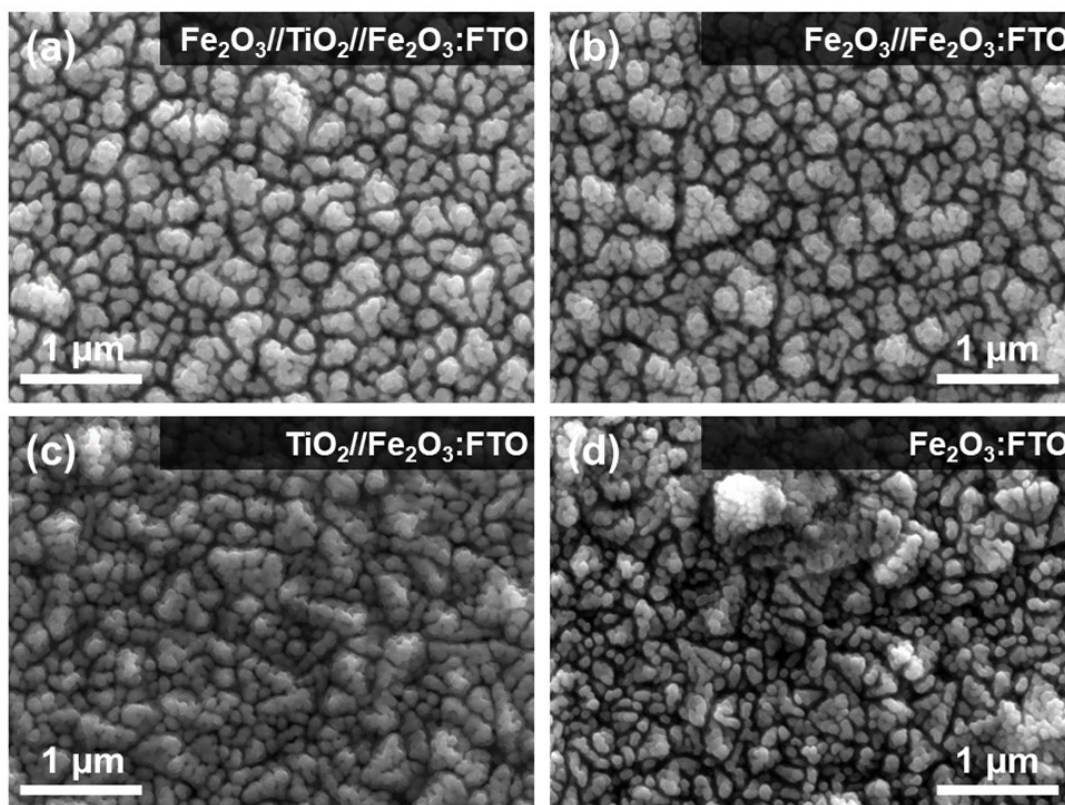


**Figure 6** Surface morphologies of the patterned triple photoanode ( $\text{Fe}_2\text{O}_3//\text{TiO}_2//\text{Fe}_2\text{O}_3:\text{FTO}$ ).

In addition to the morphological observations, elemental analysis with EDS (energy dispersive X-ray spectroscopy) has been conducted to explore compositional information on the prepared film. Figure 7 shows elemental mapping images with identical magnification as well as a corresponding SEM (scanning electron microscopy) image that represents the scanned area (Figure 7a). Firstly, a selective Fe mapping (Figure 7c) exhibits discrete contrast on each area which is distinguished by cross-lined boundary, indicating variations in atomic concentration of Fe. It corresponds well with an elemental quantification listed in Table 10, which is based on elemental spectra obtained in the rectangular areas depicted in Figure 7. The highest atomic concentration of Fe was detected from the Spectrum 2 as expected (5.29 at%). On the other hand, lower amount of Fe atoms was detected from the areas where single layer of  $\text{Fe}_2\text{O}_3$  was deposited (Spectrum 3 and 4). Secondly, when only Ti was selected, it is obvious to discriminate the patterned area with  $\text{TiO}_2$  from the masked area. However, interestingly, trace of Ti atoms can be seen in the neighboring areas ( $\text{Fe}_2\text{O}_3:\text{FTO}$  and  $\text{Fe}_2\text{O}_3//\text{Fe}_2\text{O}_3:\text{FTO}$ ).

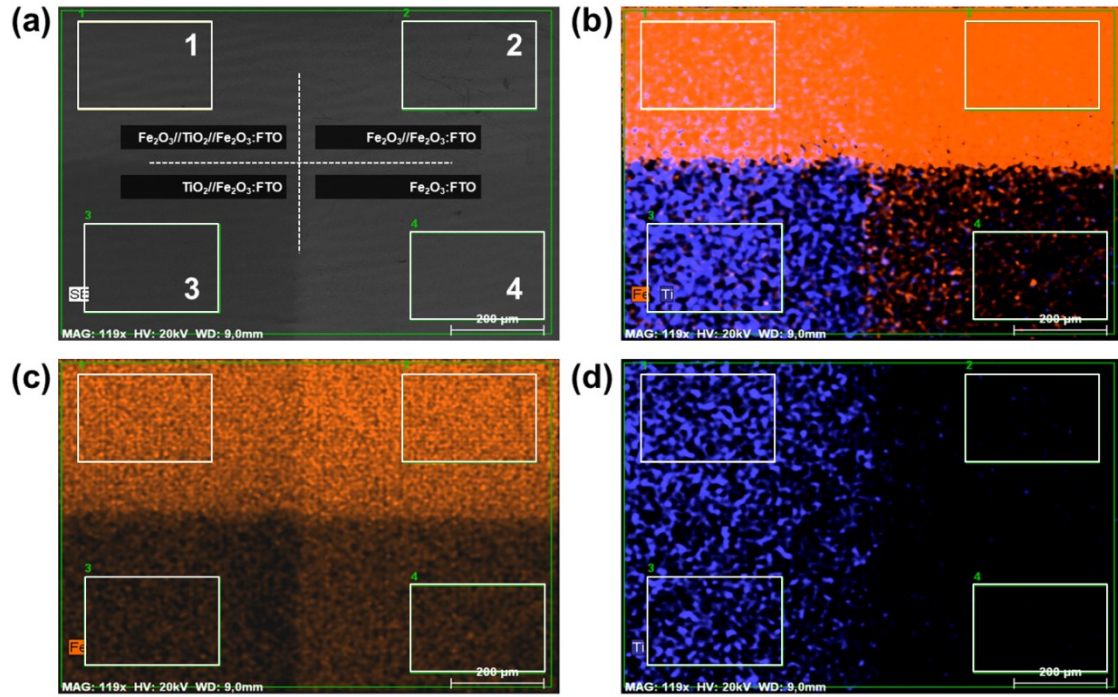
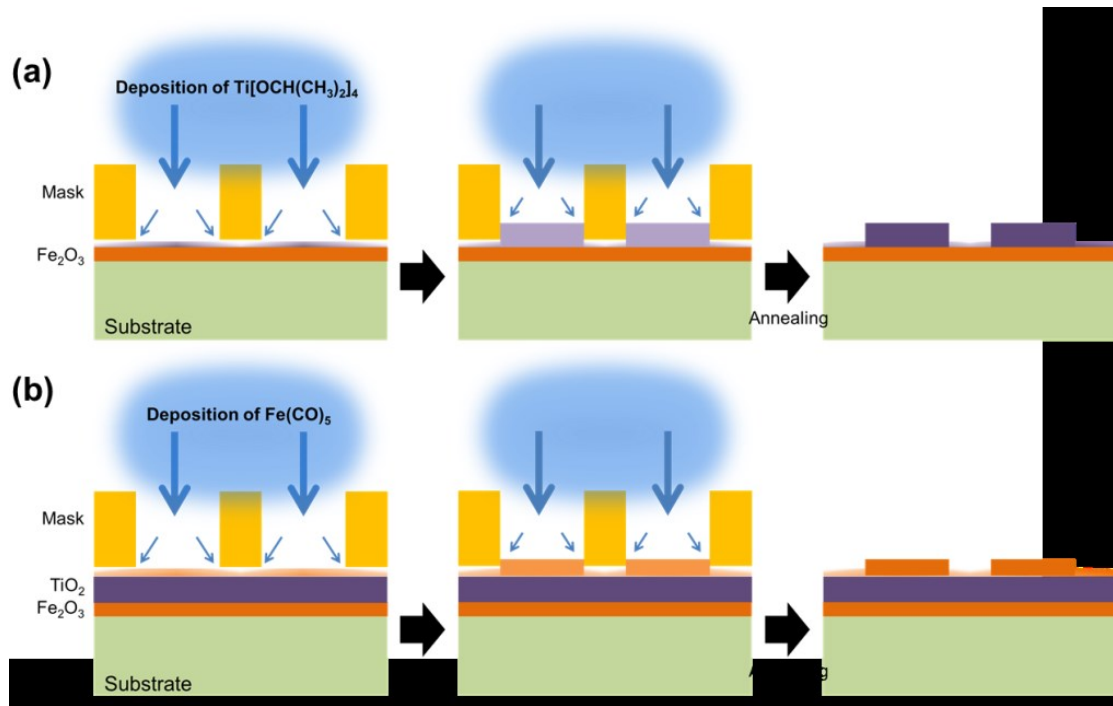


**Figure 7** Elemental distributions on the patterned structure; (a) an SEM image of the scanned area, (b) collective elemental distribution of Fe (orange) and Ti (blue), (c) and (d) selective elemental distribution of Fe and Ti, respectively. (Rectangular areas with numbers represent the scanned regions for quantitative analysis in Table 10 and scale bars represent 200  $\mu\text{m}$ .)

The existence of Ti atoms in these areas is possibly caused either by imperfect isolation during deposition or by thermally activated diffusion or migration of elements. The imperfect isolation above mentioned implies that certain reactive plasma consisting of dissociated and/or highly activated charged particles could reach under the masked area on the substrate. Moreover, thermally induced solid-state diffusion of the atoms ( $4\text{Fe}^{3+} \leftrightarrow 3\text{Ti}^{4+}$ ) cannot be completely ruled out because of repetitive high temperature (550 and 750  $^{\circ}\text{C}$  for  $\text{TiO}_2$  and  $\text{Fe}_2\text{O}_3$ , respectively) annealing steps. This hypothesis enables us to further assume that the migration of Fe atoms might have taken place during deposition and annealing processes. Thus, one can picture the structure of the patterned multilayer as partially incorporated with Ti and Fe in  $\text{Fe}_2\text{O}_3$  and  $\text{TiO}_2$ , respectively (see Scheme 5).

**Table 10** Quantitative analysis of elemental distributions on the patterned area (Rectangular areas with numbers in Figure 7) obtained by EDS.

Element	Atomic concentration (at%)			
	Spectrum 1	Spectrum 2	Spectrum 3	Spectrum 4
Oxygen	65.18	66.02	61.89	64.57
Silicon	1.94	1.98	2.63	2.75
Titanium	0.45	0.00	0.57	0.00
Tin	15.94	16.24	19.79	20.34
Aluminum	0.22	0.05	0.27	0.02
Carbon	11.59	10.42	12.62	9.47
Iron	4.70	5.29	2.24	2.85
<b>Total</b>	100	100	100	100



**Scheme 5** Illustrations of side views during the processes, describing imperfect isolation of (a) the second ( $\text{TiO}_2$ ) and (b) the third ( $\text{Fe}_2\text{O}_3$ ) layers which resulted in existence of elements on neighboring area.

However, it was limited to quantify the concentration of existing Ti in Spectrum 2 and 4 through EDS (0 at% seen in Table 10) and was necessary to confirm the earlier assumption that lateral migration of Fe to the adjacent  $\text{TiO}_2$  area might have taken place. An additional surface sensitive technique, XPS, was carried out to examine the surface of each patterned area. Figure 8 displays



survey spectra of the selective areas and enlarged regions for Fe 2p and Ti 2p. Although in-depth analyses to identify chemical states of Fe and Ti were restricted due to absence of high resolution analyses, existence of Fe and Ti on the adjacent surfaces is evident. Fe  $2p_{3/2}$  peak at  $\sim 711$  eV which is seen on  $\text{TiO}_2//\text{Fe}_2\text{O}_3:\text{FTO}$  (see blue spectrum in Figure 8b) evidences formation of iron oxide, indicating possible incorporation of Fe species either from the third deposition step ( $\text{Fe}_2\text{O}_3//\text{TiO}_2//\text{Fe}_2\text{O}_3:\text{FTO}$ ) or from vertical diffusion through annealing step. Likewise, clear evolution of Ti 2p from  $\text{Fe}_2\text{O}_3//\text{TiO}_2//\text{Fe}_2\text{O}_3:\text{FTO}$  (see red spectrum in Figure 8c) indicates formation of  $\text{TiO}_2$  by fraction of Ti species on  $\text{Fe}_2\text{O}_3$ . It is worthy to note that bump of Ti  $2p_{3/2}$  is evolved, which indicates vertical diffusion of Ti through annealing was highly likely. It is an interesting result, considering that XPS is a surface sensitive technique and  $\text{Fe}_2\text{O}_3$  on top is the last deposited layer. (see green spectrum in Figure 8c).

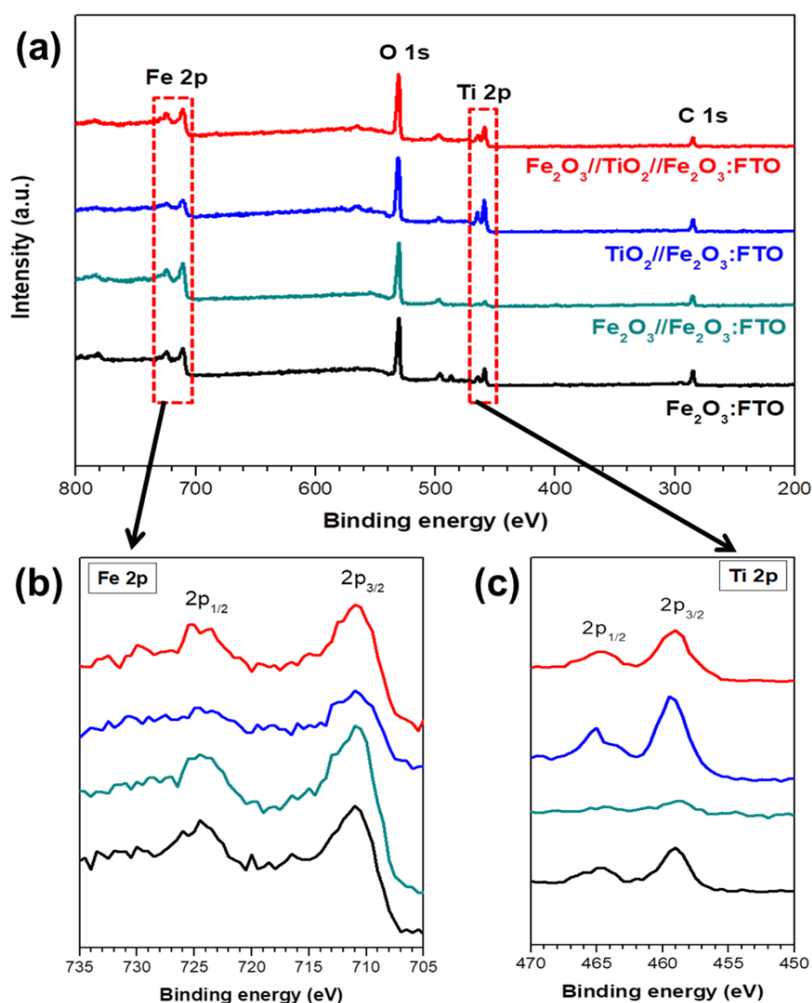


**Figure 8** (a) XPS survey spectra of the patterned areas and enlarged spectra of (b) Fe 2p and (c) Ti 2p.

PEC performances of as-prepared photoelectrodes were examined by measuring electrical



current as a function of the applied bias. Figure 9 shows J-V curves of the prepared photoelectrodes obtained using a three-electrode cell with 1.0 M NaOH as an electrolyte. Both unpatterned and patterned (Figure 9a and Figure 9b, respectively) samples exhibited anodic onset potential shift of ~100 mV upon deposition of the second TiO<sub>2</sub> layer, leading to suppressed photocurrent density. It is regarded as following results of increased recombination rate at the interface that possibly formed intermediate phase of FeTiO<sub>x</sub> and/or inappropriate valence band alignment between that of Fe<sub>2</sub>O<sub>3</sub> and of TiO<sub>2</sub> for photoholes to overcome. When the third layer of Fe<sub>2</sub>O<sub>3</sub> was deposited superior photocurrent density was obtained at high potential regime, leading to ~2.1 mA/cm<sup>2</sup> at 1.8 V vs. RHE for both patterned and unpatterned triple layers of Fe<sub>2</sub>O<sub>3</sub>//TiO<sub>2</sub>//Fe<sub>2</sub>O<sub>3</sub>:FTO. However, high photocurrent density driven by anodic bias (especially with anodic onset potential) cannot be a prominent sign as an efficient PEC performance since it is not regarded as a consequence of photoelectrochemical reaction for water redox reaction but of electrochemical reaction. Nevertheless, J-V curves obtained from the unpatterned and the patterned multilayers shows effectiveness of the macro-scaled patterning on PEC performance (see Figure 9c and Figure 9d). The patterned TiO<sub>2</sub>//Fe<sub>2</sub>O<sub>3</sub>:FTO and Fe<sub>2</sub>O<sub>3</sub>//TiO<sub>2</sub>//Fe<sub>2</sub>O<sub>3</sub>:FTO outperformed the unpatterned photoelectrodes in the whole range of the applied bias. It might be ascribed to: 1) a variety of surface morphologies formed by heterogeneous materials, 2) smaller interfacial area where recombination of photogenerated charge carriers takes place in the patterned photoelectrodes compared with the fully covered multilayers, 3) improved electrical conductivity thanks to “counter doping effect”, i.e. incorporation of Fe and Ti to neighboring TiO<sub>2</sub> and Fe<sub>2</sub>O<sub>3</sub> areas, respectively,<sup>133–135</sup> 4) new pathways for charged carriers along the patterned surface, and 5) better charge separation at the interface of Fe<sub>2</sub>O<sub>3</sub> and TiO<sub>2</sub> although the energetics that includes energy band bending at various structures needs to be elucidated more carefully.

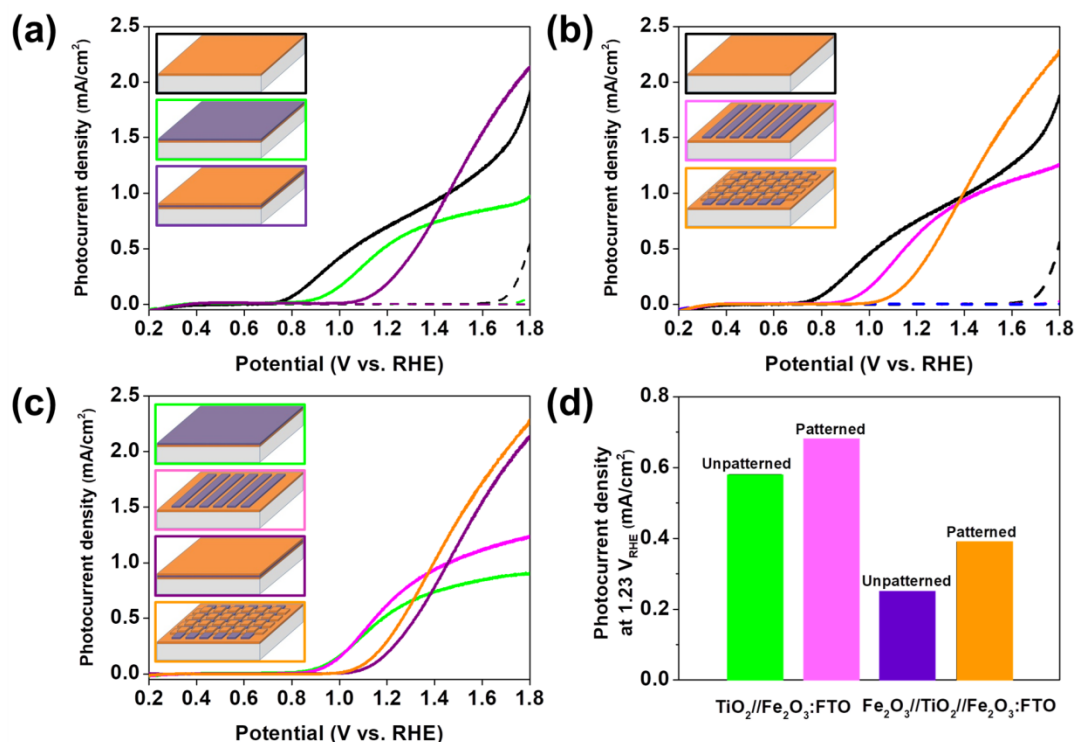


**Figure 9** J-V curves of the prepared photoelectrodes under darkness (dashed lines) and under illumination (solid lines): (a)  $\text{Fe}_2\text{O}_3:\text{FTO}$ -black, unpatterned  $\text{TiO}_2//\text{Fe}_2\text{O}_3:\text{FTO}$ -green and  $\text{Fe}_2\text{O}_3//\text{TiO}_2//\text{Fe}_2\text{O}_3:\text{FTO}$ -purple, (b)  $\text{Fe}_2\text{O}_3:\text{FTO}$ -black, patterned  $\text{TiO}_2//\text{Fe}_2\text{O}_3:\text{FTO}$ -magenta and  $\text{Fe}_2\text{O}_3//\text{TiO}_2//\text{Fe}_2\text{O}_3:\text{FTO}$ -orange, (c) comparison of J-V curves between unpatterned and patterned multilayers, and (d) photocurrent density values at water redox potential of  $1.23 \text{ V vs. RHE}$ .

For further understandings of charge carriers' transfer through interfaces, thickness of the  $\text{TiO}_2$  layer was varied by controlling duration of PECVD process. Fully covered  $\text{Fe}_2\text{O}_3//\text{TiO}_2//\text{Fe}_2\text{O}_3:\text{FTO}$  multilayer was chosen as a modeled structure for simplification, which allows to eliminate the effect of patterning observed above and to only consider electronic structure. J-V curves of the photoelectrodes with various thickness of  $\text{TiO}_2$  are presented in Figure 10. Similar anodic onset potential shift was clearly observed regardless of the thickness of  $\text{TiO}_2$  layer, along with decreased photocurrent density. The extent of reduction in photocurrent became severe as the deposition time of  $\text{TiO}_2$  increased, i.e. the thicker the  $\text{TiO}_2$  layer, the lower photocurrent was generated (compare Figure 10a-c). However, it appears that slight photocurrent density of several tens of  $\mu\text{A}/\text{cm}^2$  was generated at quite low potential of  $\sim 0.4 \text{ V vs. RHE}$  from  $\text{TiO}_2//\text{Fe}_2\text{O}_3:\text{FTO}$  ( $\text{TiO}_2$  for 30 and 60 min), which is assigned to typical J-V feature of  $\text{TiO}_2$  photoanodes (see Figure 10e and Figure 10f).<sup>136–138</sup> Focusing on  $\text{Fe}_2\text{O}_3//\text{TiO}_2//\text{Fe}_2\text{O}_3:\text{FTO}$  photoelectrodes, gradual decrease in photocurrent density as thickness of intercalated  $\text{TiO}_2$  increases is also observed.

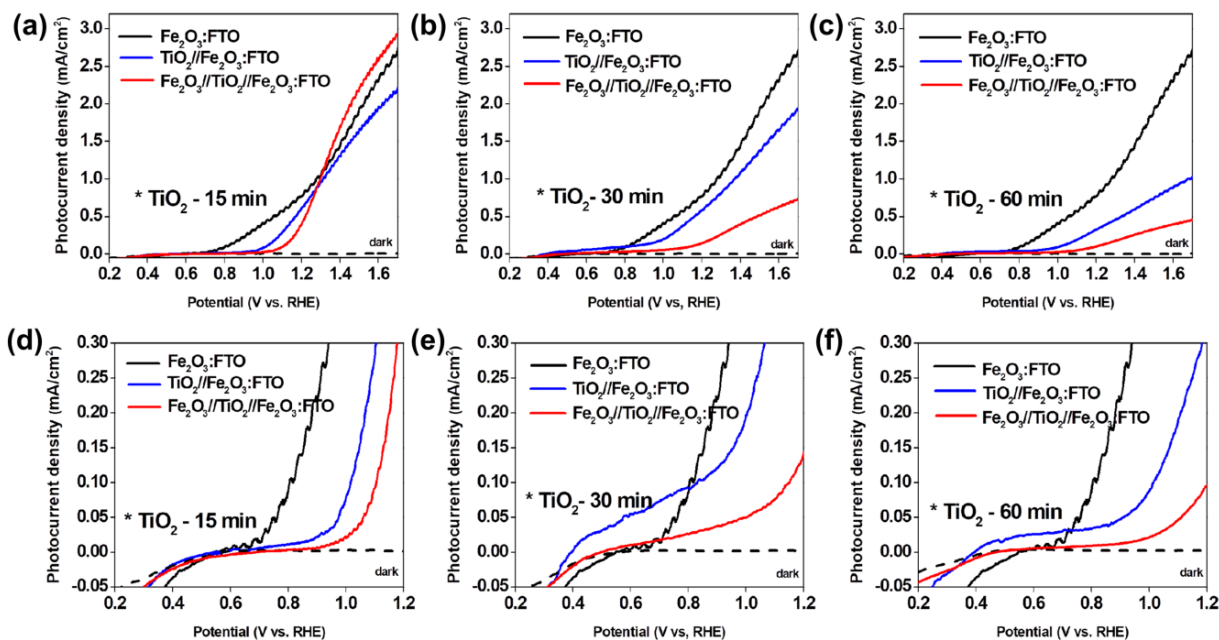
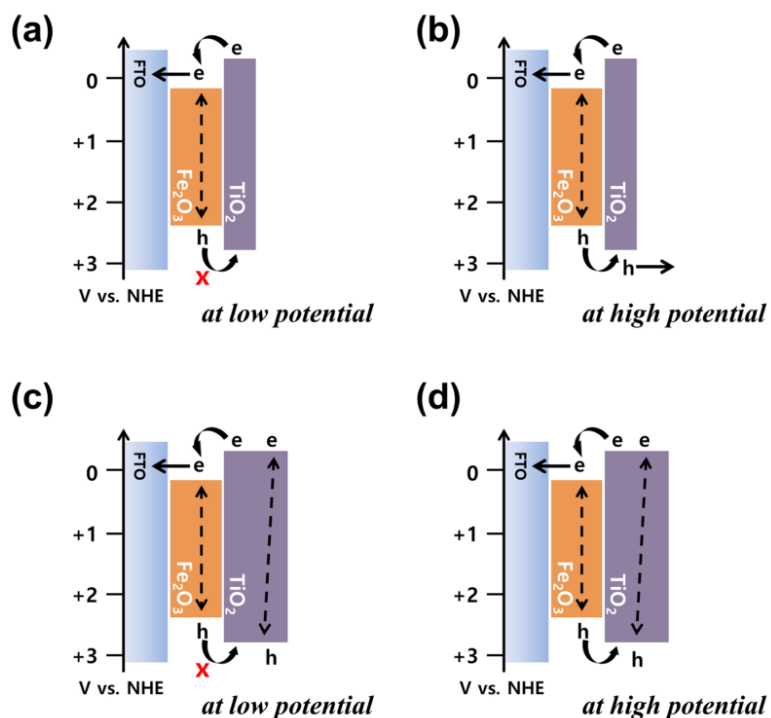
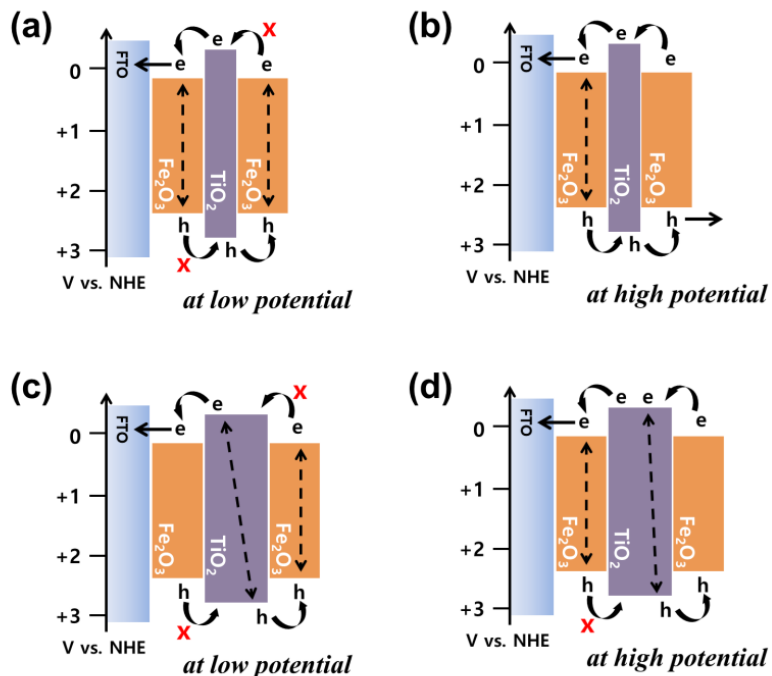


**Figure 10** Dependence of  $\text{TiO}_2$  thickness on J-V behavior of double/triple photoelectrodes: (a, d) 15 min, (b, e) 30 min and (c, f) 60 min of deposition times for  $\text{TiO}_2$  layer.

As widely known valence band of  $\text{TiO}_2$  lies at higher potential than that of  $\text{Fe}_2\text{O}_3$ , which is unfavorable for holes generated at the valence band of  $\text{Fe}_2\text{O}_3$  to be drifted to that of the  $\text{TiO}_2$  over-layer, inhibiting efficient oxygen evolution at the semiconductor-electrolyte interface.<sup>108</sup> This misalignment of energy bands and interface with possible intermediate oxide phases could increase recombination rate due to hindrance of efficient charge transport. Observing J-V curves shown in Figure 9a, rapid increase in photocurrent density is observed from  $\text{TiO}_2//\text{Fe}_2\text{O}_3:\text{FTO}$  when high overpotential ( $>1.2$  V vs. RHE) was applied. This might result from higher extent of band bending that allows holes at the valence band of  $\text{Fe}_2\text{O}_3$  to overcome energy barrier.<sup>106</sup> However, as the thickness of  $\text{TiO}_2$  increases this overpotential effect seems to be diminished, leading to retarded photoresponse even at high overpotential not only in  $\text{TiO}_2//\text{Fe}_2\text{O}_3:\text{FTO}$  but also in  $\text{Fe}_2\text{O}_3//\text{TiO}_2//\text{Fe}_2\text{O}_3:\text{FTO}$  (compare Figure 9b and Figure 9c). While these holes from  $\text{Fe}_2\text{O}_3$  participate in oxidation reaction at the interface of  $\text{TiO}_2$ /electrolyte when the  $\text{TiO}_2$  is thin, they could be recombined with electrons in bulk before reaching the interface when the  $\text{TiO}_2$  is thick. Based on the observation above, charge transfer scenarios through interfaces are proposed and depicted in Scheme 6 and Scheme 7.



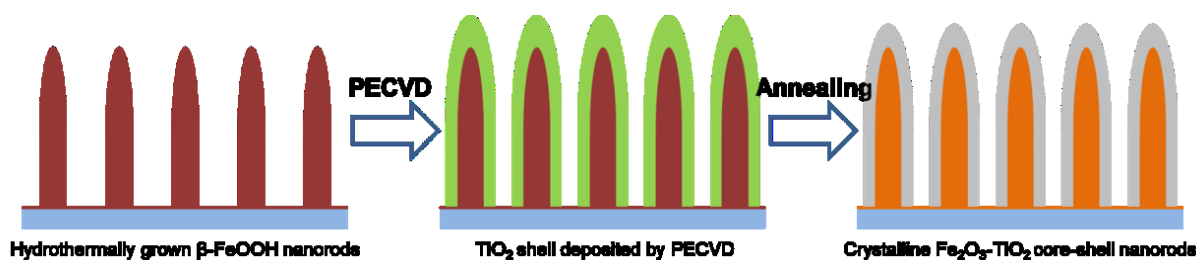
**Scheme 6** Proposed charge transfer schemes through interface in bi-layer structures of  $\text{TiO}_2//\text{Fe}_2\text{O}_3:\text{FTO}$  depending on thickness of  $\text{TiO}_2$  layer and overpotential.



**Scheme 7** Proposed charge transfer schemes through interface in triple-layer structures of  $\text{Fe}_2\text{O}_3//\text{TiO}_2//\text{Fe}_2\text{O}_3:\text{FTO}$  depending on thickness of  $\text{TiO}_2$  layer and overpotential value.

### 2.1.2 Core-shell structured heterojunction of $\text{Fe}_2\text{O}_3$ - $\text{TiO}_2$ photoelectrodes

1D hematite nanorods have been adopted to fabricate  $\text{Fe}_2\text{O}_3$ - $\text{TiO}_2$  photoelectrodes. Since it is inevitable for photoelectrodes to have contact with aqueous electrolyte in PEC water splitting, nanostructuring to realize large surface area is regarded as one of promising approaches.<sup>139–141</sup> In addition to dimensional advantage, it is expected to achieve synergetic effect on photoactivity by heterostructuring. In this study, typical hydrothermal synthesis route was employed to grow iron oxyhydroxide ( $\beta$ - $\text{FeOOH}$ ) nanorods followed by PECVD of  $\text{Ti}[\text{OCH}(\text{CH}_3)_2]_4$  for constructing heterojunction core-shell ( $\text{Fe}_2\text{O}_3$ - $\text{TiO}_2$ ) photoelectrodes (Scheme 8). Thus, this work is distinguished from the earlier study that dealt with planar heterojunction.



**Scheme 8** A schematic process to prepare 1D heterostructure of  $\text{Fe}_2\text{O}_3$ - $\text{TiO}_2$  photoelectrode.

SEM images of the prepared photoelectrodes on FTO substrates are presented in Figure 11. Pristine hematite nanorods (Figure 11a) were obtained by annealing  $\beta$ - $\text{FeOOH}$  nanorods at  $750^\circ\text{C}$ , which is not only to induce Sn doping to improve photoactivity<sup>110</sup> but to sustain the post-annealing environment. They exhibit smooth surface (see inset of Figure 11a) and are randomly oriented as observed in other studies.<sup>142,143</sup>  $\text{Fe}_2\text{O}_3$ - $\text{TiO}_2$  composites were fabricated by deposition of  $\text{TiO}_2$  with varied PECVD processes. The composite resulted from 10 min PECVD process for  $\text{TiO}_2$  exhibits  $\sim 100$  nm in diameter (see Figure 11b) with good step coverage of  $\text{TiO}_2$  particles on  $\text{Fe}_2\text{O}_3$  nanorods as if formation of  $\text{TiO}_2$  shell took place homogeneously. When the deposition time was prolonged to 30 min the diameter of nanorods increased to  $\sim 200$  nm and particulate morphology of  $\text{TiO}_2$  became more noticeable. Considering randomness orientation of hematite nanorods and their thickness ( $\sim 50$  nm), it is apparent that the  $\text{TiO}_2$  shell further grew in the vertical direction to the substrate, which implies that the  $\text{Fe}_2\text{O}_3$  nanorods did not act as template for the  $\text{TiO}_2$  shells anymore. Rather anisotropic growth of  $\text{TiO}_2$  might take place like the case of PECVD of  $\text{Fe}(\text{CO})_5$ , leading to columnar structure of the agglomerates and gaps in between. When the deposition time became prolonged to 60 min, drastic decrease in distance between the  $\text{TiO}_2$  columns by merging and further growth of the particles was observed. A modified growth model of  $\text{Fe}_2\text{O}_3$ - $\text{TiO}_2$  core-shell structure is suggested in Scheme 9.

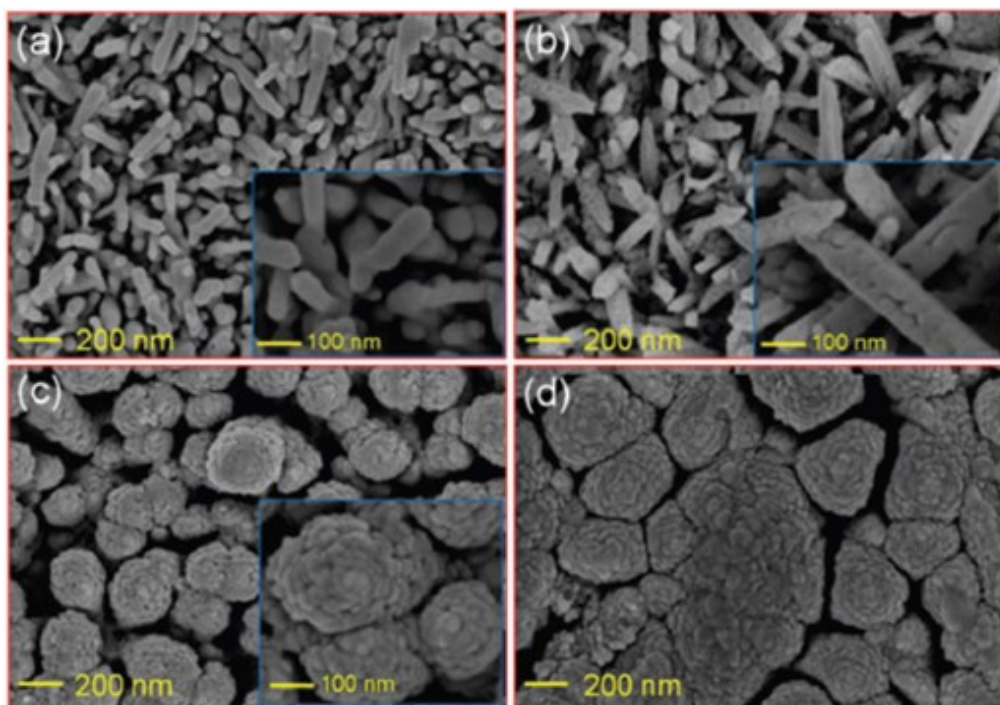
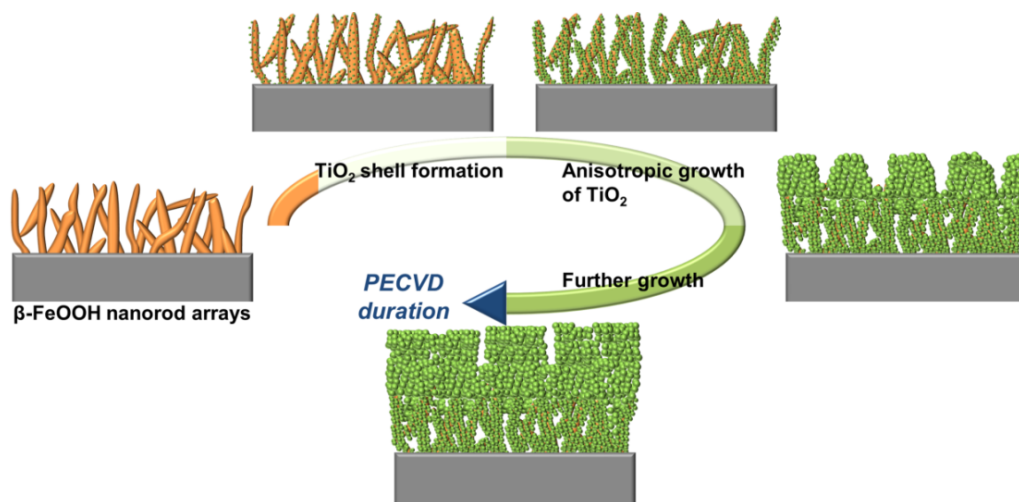


Figure 11 SEM images of (a)  $\text{Fe}_2\text{O}_3$ -(0 min) $\text{TiO}_2$ , (b)  $\text{Fe}_2\text{O}_3$ -(10 min) $\text{TiO}_2$ , (c)  $\text{Fe}_2\text{O}_3$ -(30 min) $\text{TiO}_2$ , and (d)  $\text{Fe}_2\text{O}_3$ -(60 min) $\text{TiO}_2$  composites (Reproduced from Ref. <sup>106</sup> with permission from The Royal Society of Chemistry).



Scheme 9 A simplified model depicting formation of  $\text{Fe}_2\text{O}_3$ - $\text{TiO}_2$  core-shell composites.

Photoresponses of the prepared  $\text{Fe}_2\text{O}_3$ - $\text{TiO}_2$  composites have been recorded and are presented in Figure 12. The core-shell composites were prepared by varying deposition time for  $\text{TiO}_2$  in PECVD and  $\beta$ - $\text{FeOOH}$  nanorod arrays synthesized under the same hydrothermal condition were used as a hosting material. Pristine  $\text{Fe}_2\text{O}_3$  nanorods arrays obtained from the hydrothermal route and the  $\text{TiO}_2$  film from PECVD were also tested in the linear scan voltammetry to verify



effectiveness of constructing 1D heterojunction.

Steady increase in photocurrent density was observed from the hematite nanorods photoanode, exhibiting  $\sim 0.8$  V of onset potential. The maximum photocurrent density was obtained at 1.8 V vs. RHE as  $\sim 0.2$   $\text{mA}/\text{cm}^2$ . The PEC performance of pure PECVD  $\text{TiO}_2$  was poorer than that of the pristine  $\text{Fe}_2\text{O}_3$  nanorods, which is a typical feature of  $\text{TiO}_2$  due to limited light absorbance. In contrast, core-shell structured  $\text{Fe}_2\text{O}_3$ - $\text{TiO}_2$  photoanodes displayed remarkable enhancement in photocurrent density at anodic bias, which indicates that combination of  $\text{Fe}_2\text{O}_3$  and  $\text{TiO}_2$  improved PEC performance. Note that the composites consisting of 5 min and 10 min  $\text{TiO}_2$  shell showed poorer J-V behavior than the pristine  $\text{Fe}_2\text{O}_3$  nanorods. It might be due to incomplete formation of core-shell structure that negatively affected photoactivity of the composite photoanodes. Hematite nanorods insufficiently covered with  $\text{TiO}_2$  particles seemed to be undesirable for PEC water splitting possibly due to: 1) high defect density on the surface of nanorods generated by plasma and 2) recombination at the  $\text{Fe}_2\text{O}_3/\text{TiO}_2$  interface that might overpowered charge separation effect. On the other hand, the best performing  $\text{Fe}_2\text{O}_3$ - $\text{TiO}_2$  core-shell photoanodes where deposition time of 20 and 30 min for  $\text{TiO}_2$  reached  $\sim 0.19$   $\text{mA}/\text{cm}^2$  at the water redox potential of 1.23 V vs. RHE and exhibited steady increase.

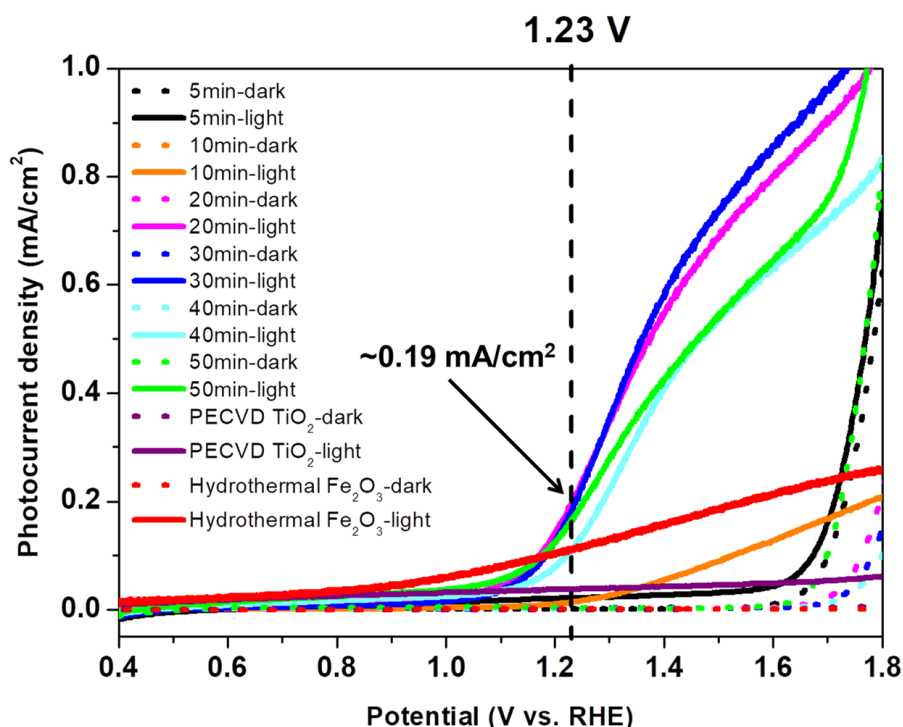


**Figure 12** J-V characteristics of the core-shell  $\text{Fe}_2\text{O}_3$ - $\text{TiO}_2$  composites depending on deposition time of  $\text{Ti}[\text{OCH}(\text{CH}_3)_2]_4$ . Pure  $\text{TiO}_2$  and  $\text{Fe}_2\text{O}_3$  produced by PECVD (30 min) and hydrothermal synthesis, respectively, were also tested as comparisons.

## 2.2 Conclusions

In the patterning of  $\text{Fe}_2\text{O}_3/\text{TiO}_2$  multilayers, successive confinement of each layer was achieved by employing the featured mask during PECVD. Surfaces of the architected area exhibited distinguishable morphologies due to template effect of the base surface. Elemental analyses conducted by EDS and XPS revealed possibility of atomic diffusion both in orthogonal and in lateral directions, which were ascribed either to imperfect isolation during deposition or to annealing step. This structural characteristics turned out to affect PEC performance of the patterned photoanode ( $\text{Fe}_2\text{O}_3//\text{TiO}_2//\text{Fe}_2\text{O}_3:\text{FTO}$ ). In general, detrimental PEC performance was observed as the number of layers increased regardless of the patterning, which is regarded as a result of increased recombination sites at the junctions of  $\text{Fe}_2\text{O}_3$  and  $\text{TiO}_2$ . However, it is noteworthy that the patterned bi- and triple layers exhibited better PEC performances than the unpatterned ones. The extra study revealed that the thickness of intercalated  $\text{TiO}_2$  played an important role in charge carrier transport through junctions.

In the combinatorial structure of  $\text{Fe}_2\text{O}_3$ - $\text{TiO}_2$  core-shell photoanodes, quite conformal deposition of  $\text{TiO}_2$  using PECVD was observed on  $\text{Fe}_2\text{O}_3$  nanorods. Thicker  $\text{TiO}_2$  shell was obtained from the longest PECVD of  $\text{TiO}_2$ , leading to decreased surface area of the composites. PEC performances of the prepared composites varied with respect to the thickness of  $\text{TiO}_2$  shell and their current densities showed typical type-I heterojunction behavior.<sup>144,145</sup> Overall efficiency of the composites (30 and 60 min  $\text{TiO}_2$  on hematite nanorods) outperformed both pristine hematite nanorods and PECVD  $\text{TiO}_2$  film. The improved PEC performance obtained from the core-shell composites was attributed not only to the efficient charge separation but to increased surface area thanks to granular structure of  $\text{TiO}_2$  shell.



### 3 Surface modification of hematite films by post-treatments

#### 3.1 Motivation and background

In this Chapter, effects of post-synthesis treatments consisting of plasma and short annealing steps on hematite films were studied. Due to sluggish transportation of photoholes to hematite surface, reducing recombination rate and enhancing hole mobility are of great interests to promote OER (oxygen evolution reaction).<sup>146</sup> Especially, surface modification to tackle the former issue is known as a good approach to suppress surface recombination.<sup>147,148</sup> Utilizing plasma as a source of modification agent has been motivated since it is widely accepted as an effective mean of surface modification.<sup>149</sup> In addition to the plasma, sequential annealing step was conducted to relax the plasma-treated surface. Roles of these post-synthesis treatments were evaluated by systematic experimental procedures and described in the following section.

##### 3.1.1 Post-synthesis treatment of hematite via oxygen plasma

Firstly, the as-obtained samples were examined by SEM to comparatively identify the effect of plasma on morphology of hematite (Figure 13). The pristine hematite film consisting of agglomerates of particles tends to grow bigger as the duration of plasma treatment increases, which led to significant reduction of spaces between agglomerates. However, no significant changes in morphology was observed after the plasma treated samples were annealed shortly, indicating that the short annealing step did not contribute to bulk diffusion or film densification. Bombardment of oxygen species in the plasma process plays a main role to promote grain growth of hematite particles. It is consistent with a previous result reported by Mathur *et al.* that 2D (2-dimensional) SnO<sub>2</sub> platelets collapsed into elongated granular structure and nanoglobular particles at 25 W and 125 W of plasma power, respectively.<sup>150</sup>

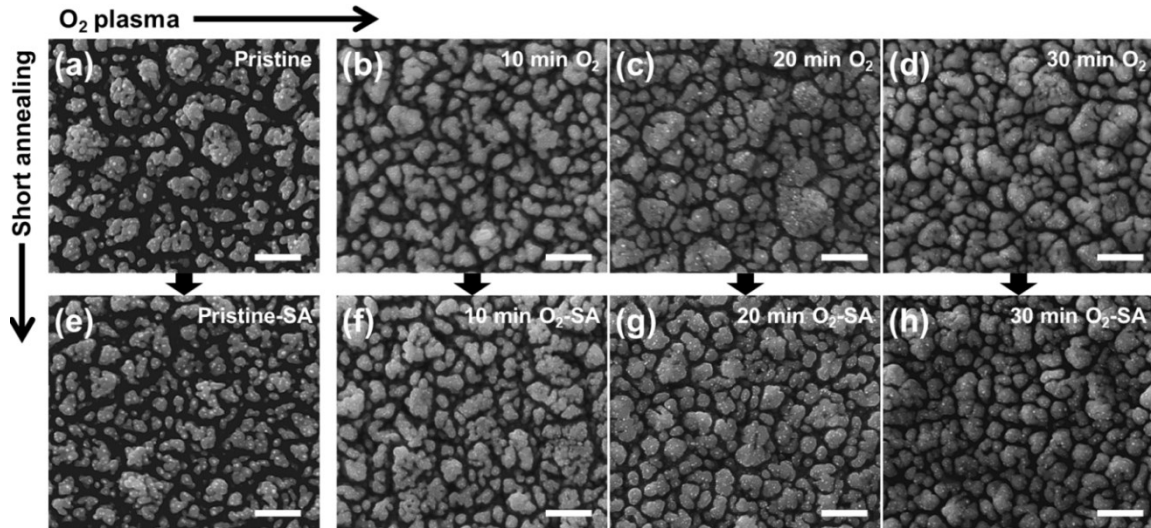


**Figure 13** Upper row: Optical micrographs of (a) pristine hematite and post-treated hematite by oxygen plasma for (b) 10 min, (c) 20 min, and (d) 30 min; Lower row: hematite films post-treated by short annealing (750 °C for 10 min) after oxygen plasma processes for corresponding duration. Scale bars are 500 nm.

Figure 14 displays surface topographies and corresponding diagonal line profiles of the hematite samples that were treated with oxygen plasma for given duration followed by short annealing. Based on diagonal line profiles, the hematite film treated with oxygen plasma for 10 min followed by short annealing exhibited the roughest surface, showing 101.768 nm, 20.708 nm and 16.390 nm of peak-valley roughness ( $R_{pv}$ ), root-mean-square roughness ( $R_q$ ), and average roughness ( $R_a$ ), respectively (see Figure 15). It was found that the roughness value gradually decreases as the oxygen plasma time increases, which indicates plasma with reactive oxygen species can flatten the surface by energetic ion bombardment although the pristine hematite exhibits the lowest roughness.

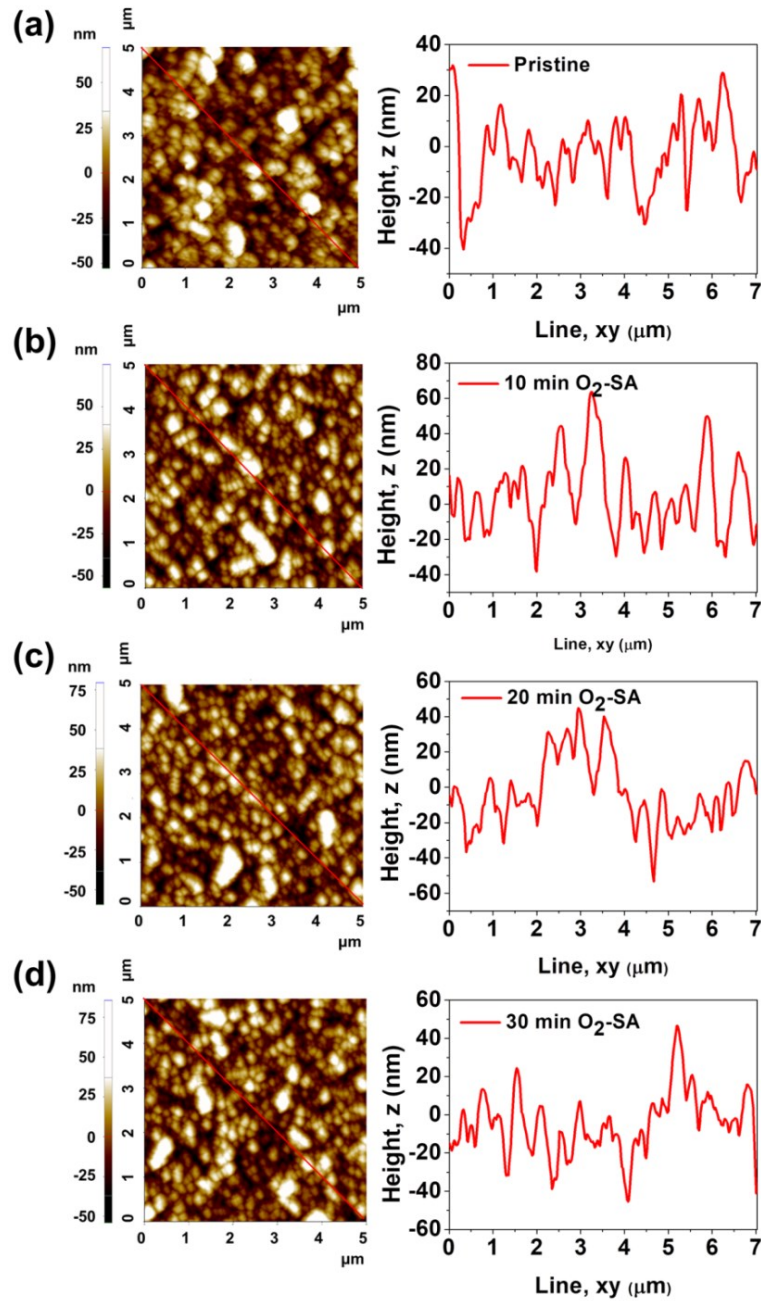


**Figure 14** Surface topography images obtained by AFM and corresponding diagonal line profiles of (a) pristine hematite and oxygen plasma treated for (b) 10 min, (c) 20 min and (d) 30 min followed by short annealing.

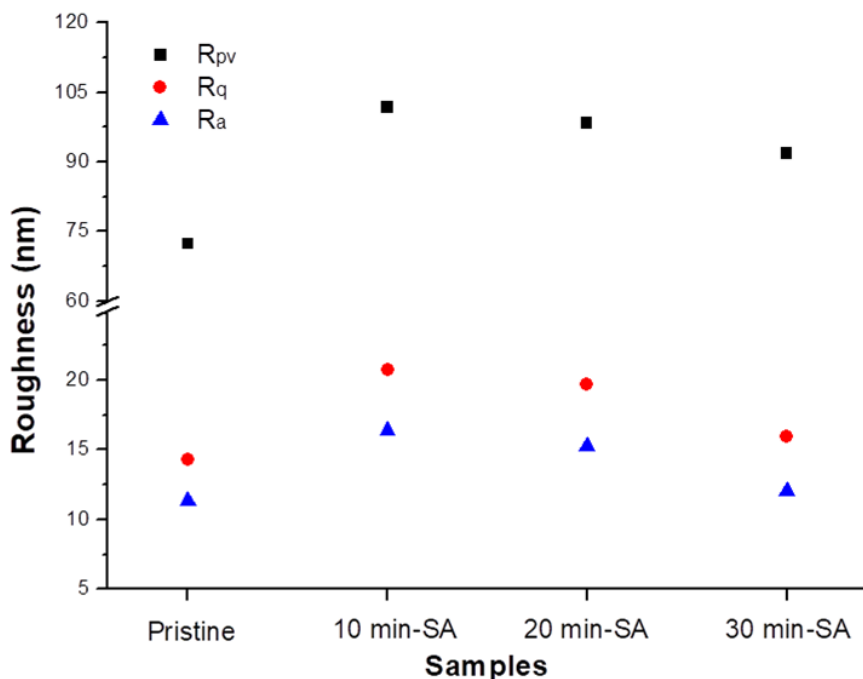


**Figure 15** Roughness of the prepared hematite films obtained from the diagonal line profiles given in Figure 9.  $R_{pv}$ ,  $R_q$  and  $R_a$  refer to peak-valley, root mean square and average roughness values, respectively.

In addition to observation of the films, photoresponses of the prepared samples have been recorded by measuring electrical current in a 3-electrode system and are shown in Figure 16. When the hematite films were treated with oxygen plasma (see Figure 16a), severe shift in onset potential ( $V_{onset}$ ) was observed.  $V_{onset}$  values were determined by reading the voltage values where the current density reaches  $0.02 \text{ mA/cm}^2$ . The highest  $V_{onset}$  was obtained from the sample treated with oxygen plasma for 10 min (1.10 V vs. RHE) whereas the untreated hematite photoelectrode exhibited 0.74 V vs. RHE. Consequently, photocurrent density of oxygen plasma treated hematite film for 10 min was  $0.035 \text{ mA/cm}^2$  at water redox potential (1.23 V vs. RHE). Interestingly, when the films were further annealed at  $750^\circ\text{C}$  for 10 min after the oxygen plasma  $V_{onset}$  of the post-treated samples became almost equal to that of the pristine sample and noticeable enhancement in photocurrent density was achieved. Among the modified samples, the hematite photoelectrode treated with oxygen plasma for 20 min followed by the short annealing process performed best showing  $1.306 \text{ mA/cm}^2$  at 1.23 V vs. RHE with 0.76 V of  $V_{onset}$ . To clarify the origin of photoelectrochemical behavior, a hematite film that was annealed shortly without preceding oxygen plasma was also prepared. As can be seen in Figure 16c, the photocurrent density of hematite only annealed briefly was lower in the whole range of the applied potential than that of pristine hematite, yet maintaining onset potential. It implies that the additional heat treatment alone did not enhance photoactivity of hematite. Figure 16d provides

summary of the PEC behaviors described above.

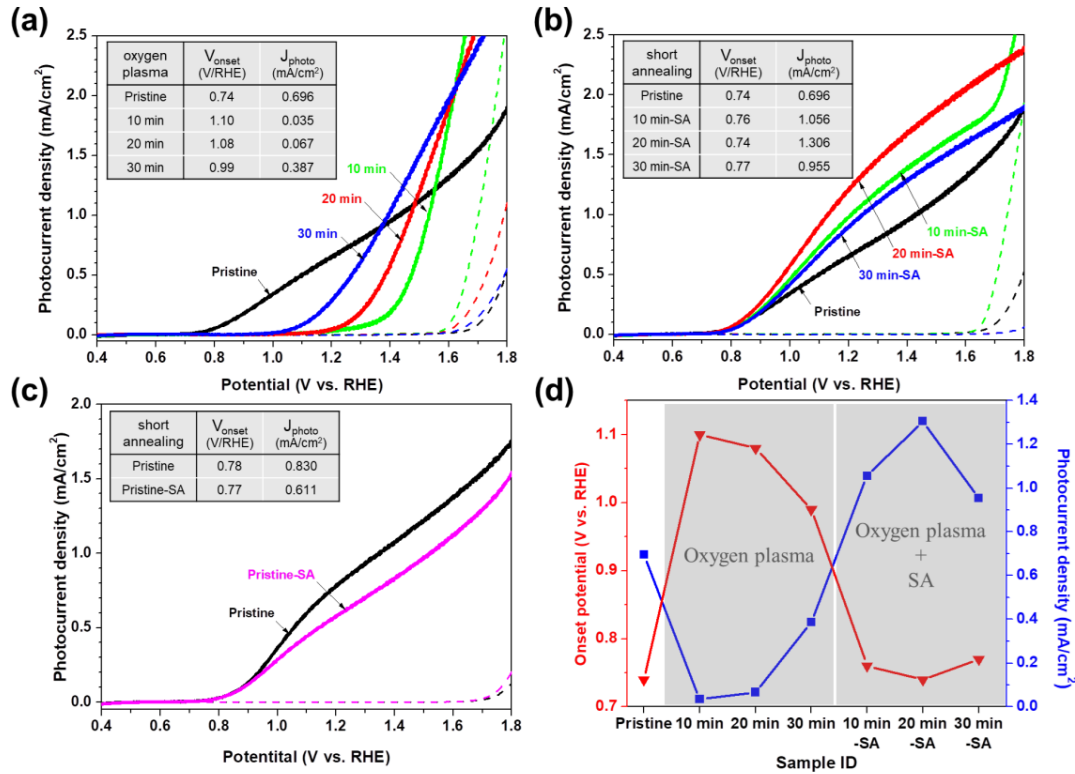


**Figure 16** J-V curves of the prepared hematite photoelectrodes treated with (a) oxygen plasma, (b) oxygen plasma followed by short annealing and (c) only short annealing; (d) a graphical demonstration of onset potential (red) and photocurrent density at 1.23 V vs. RHE (blue) based on insets in (a) and (b).

Morphological changes described above to be correlated with J-V behaviors seem to be insufficient due to following reasons: 1) Although one can argue that back injection of electrons from the exposed FTO area to the electrolyte can be suppressed by particle agglomeration, detrimental photocurrent density at the modest applied bias observed from oxygen plasma treated hematite is not clear. 2) In contrast, nanostructuring of metal oxide photoelectrodes has been drawing tremendous attention due to high surface area contacting to aqueous electrolyte. In this study, however, modified morphology of hematite films by the post-synthesis treatments led to increase in particle size, which would imply decrease in surface area. 3) Moreover, it is vague to elucidate severe shift in onset potential before and after short annealing process when considering no significant morphology shift. For further elucidation, XRD was carried out to evaluate crystallinity of the prepared films. Since it has been revealed that it is highly favorable for electrons to transfer along (110) plane, leading to improved photocurrent.<sup>151,152</sup> For this, the sample treated with the oxygen plasma for 20 min and short annealing was chosen. The XRD

patterns shown in Figure 17 revealed that the as-prepared film exhibited single phase of hematite (PDF 87-1164), corresponding well to characteristic planes of (012), (104), (110), and (024). After the post-synthesis treatment using the oxygen plasma and the short annealing, crystallinity remained identical except silent signal of (024) plane in the oxygen plasma treated one. Thus, bulk crystallinity does not seem to be a major factor responsible for enhanced PEC performance of the prepared photoelectrodes.

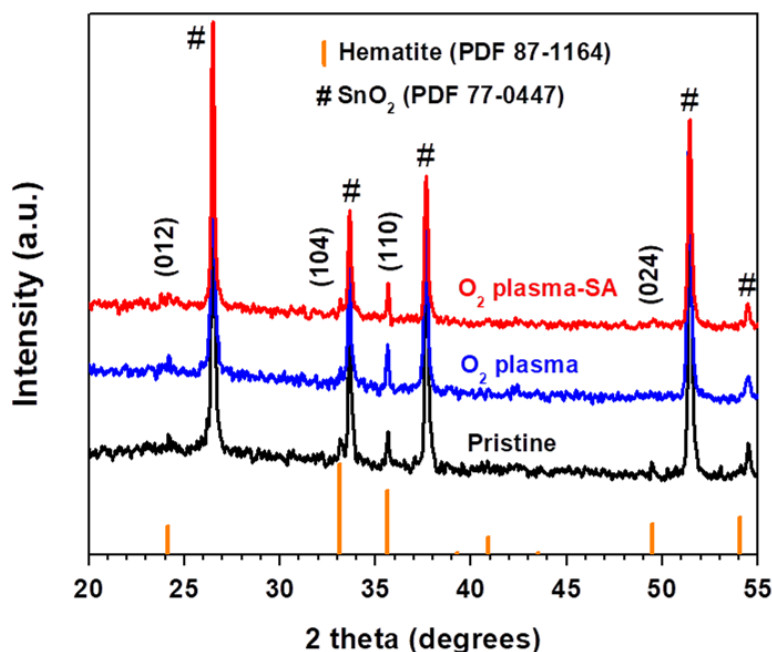


**Figure 17** XRD patterns of the pristine hematite (black), hematite treated with oxygen plasma for 20 min (blue) and oxygen plasma followed by short annealing (red).

Since onset potential can be improved by surface modification as revealed in earlier studies,<sup>153,154</sup> XPS analyses were carried out to verify surface states of the hematite samples. The post-treated samples with the oxygen plasma for 20 min followed by short annealing were chosen. Figure 18 presents high resolution XPS spectra of Fe 2p and O 1s obtained from the hematite samples. In the Fe 2p spectra, distinct peaks arisen at  $\sim 711$  eV (Fe 2p<sub>3/2</sub>) and at  $\sim 724$  eV (Fe 2p<sub>1/2</sub>) with a satellite peak at  $\sim 719$  eV are evidenced as a typical feature of Fe<sub>2</sub>O<sub>3</sub> (see Figure 18a).<sup>155–157</sup>

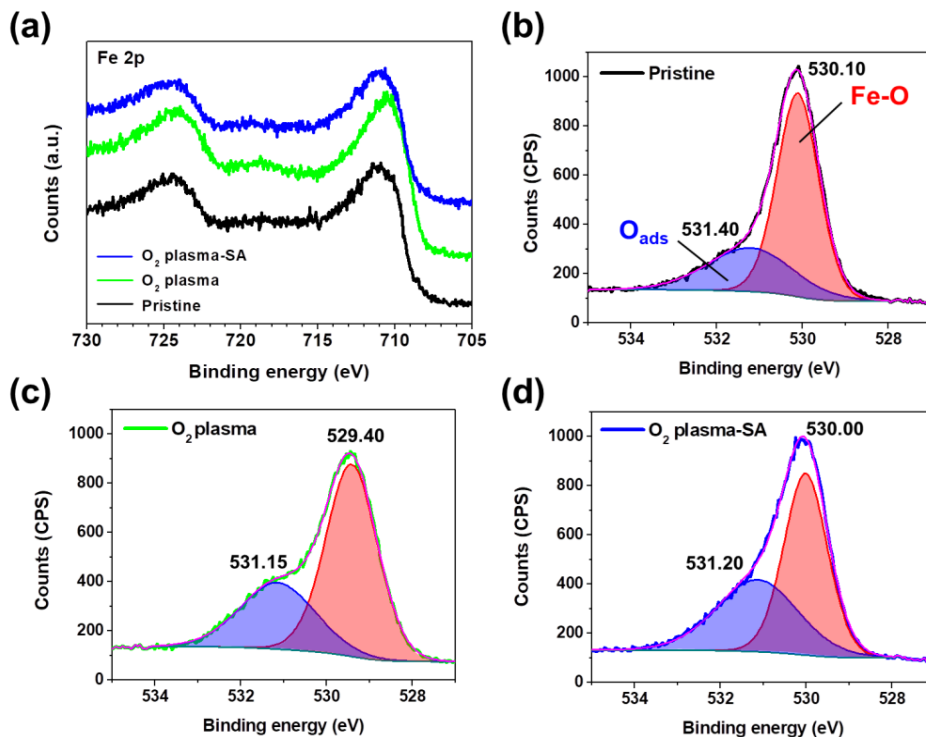
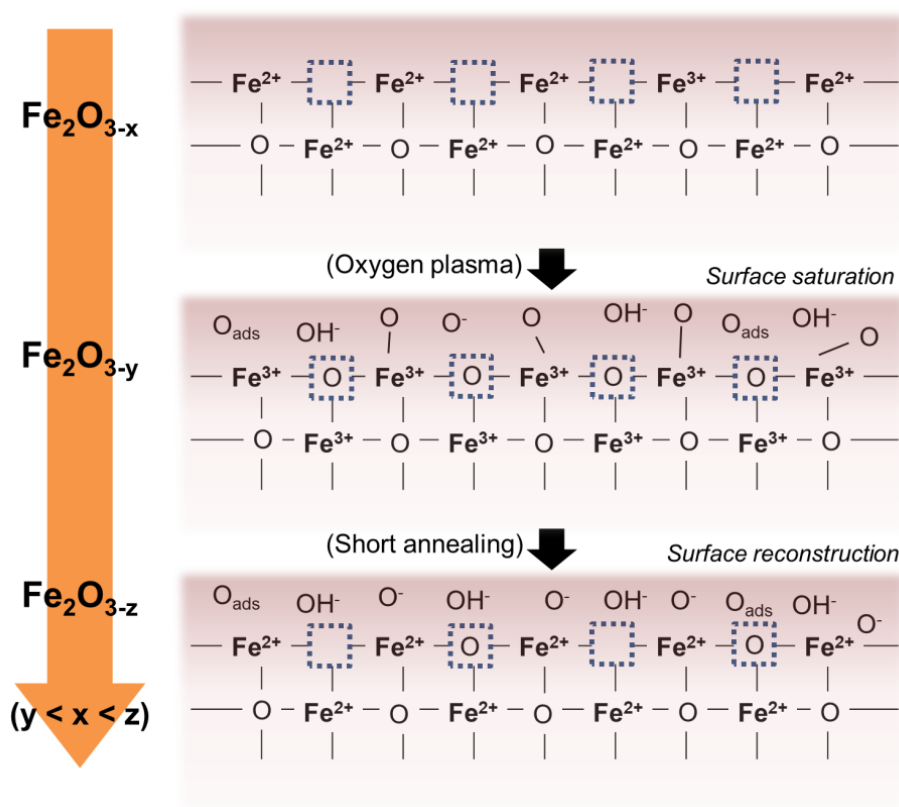


**Figure 18** High resolution XPS spectra obtained from the pristine hematite, the oxygen plasma treated hematite and the hematite treated with oxygen plasma followed by short annealing of (a) Fe 2p and (b, c and d) O 1s.

Likewise, core level of O 1s at 531.10 eV can be assigned to Fe-O bonding and a shoulder peak at ~530 eV is generally accepted as a fingerprint of surface adsorbed oxygen species, denoted as O<sub>ads</sub> in Figure 18b.<sup>155</sup> Comparing the spectra between the pristine and the oxygen plasma treated samples, core level spectra of Fe 2p are shifted to lower binding energies from 710.95 eV to 710.15 eV (Fe 2p<sub>3/2</sub>) and from 724.40 eV to 724.05 eV (Fe 2p<sub>1/2</sub>). Similar to this, core level of O 1s shifted to lower binding energy from 531.10 eV to 529.40 eV. This is regarded as a result of additional electronic charges that were induced by plasma, leading to reduction of electrostatic interaction between nucleus and surrounding electrons. In other words, binding energies of Fe and O core levels might be weakened possibly due to electron rich environment during the plasma treatment. Besides, the satellite peak evolved at ~719 eV that represents the oxidation states of Fe<sup>3+</sup> became prominent upon the oxygen plasma treatment, indicating surface of the pristine hematite could be saturated by oxygen species (Figure 18a) and then they formed Fe-O bonding on the surface, evident in the increased peak area at ~530 eV (from 965.0 to 1194.4).<sup>158,159</sup> However, it is yet to conclude that the Fe-O bonding is a result of surface oxidation on the surface of hematite, considering that removal of electrons from Fe core to oxygen would lead to increased interaction between Fe and surrounding electrons, which ought

to result in chemical shift to higher binding energy. Despite the increased amount of Fe-O upon oxygen plasma the effect of electronic hindrance caused by additional charges might overwhelm to result in chemical shift to lower binding energy, which is also evident in chemical shift of O 1s (see Figure 18c). After the short annealing step, both Fe 2p and O 1s spectra showed chemical shift back to higher binding energy to certain extent. The satellite peak became less noticeable compared with the one after the oxygen plasma treatment. The chemical shift in Fe 2p peak to higher binding energy has been often reported as an evidence for formation of oxygen vacancies.<sup>160</sup> Note that the area of the peak assigned to lattice oxygen ( $O^{2-}$ ) decreased (from 1194.4 to 896.0), indicating that the surface oxygen species could either be lost or migrate inwardly during annealing in ambient.



**Scheme 10** A proposed scheme of the hematite surface during the post-treatments based on XPS analyses.

It is presumable that the pristine hematite (oxygen deficient) becomes saturated by oxygen species induced by oxygen plasma, leading to increased concentration of  $Fe^{3+}$  and filling up intrinsic oxygen vacancies on the surface. This chemically modified surface by the plasma process could impede water oxidation by reducing surface occupancy of Fe centers that were found to be a more favorable water oxidation route than a surface exposed with oxygen



species.<sup>161</sup> When the hematite film treated with oxygen plasma was annealed, this oxygen saturated surface seems to be reconstructed by inducing an optimized amount of oxygen vacancies. It corresponds to the earlier studies that dealt with oxygen vacancies and oxygen deficient hematite for enhanced photoelectrochemical activity.<sup>160,162,163</sup> Based on the surface analyses, the stoichiometry of the hematite surfaces is proposed as  $\text{Fe}_2\text{O}_{3-x}$  for the pristine hematite,  $\text{Fe}_2\text{O}_{3-y}$  for the oxygen plasma treated hematite and  $\text{Fe}_2\text{O}_{3-z}$  for the hematite treated with both oxygen plasma and short annealing, where  $y < x < z$  (see Scheme 10).

To further corroborate J-V behavior submillisecond to second timescale TAS was conducted. It has been widely used as an effective tool, which measures changes in absorbance of the sample upon irradiation by a pulsed laser. This technique allows analyzing recombination, lifetime of charge carriers and trapping states by observing transient signals.<sup>164</sup> Especially, flash-photolysis spectroscopy measurement was carried out in this study. When short pulses of light were incident to material (hematite) an electron gets excited to a higher energetic state and the excited molecule can either relax back to the ground state directly or participate in photoreaction. The transient excited states have their own absorption spectra and these can be monitored via change in intensity of monitoring light.<sup>165</sup> Figure 19 displays transient decays obtained from the selected samples as a function of wavelengths of probe lights at an applied potential of 1.50 V vs. RHE. At the wavelengths of 575 nm and 650 nm, transient decays possess two distinct features: 1) a negative absorption band that forms in the nanosecond to microsecond scale peaking at 575 nm,<sup>166</sup> which is assigned to electron trapping into localized states near the conduction band edge<sup>166-168</sup> and 2) a broad positive absorption band observed at 650 nm, exhibiting a lifetime in hundreds of milliseconds timescale, which is only visible under anodic bias.<sup>169,170</sup> From the hematite sample treated with oxygen plasma for 20 min, the transient absorption amplitude at 0.1 ms drastically increased ( $-1.73 \times 10^2 \mu\text{OD}$ ) compared to that of the pristine sample ( $-2.6 \times 10 \mu\text{OD}$ ) at 575 nm. Besides, the transient signal probed at 650 nm exhibited approximately two times higher amplitude for the oxygen plasma treated hematite ( $1.13 \times 10^2 \mu\text{OD}$ ) than for the untreated hematite ( $5.9 \times 10 \mu\text{OD}$ ). It is generally accepted that the increased absorption amplitudes at 575 nm and at 650 nm suggest an increased amount of electron trap states and an increased yield of long-lived photoholes, respectively.<sup>163</sup> Upon short annealing on the oxygen plasma treated hematite a slight decrease in the transient absorption amplitude ( $-1.03 \times 10^2 \mu\text{OD}$ ) at 575 nm along with recovery of absorption amplitude at 650 nm ( $5.9 \times 10 \mu\text{OD}$ ). This diminution in amplitude at 575 nm and complete recovery of absorption at 650 nm indicate reduced number of electron trap states. Hence, improved photocurrent density from the shortly annealed hematite compared to that from the sample treated only with oxygen plasma can be corroborated.

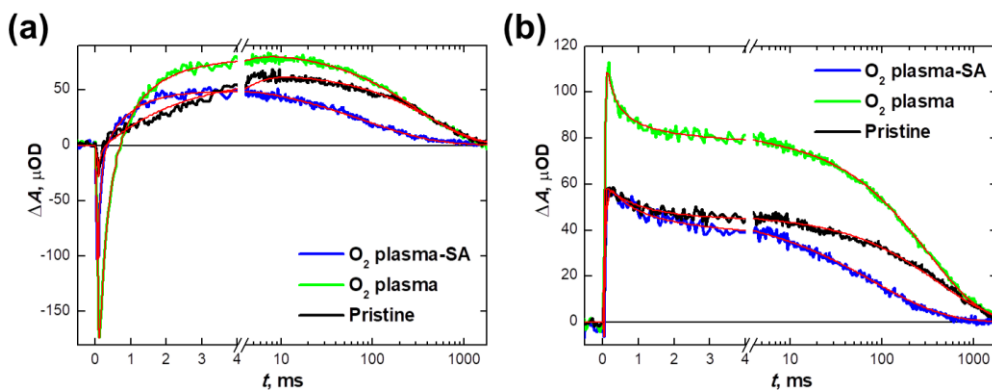


**Figure 19** Transient absorption decays at an applied voltage of 1.50 V vs. RHE, probed (a) at 575 nm and (b) at 650 nm.

In addition to qualitative evaluation analyzed by the transient decays, water oxidation rates of the prepared samples were determined at 1.50 V vs. RHE with a probed wavelength of 650 nm (data not shown, refer to Ref. 170). While the pristine (mean lifetime of 510 ms) and the oxygen plasma treated hematite (mean lifetime of 390 ms) photoanodes exhibited the water oxidation rate of  $2.0 - 2.5 \text{ s}^{-1}$ , the hematite annealed shortly after oxygen plasma showed  $\sim 7.1 \text{ s}^{-1}$  (mean lifetime of 140 ms). When considering almost same yield of long-lived holes seen in the pristine and the annealed sample (45 and 48  $\mu\text{OD}$ , respectively) higher water oxidation rate indicates that the catalytic activity of the annealed sample outperforms the pristine hematite, which resulted in superior photocurrent density seen in Figure 16b.

### 3.1.2 Post-synthesis treatment of hematite via argon plasma

A further work was conveyed by applying argon (Ar) plasma that provides non-oxidative atmosphere unlike oxygen plasma. It was expected that the surfaces of hematite films are subjected to mainly physical disturbance given by Ar plasma. By evaluation of the hematite surfaces treated with Ar plasma followed by short annealing, identically applied as the previous part, the role of post-synthesis treatment consisting of oxygen plasma and short annealing could be highlighted. Figure 20 presents J-V curves of the prepared samples as a function of duration of Ar plasma. All hematite films exhibited severe anodic onset potential shifts as observed in Figure 16a. Upon rapid thermal treatment, the onset potential of the films shifted back almost identical to that of the pristine sample. In case of photocurrent density, it appears that when the hematite film was exposed to Ar plasma for longer time, photoresponse became similar to that of the pristine. However, the effect of energetic disruption on PEC performance is not as effective as that of oxygen plasma. It seems that chemical modification induced by oxygen plasma on the

hematite surface played a critical role in PEC performance.

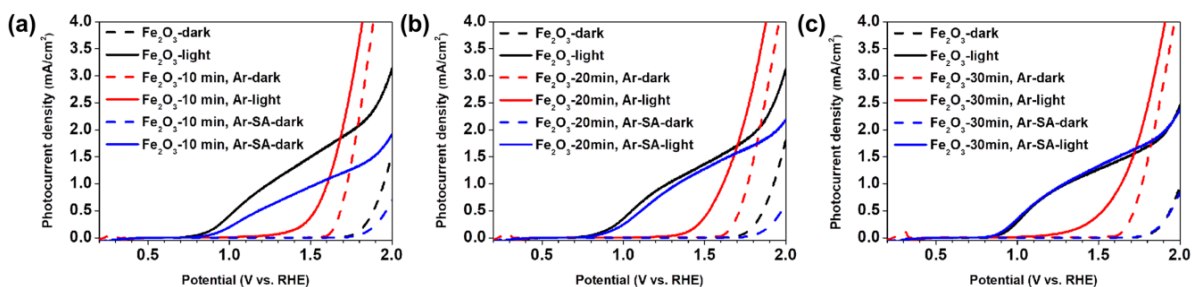


**Figure 20 J-V curves of the hematite photoanodes that were treated with Ar plasma for (a) 10 min, (b) 20 min and (c) 30 min followed by short annealing.**

Non-oxidizing nature of Ar plasma was proven by high resolution spectra of Fe 2p given in Figure 21. Unlike the case in the oxygen plasma treated hematite, no evolution of satellite peak at  $\sim 718$  eV was observed in spite of analogous anodic onset potential shift. From this, the chemical states of hematite surface are strongly dependent on the plasma environment. Hence, the electron trapping states observed from the hematite treated with oxygen plasma are ascribed to surface defects induced by energetic ion bombardment. The recovery of onset potential shift after the short annealing process indicates that the defective surface of hematite films acting as efficient recombination sites could be relaxed. Moreover, the satellite peak that is an evidence of existence of  $\text{Fe}^{3+}$  became noticeable after the short annealing step, which could be resulted from partial oxidization in ambient. It is interesting to note that depending on the plasma environment a variety of chemical states can be formed and it can significantly affect photoelectrochemical property of hematite.

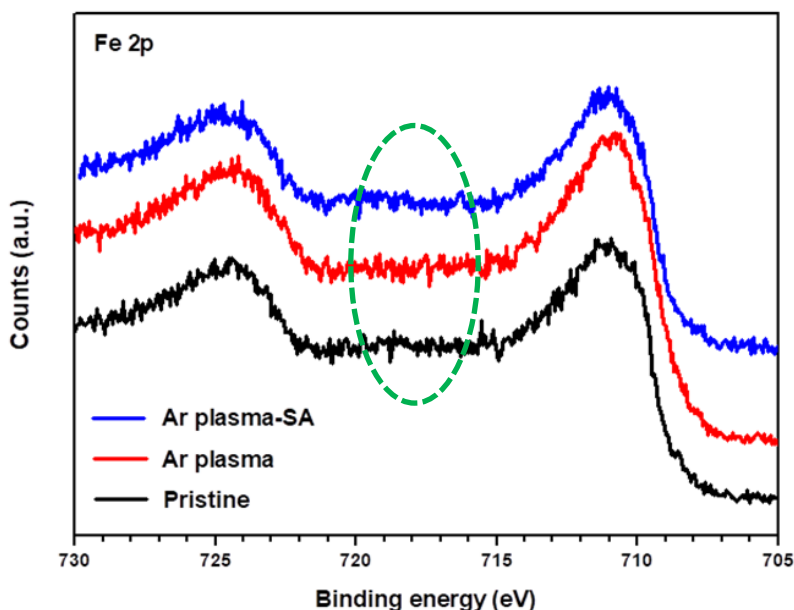


**Figure 21** High resolution XPS spectra of the post-treated hematite photoanodes with Ar plasma.

### 3.2 Conclusions

A pristine hematite film synthesized by PECVD exhibited porous particulate structure. Interestingly, plasma treatment led to promotion of particle growth and the size of agglomerates further increased as the plasma treatment became prolonged. Besides, despite no significant morphology shift upon short annealing, noticeable J-V characteristics were observed with respect to the post-synthesis treatment. The XPS analyses revealed that the oxygen plasma induced oxygen saturated surface which impeded water redox reaction, whereas the short annealing might reconstruct the surface either by inward diffusion of oxygen species or by removing surface adsorbed oxygen species. The designed surface model based on qualitative/quantitative analyses on high resolution spectra of Fe 2p and O 1s suggests the surface of hematite transforms into the optimum status exhibiting improved PEC performance. TAS corroborated J-V characteristics of the prepared hematite films, providing information about water oxidation rate. The oxygen plasma treatment yielded defect sites that are efficient recombination sites, and yet the following annealing reduced back electron recombination resulting in onset potential recovery and enhanced photocurrent density. Moreover, the surface defects generated by ion bombardment in plasma seemed to be a cause of deteriorated PEC activity, which was deductively evidenced by Ar plasma treatment followed by short annealing. In short, similar anodic onset potential shift was also observed from the Ar plasma treated hematite of which surface states remained unchanged. No enhancement in photocurrent density upon short

annealing suggests that preceding surface environment is crucial for PEC performance. However, more systematic investigation on Ar plasma treated hematite photoanodes is required.

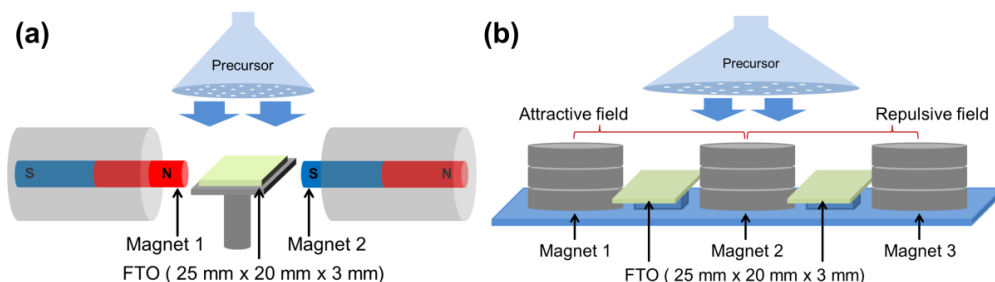


## 4 In-situ modulation of thin film growth by external magnetic fields

### 4.1 Motivation and background

The last strategy to modify metal oxide films deposited by PECVD in this study was to employ commercial magnets into PECVD processes. A number of studies to improve certain properties of metal oxides has been conducted by introducing magnetic fields into process environment.<sup>171,172</sup> For instance, magnetic nanostructures of Co and Ni were synthesized with help of magnetic field and their electromagnetic properties were improved due to aligned structure.<sup>173</sup> Earlier, synthesis of Ni particles with controlled morphology was successive and the shape of particles strongly depended on the strength of magnetic field at moderate temperature.<sup>174</sup> A representative magnetic metal oxide,  $\text{Fe}_3\text{O}_4$  (magnetite), was synthesized by a facile thermal decomposition method under the static magnetic field. The magnetite nanoparticles synthesized under the magnetic field exhibited clear cubic structure with good size uniformity whereas the counter group obtained without the magnetic field showed the shape of nanocuboctaheron.<sup>175</sup> While the above examples dealt with wet chemical methods, a static magnetic field was introduced in PECVD for investigating the influence of external magnetic fields on gas phase deposition of (non)magnetic metal oxides.

Two types of experimental apparatus were designed depending on type of magnets used. Magnetic fields induced by rod-type magnets (N45,  $\text{Nd}_2\text{Fe}_{14}\text{B}$ , adhesive force  $\sim 6.5$  kg) and disk-type magnets (Y30,  $\text{SrO}_6 \cdot \text{Fe}_2\text{O}_3$ , adhesive force  $\sim 1.1$  kg) were tested as illustrated in Scheme 11a (a detailed description of the setup will be given in section 5.3.1) and Scheme 11b, respectively. The preparation of the setup in Scheme 11b was motivated not only to figure out how the dimension of magnetic field in PECVD affects the growth of films, but also to produce samples under different magnetic fields (attractive/repulsive) in a single PECVD process.



**Scheme 11 Illustrations of the experimental setups for PECVD processes, employing (a) rod-type and (b) disk-type magnets.**

#### 4.1.1 Effect of magnetic fields on a magnetic oxide (hematite)

Deposition of  $\text{Fe}(\text{CO})_5$  in PECVD was carried out with- and without magnets. As plasma environment is significantly affected by geometry of reaction chamber, consequently influencing on the film growth, reference samples were produced with existence of supporting apparatus only without magnets mounted. Figure 22 presents photographs of glow discharge generated under the magnetic fields. Plasma generated by a r.f. power of 20 W formed distinguishable features depending on the magnetic fields, which consequently affected local density of plasma. Hence, it appeared that the plasma on the substrate under the attractive field was more concentrated than under the repulsive field.

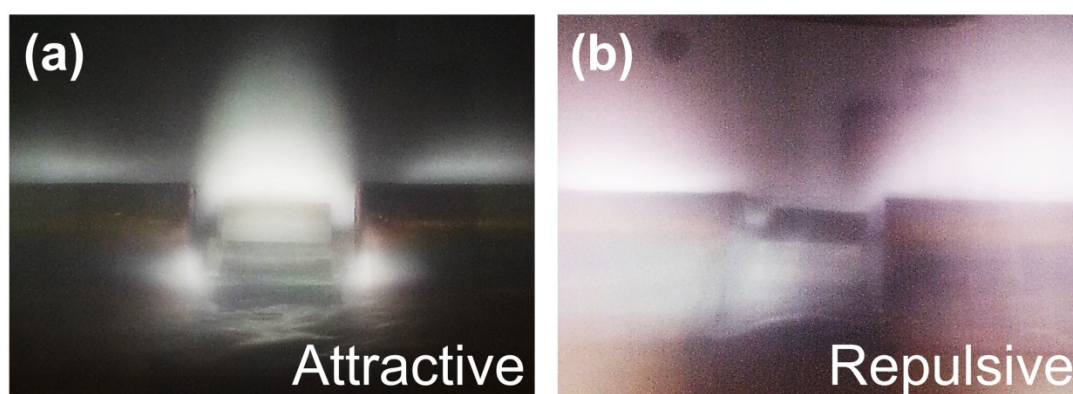


**Figure 22** Photographs of the plasma generated under (a) the attractive field and (b) the repulsive field, induced by rod-type magnets.

Hematite films deposited under various process parameters that consist of deposition time and applied magnetic fields are presented in Figure 23 with SEM images. Interestingly, hematite films grown under the magnetic fields seem to exhibit faster deposition rate, which can be estimated by darkness of the films obtained from 5 min processes. This variation in growth rate of the films can be mainly ascribed to r.f. bias<sup>29</sup> that was affected by presence of magnets. Briefly, lower r.f. bias was detected when the magnets were placed on the anode and a diagnostic procedure, seeking to the influence of magnets on the working process will be described and reported in the experimental section (refer to the Chapter 5). It is crucial for photoelectrodes in PEC water splitting since the balance between light absorption and bulk recombination is one of the important aspects.



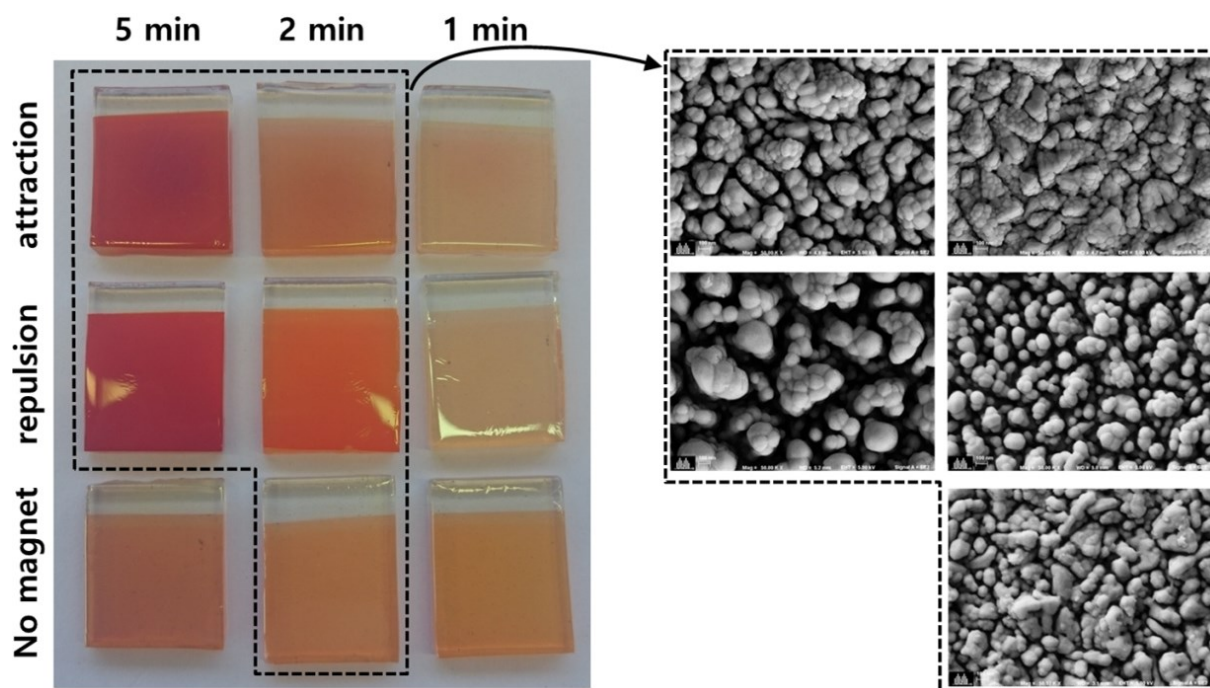


**Figure 23** Hematite films coated on FTO substrates from different parameters, including applied magnetic fields and deposition time and corresponding surface morphologies of the selected films.

PEC activities of the hematite films deposited under various conditions were determined by measuring photocurrent in the 3-electrode system identical to the previous sections and their J-V curves are plotted as a function of magnetic fields and deposition times (Figure 24). Besides, Figure 25 demonstrates the photocurrent density values at the water redox potential to clearly visualize performance tendency. In 1 min process, the highest photocurrent density at 1.23 V vs. RHE was obtained from the reference sample ( $0.406 \text{ mA/cm}^2$ ) compared to those deposited under the attractive field ( $0.206 \text{ mA/cm}^2$ ) and the repulsive magnetic field ( $0.105 \text{ mA/cm}^2$ ). However, when the deposition time increased to 2 min, the repulsive magnetic field appeared to fabricate the most efficient hematite film exhibiting  $0.659 \text{ mA/cm}^2$  ( $0.484 \text{ mA/cm}^2$  for the reference and  $0.278 \text{ mA/cm}^2$  for the attractive field). On the contrary, no favorable effect of magnetic fields on PEC performance was observed from 5 min process ( $0.406$ ,  $0.208$  and  $0.105 \text{ mA/cm}^2$  for the reference, the attractive field and the repulsive field, respectively). It points out necessity of considering various process parameters in search of the optimum conditions.

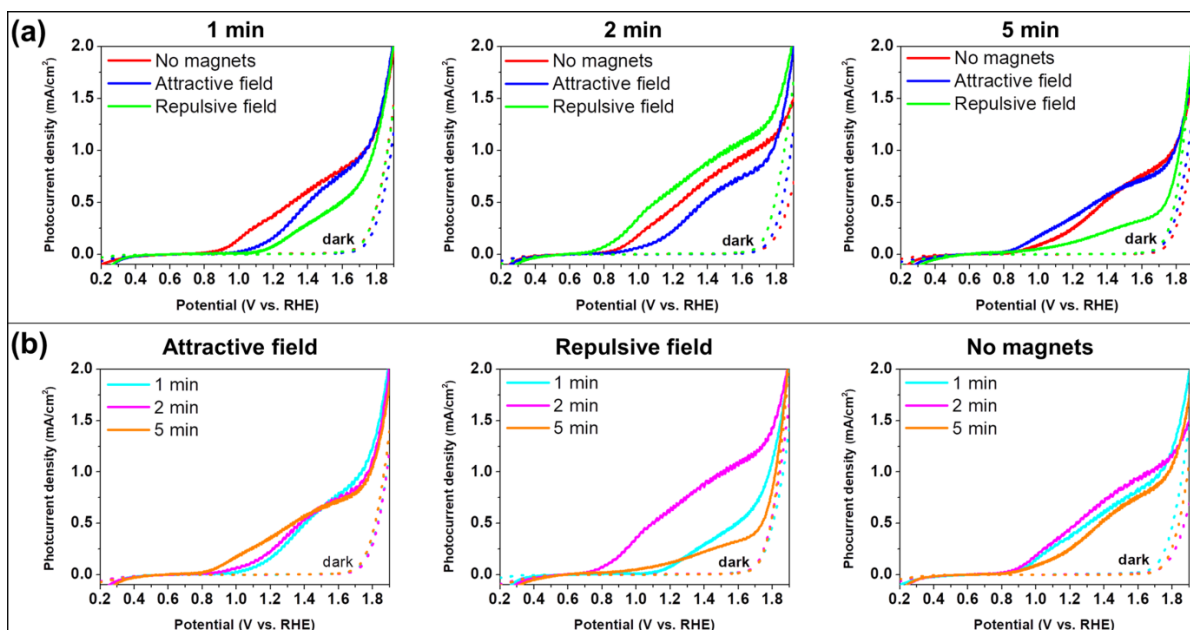


**Figure 24** J-V curves plotted as a function of (a) magnetic fields at a fixed deposition time and (b) deposition times under specific magnetic fields.

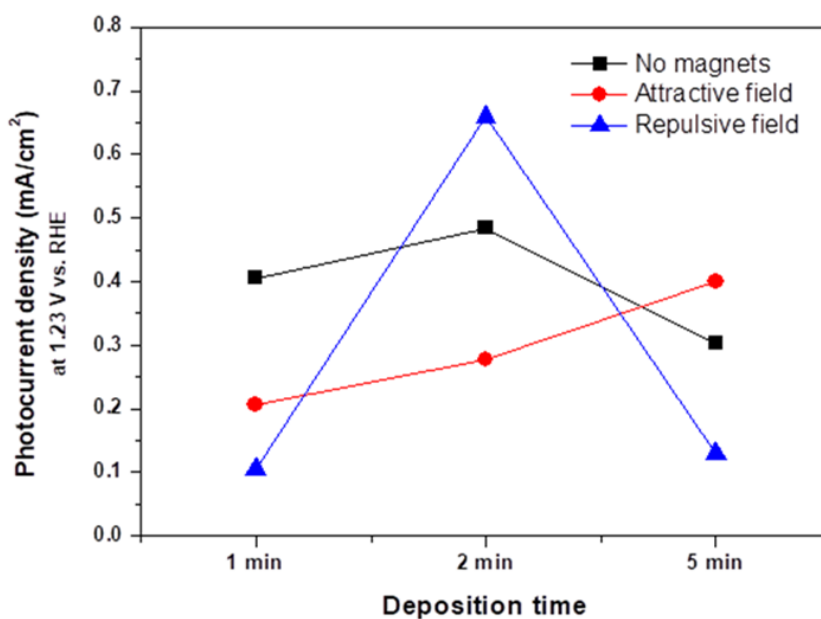


**Figure 25** Photocurrent density values (at 1.23 V vs. RHE) of the prepared hematite films.

The films were investigated by SEM and are shown in Figure 26, which contains surface morphologies of the hematite deposited for 2 min. Noticeable change in morphology of particles has been achieved by altering polarity of magnets in PECVD process. While particles with irregular shape were formed on the reference sample, particles with homogeneous size of ~70 nm were agglomerated under the attractive magnetic field, which led to dense structure. When

the substrate was placed in the repulsive magnetic field, highly porous hematite particles with facets (marked with white arrows in Figure 26c). It is intriguing to correlate with the J-V curves shown in Figure 24a (middle, 2 min) that this porous morphology could possibly be favorable for water redox reaction since it is widely accepted that high surface area of photoelectrode provides better performance in PEC water splitting. Moreover, the lowest onset potential ( $\sim 0.7$  V vs. RHE) observed from the sample prepared under the repulsive field is ascribed to enhanced water oxidation kinetics, evidenced by the lowest dark onset potential.

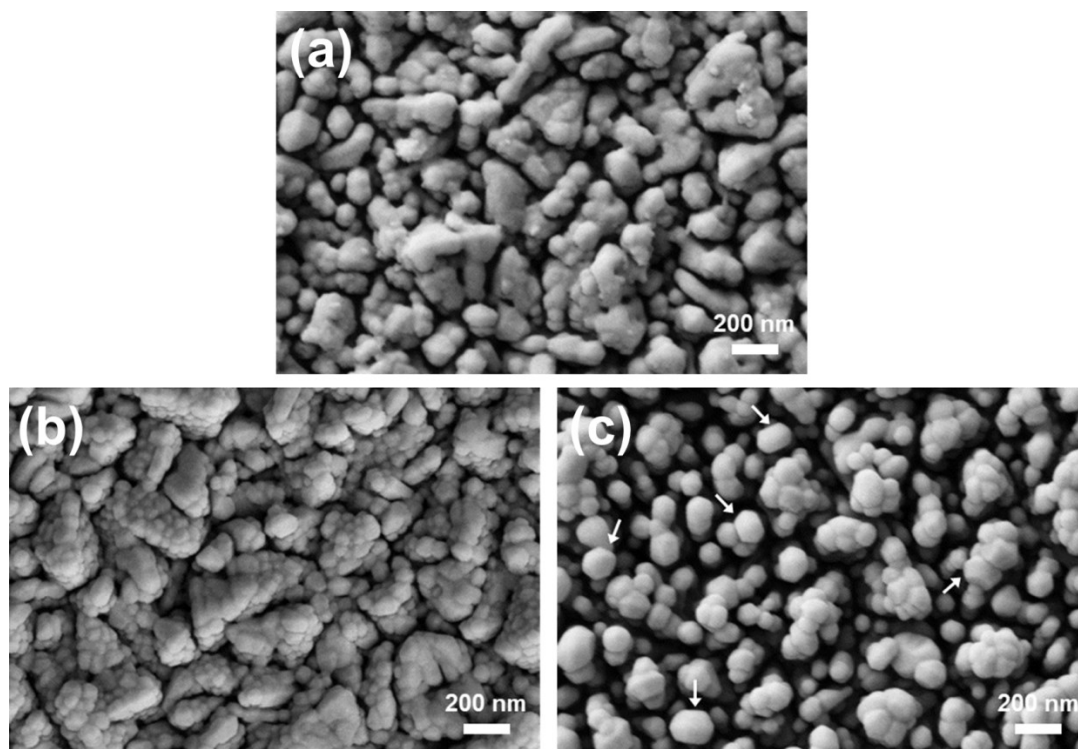


**Figure 26** Surface morphologies of the hematite films deposited for 2 min (a) without magnets, (b) under the attractive field and (c) under the repulsive field.

When the PECVD process was prolonged to 5 min, hematite particles tended to grow larger as seen in Figure 27. In both attractive and repulsive fields, voids formed among particle agglomerates became bigger than films deposited for 2 min, which indicated the growth of hematite particles take place in perpendicular direction to the substrate. This preferred orthogonal growth of film to the substrate is proven in Figure 27c and Figure 27d, which shows increased thickness of columnar structure. Besides, faceted structure of particles seems to collapse with increased deposition time under the repulsive field (compare Figure 26c and Figure 27b). Despite absence of an image taken from 1 min deposited sample under the repulsive field, it might be worthy to note the PEC behavior previously shown in Figure 24b (middle). Severe cathodic onset shift ( $\sim 0.4$  V vs. RHE) was marked from the 2 min sample compared with the 1 min

sample and the improved onset behavior of hematite has been reported as a result of improved water oxidation kinetics, which was also verified by TAS analysis in the earlier section. However, all samples exhibited almost same dark onset potentials; which implies electrocatalytic activity does not seem to be responsible for cathodic shift in light onset potential. In general, the onset potential under the dark condition is an indicator of electrocatalytic activity, i.e. the lower dark onset, the better electrocatalytic activity. So, the cathodic shift in onset potential might come from preferable morphology, for instance, reduction of back recombination by decreasing the direct contact area between FTO and the electrolyte along with increased light absorption. On the contrary, decreased photoactivity of the 5 min sample compared with 2 min one might be due to increased bulk recombination despite increased light absorption. Based on this observation on changing film structure, one can derive importance of aforementioned balance between the thickness and charge carrier dynamics as well as morphology of films.

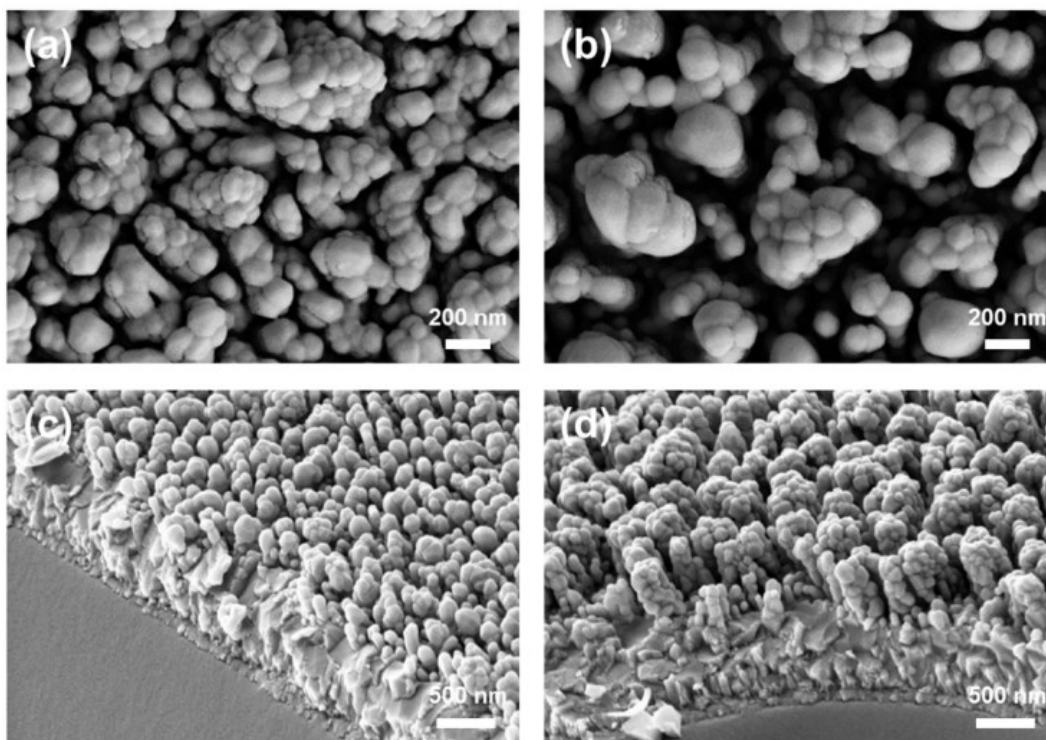


**Figure 27** Surface morphologies of the hematite films deposited under (a) attractive field and (b) repulsive field with deposition time of 5 min; Tilted side view images of the films under the repulsive field for (c) 2 min and (d) 5 min.

In addition to the morphological investigation, crystallinity of the hematite films was examined to explore the effect of internal magnetic fields on films' property. Hematite films produced by 2 min PECVD process were chosen and their XRD patterns are displayed in Figure 28. The pristine hematite film showed a typical crystalline feature of hematite (PDF 87-1164) without

any other phases of iron oxides. However, when there was an attractive magnetic field applied around the substrate, the film did not exhibit the signal of (110) plane while that of (104) plane was predominant. This is a meaningful result to correlate with J-V characteristics of these films since the electrical conductivity along (110) plane is 4 times higher than that along (104) plane.<sup>152</sup> So, the absence of (110) plane growth under the attractive field might result in lower photocurrent density of the film, comparing with the other photoanodes.

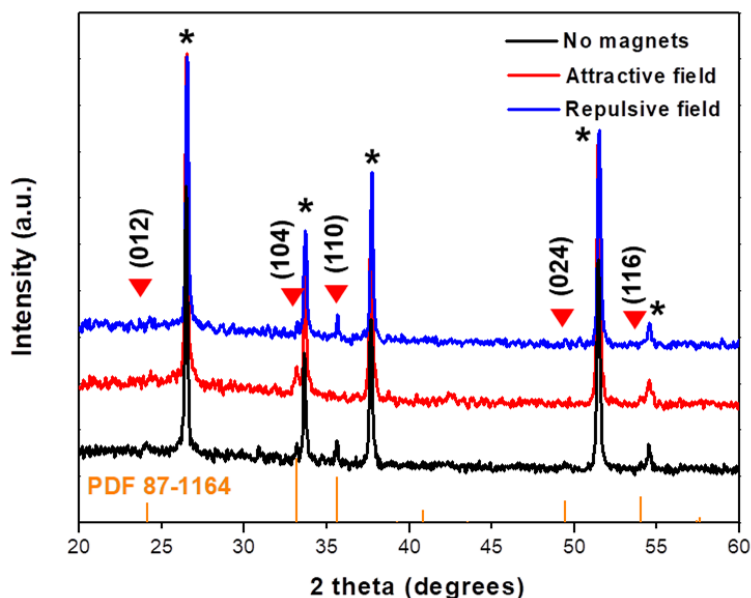


**Figure 28** XRD patterns of the hematite films deposited for 2 min under different magnetic fields. Asterisks (\*) represent SnO<sub>2</sub> (PDF 41-1445) from FTO substrates.

In a second set of experiment, disk-type magnets were stacked and used to apply a different geometry of magnetic field (see Figure 29). When this magnet stack consisting of 3 disk magnets were placed in the PECVD chamber, toroidal shape of plasma was generated. To evaluate the film's growth, substrates (FTO, Si wafer) were placed on (P0) and beside (P1) the magnet stack, where the density and the geometry of plasma were expected to be different.

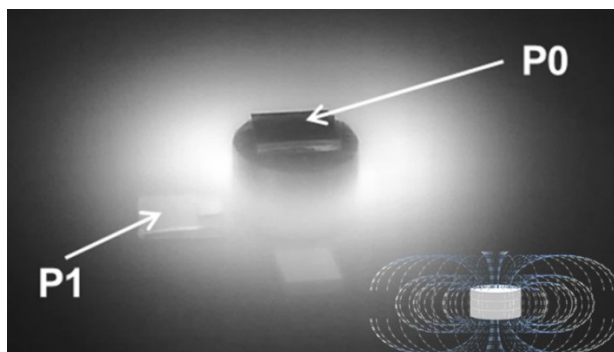


**Figure 29** A photograph of an experimental setup using stacked disk-type magnets with samples placed at different positions and an inset illustrating the expected magnetic flux lines.

Figure 30 shows surface morphologies of the hematite films, prepared at P0, P1 and without the magnet stack as a reference sample. The reference sample (Figure 25a) exhibited mesoporous structure,<sup>176</sup> consisting of spherical particles necking each other with size range of 100~200 nm. The samples deposited with the stack of magnets showed distinct surface textures; much finer hematite particles were observed from the film deposited at P0 and dense film was fabricated when the substrate was placed at P1. It is regarded that characteristic plasma environment evolved by magnetic field surrounded would consequently affect the films' morphology.

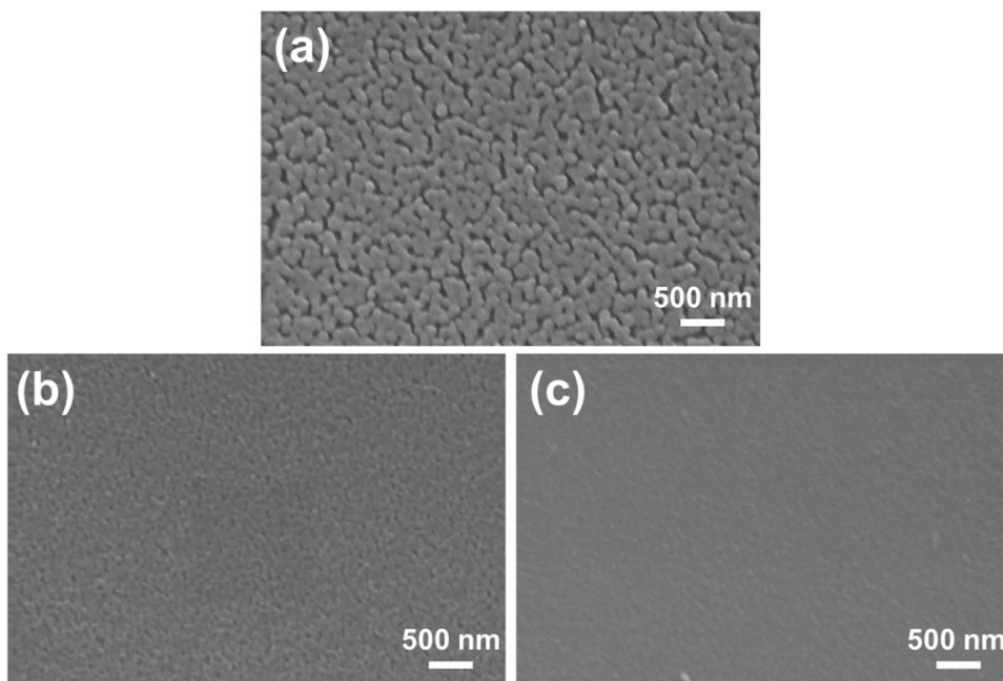


**Figure 30** Surface morphologies of the hematite films deposited on Si wafers (a) without magnets, (b) at P0 and (c) at P1.



Crystallinity of the films deposited on silicon wafer was evaluated by XRD with a grazing incidence mode and their patterns are presented in Figure 31. The reference sample was revealed as hematite (PDF 84-0308) with typical peaks well assigned to its characteristic lattice planes. However, certain peaks such as (012) and (113) were clearly found to be silent from the P1 sample. Meanwhile, a signal of (006) plane was suppressed when the film had been grown on the magnet stack. Thus, the plasma with toroidal shape that was confined by the magnet stack was able to modify the crystallinity of the hematite. It was interesting to further estimate water splitting performance of these samples since the crystallinity and the morphology are of factors that influence on PEC performances.

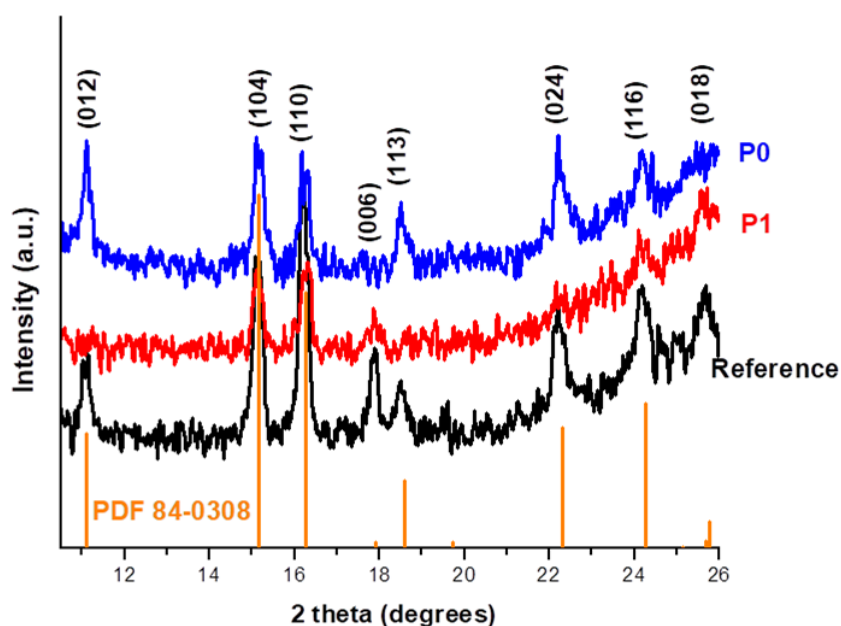


**Figure 31 Crystallinity of the hematite films prepared with a stack of disk-type magnets.**

J-V curves measured from the 3 samples, consisting of the reference, P0 and P1, are shown in Figure 32a. Favorable performance in PEC water splitting was obtained from the sample P0 that was grown on the magnet stack whereas poorer performance was observed from the sample P1. The sample P0 exhibited almost linear behavior with light onset potential of  $\sim 0.75$  V in contrast to lagged increase in photocurrent from the reference and P1 samples. The low onset potential is ascribed to accelerated surface water oxidation kinetics, which is also evidenced by low dark onset (red dashed line) as discussed earlier. Although it is not straightforward to correlate the PEC behavior with morphology and crystallinity directly, the microstructure and the crystallinity turned out to be clearly modified by the stack of magnets. It implies that magnetic field is effective to modulate properties of metal oxide films gas phase deposition. A supplementary experiment was conducted to rule out the effect of process geometry on PEC performance of

hematite. For this purpose, a metal (Al, aluminum) block with same shape and dimension ( $\varnothing$  30 x 18 mm) as the magnet stack was fabricated and the deposition of  $\text{Fe}(\text{CO})_5$  was carried out under the same process conditions. Expectedly, the plasma glow generated surrounding the Al block homogeneously covered a whole area of the chamber electrode. The hematite films deposited at P0 and P1 performed almost identically as shown in Figure 32b, indicating the deviation in PEC performance originates from the confined plasma by magnets rather than geometric conditions. Onset potential values were determined as  $\sim 0.8$  V vs. RHE for both hematite photoanodes deposited at P0 and P1. Moreover, photocurrent density values at 1.23 V obtained from those photoanodes were  $\sim 0.25$  mA/cm<sup>2</sup>, which are lower than that of the hematite photoanode produced at P0 in the presence of the magnet stack ( $\sim 0.40$  mA/cm<sup>2</sup>).

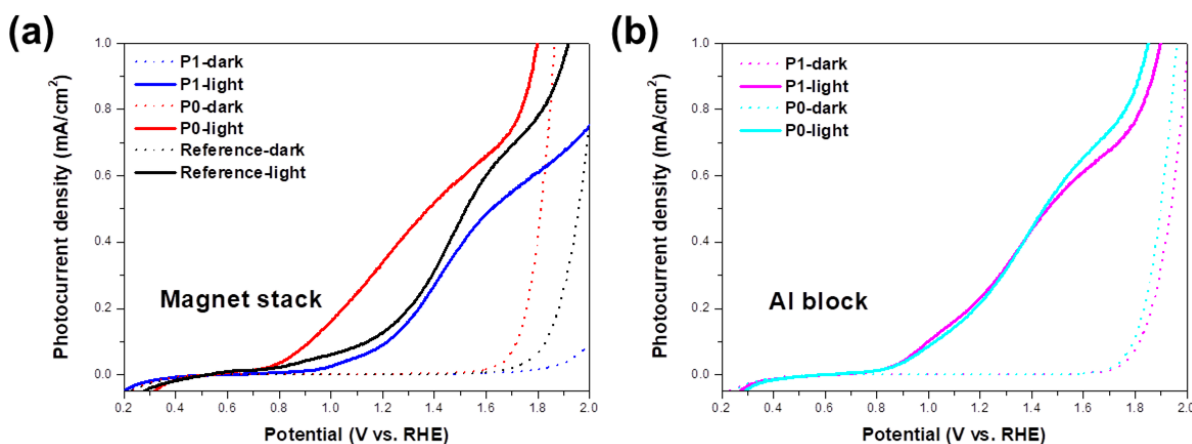


**Figure 32 J-V curves obtained from hematite films synthesized with (a) the magnet stack and (b) Al block.**

Using this magnet stack, an apparatus was designed as presented in Scheme 11b. This configuration enabled to induce the attractive and the repulsive field simultaneously and the operational artifacts in PECVD process could be ruled out. Characterization of the magnetic fields was carried out by a magnetometer not only determine the field strength but also to estimate magnetic flux lines roughly. The field strength recorded where the magnet stacks attract each other as 3.3 mT (Figure 33a) and 19.0 mT (Figure 33b) in perpendicular and in parallel to the substrate, respectively. It indicates that the magnetic flux in parallel direction was predominant where the attractive field was applied. The spot between the magnet stacks that repel each other exhibited 33.4 mT with perpendicular magnetic flux whereas no field was detected in parallel direction to the substrate (Figure 33c and Figure 33d).



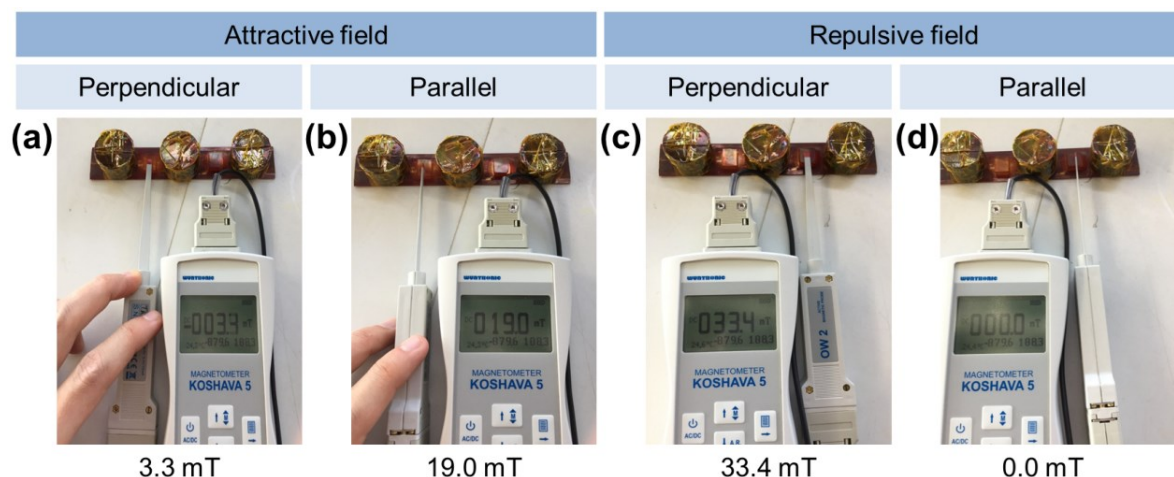


**Figure 33 Determination of magnetic field strength using the magnetometer where (a and b) the attractive force and (c and d) the repulsive force exist between the magnet stacks.**

Figure 34 shows a photograph of the PECVD process, carried out with the set of magnet stacks as well as a scheme of the expected magnetic flux lines. The feature of confined plasma glow exhibited a trace of magnetic field as observed in the previous part. In addition to the toroidal shape around the individual stack, characteristic formation of plasma influenced by the attractive and the repulsive interaction between the stacks was observed, which corresponds with magnetic field strength and flux directions determined above. The resultant surface morphologies of hematite films grown on FTO substrates are presented along with an image obtained from a reference sample in Figure 35. The reference sample that was prepared without existence of magnets. More porous surface structure was obtained from the reference sample that was prepared without any magnets, which can be clearly comparable in Figure 30 (upper row). The magnetic field appears to restrain orthogonal growth of films, resulting in dense/compact structure, which was also observed in the earlier case employing one stack of magnets. When looking into the morphologies of the films produced simultaneously under different plasma environment where the attractive and repulsive interactions were built, texture of the aggregates revealed to be slightly different. Primary particles synthesized under the attractive field formed rather smooth aggregates resulting in fewer amounts of granular boundaries (Figure 35b), while a certain extent of aggregates with clear boundaries was observed from the sample that had been placed under the repulsive field (Figure 35c).

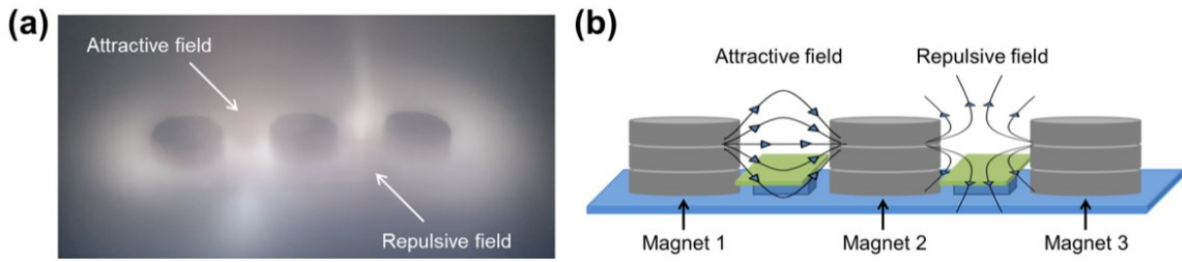


**Figure 34** (a) A photograph taken during a PECVD process with the set of magnet stacks and (b) a simplified scheme of the expected magnetic flux lines.

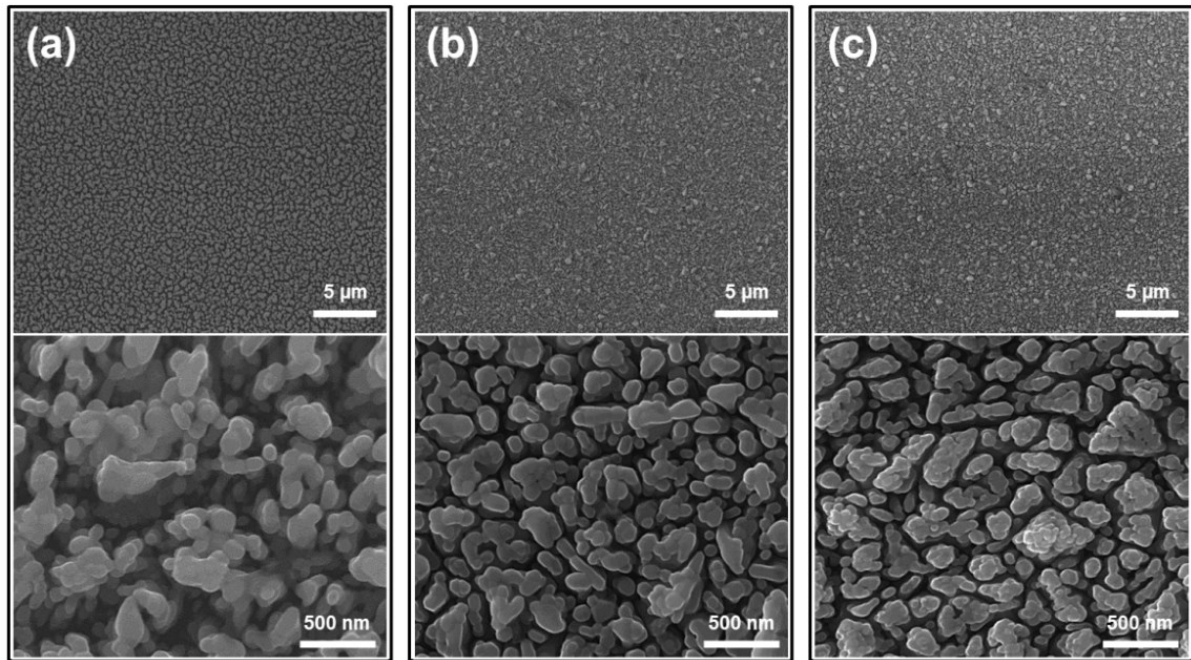


**Figure 35** Surface morphologies of the hematite films prepared on FTO substrates under different plasma environment, formed by the designed configuration with magnet stacks; (a) without magnets, (b) under the attractive field and (c) under the repulsive field.

Figure 36 displays XRD patterns of the films on silicon wafers with a grazing incidence mode (incidence angle of X-ray beam =  $2.5^\circ$ ). There were missing signals of (006) and (113) planes from the reference sample, which is dissimilar to the XRD pattern of the reference shown in Figure 31. It is a deviation between practical PECVD processes and ideal expectations that the process parameters must guarantee reproducibility, which does not seem to be the case seen here. Nevertheless, it is still worth to analyze the XRD patterns of the samples that were synthesized under the magnetic fields and a (104) plane oriented characteristic was observed, whereas the reference hematite exhibited both reflexes of the (104) and the (110) planes. Moreover, there was a small discrepancy in the intensity of the (110) plane between the hematite deposited under the attractive and the repulsive field that no sign of (110) reflex was seen in the red pattern. It

indicates that depending on the geometry of the magnetic flux, crystallinity of the films could be affected to a certain extent.

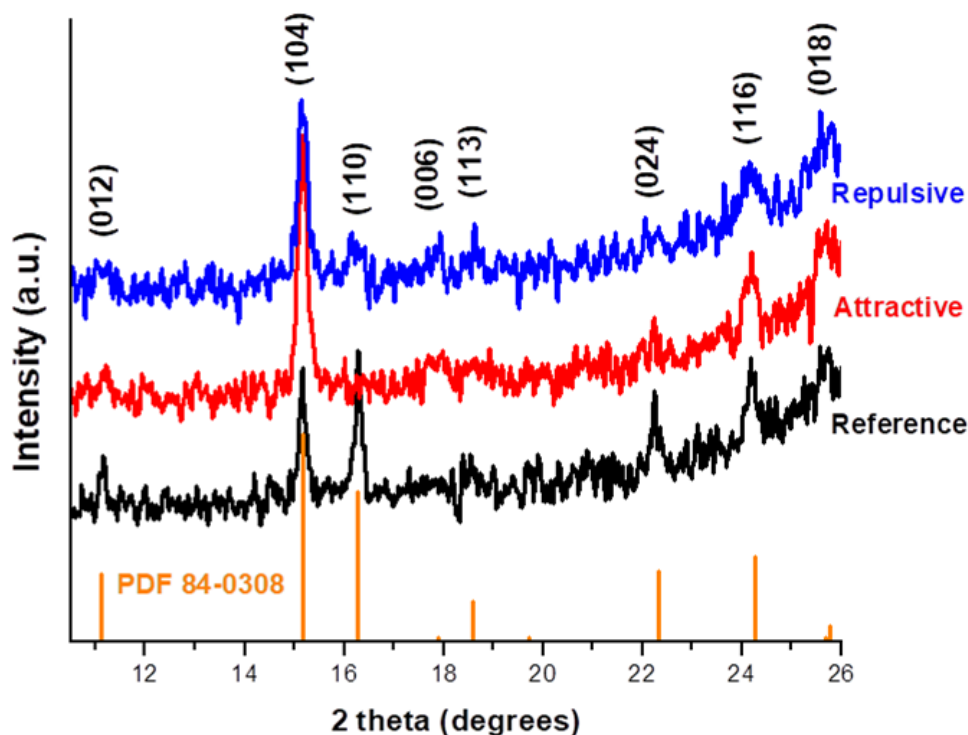


**Figure 36 XRD patterns of the films prepared with the set of the magnet stacks.**

The hematite photoanode produced under the attractive field outperformed the other samples in PEC activity (see Figure 37). It indicates the attractive field offered preferable deposition environment to deposit better performing hematite photoanode under the tested conditions. Since the porosity of the films deposited under both attractive and repulsive fields appeared to be analogous, the smooth surface (Figure 35b) might be advantageous for charge transportation with reduced bulk recombination whereas pronounced grain boundaries between primary particles (Figure 35c) could act as efficient recombination sites, possibly leading to decreased PEC activity.<sup>177</sup>

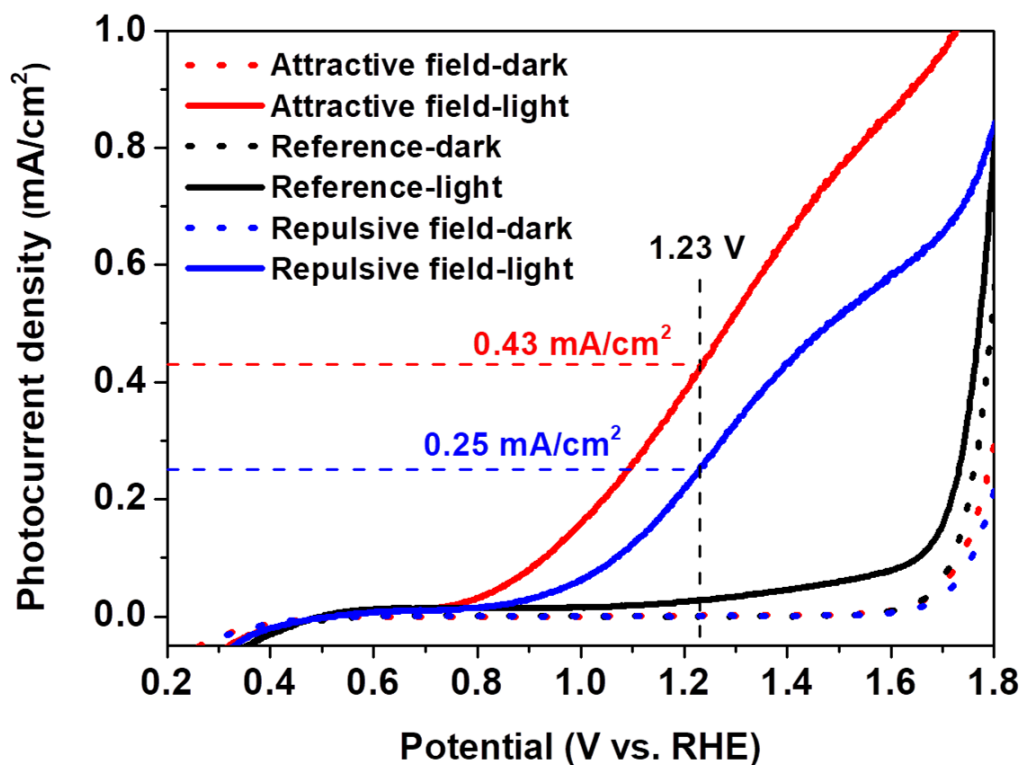
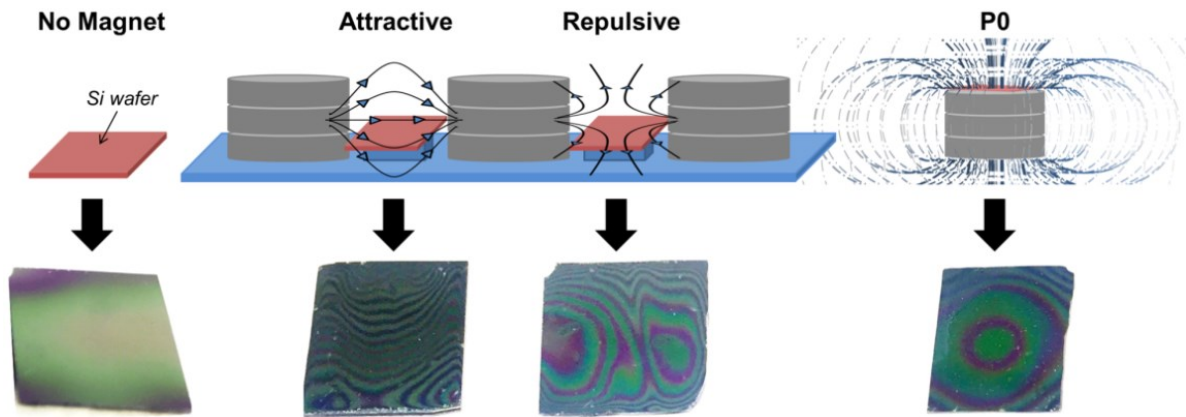


Figure 37 PEC performances of the prepared hematite with the set of the magnet stacks.

#### 4.1.2 Effect of magnetic fields on a non-magnetic oxide ( $\text{SiO}_x$ )

The experimental strategy employing the disk-type magnets was expanded to deposition of silicon oxide ( $\text{SiO}_x$ ). From the earlier observation in the synthesis of hematite, in-situ magnetic fields affected growth and crystallinity of the films as a result of modified plasma environment. And yet it was of further interest to verify the effectiveness of magnets in PECVD process on deposition of  $\text{SiO}_x$  that is non-magnetic. Here, topography of the  $\text{SiO}_x$  prepared under the various magnetic fields was investigated and the films' growth rate was determined by measuring thickness. Eventually, hydrophobicity of the  $\text{SiO}_x$  was compared and evaluated. Figure 38 shows a schematic experimental setup under various conditions with expected magnetic flux lines as well as photographs of actual coatings prepared at each position. When the deposition was carried out without magnets, homogeneous formation of  $\text{SiO}_x$  film was achieved. However, in the processes with magnet stacks involved, characteristic reflection patterns of the coatings were observed, which indicates the deposition of  $\text{SiO}_x$  strongly depended on geometry of the magnetic flux lines. The inhomogeneity of the coatings is regarded as a result of fluctuation on the film thickness.



**Figure 38 (upper row) Illustration of PECVD process under various conditions and (lower row) optical images of the prepared  $\text{SiO}_x$  coatings on silicon wafers.**

To evaluate the deposition kinetics, thickness of the films was measured by SEM (see Figure 39) and the deposition rates were calculated by averaging the thickness values obtained from randomly chosen 6 points in the cross-section images (see Table 11). For deposition time of 10 min, the resultant films' thickness values were varied with respect to the deposition conditions. The average thickness of the reference  $\text{SiO}_x$  film was determined as  $\sim 1.2 \mu\text{m}$  and the coatings prepared with presence of magnet stacks were thicker than the reference sample. The thickest film was produced under the attractive field, showing  $\sim 3.8 \mu\text{m}$  of average thickness and the one positioned where the repulsive field was applied showed  $\sim 2.8 \mu\text{m}$  (Figure 39b and Figure 39c). In addition, growth rates of the magnet-assisted films turned out higher than the reference sample and the plasma confined by the attractive magnetic field resulted in the fastest formation of  $\text{SiO}_x$  film, showing  $384 \pm 17 \text{ nm/min}$  of the growth rate. Moreover, larger standard deviation values calculated for the magnet-assisted films support reflection patterns, whereas the reference sample seemed to be more homogeneously coated (see Figure 38).

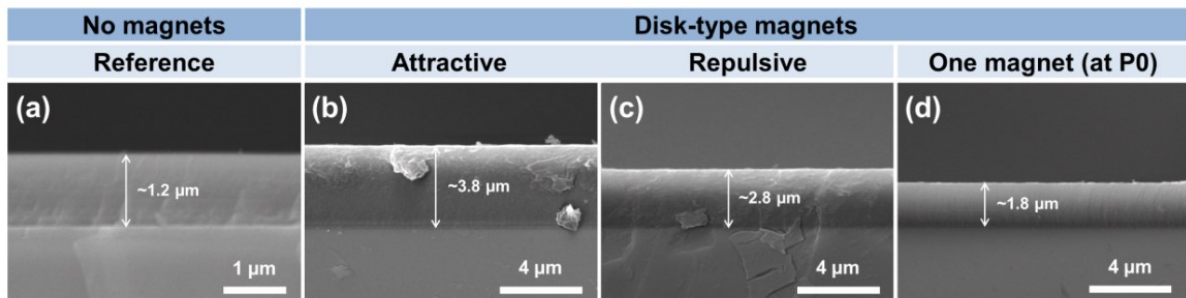


**Figure 39 Cross-section images of the  $\text{SiO}_x$  coatings deposited (a) without magnets, (b) under the attractive field, (c) under the repulsive field, and (d) using one stack of magnets.**



**Table 11** Calculated deposition rates of the SiO<sub>x</sub> coatings under various conditions.

Conditions	No magnets	Disk-type magnets		
Samples	Reference	Attractive	Repulsive	P0
Deposition rate (nm/min)	118 ± 2	384 ± 17	278 ± 37	180 ± 33

Surface topographical images and roughness ( $R_a$  and  $R_q$  for average and root-mean-square roughnesses, respectively) of the SiO<sub>x</sub> films were obtained by AFM to evaluate the deposition tendency, which are given in Figure 40. First, the reference sample exhibited relatively smooth surface, consisting of fine particles, which can be referred to the color index bar. When the SiO<sub>x</sub> was coated under the attractive field, increased roughness was obtained with slightly increased particle size. However, needle-like structure was characterized from the repulsive magnetic field, which is possibly due to the confined plasma by the magnet stack, leading to perpendicular growth of the particles (refer to magnetic field strength and direction in Figure 33). Moreover, when the substrate was put at the position P0 (~13 mT, perpendicular) sparsely distributed particles (>25 nm) were observed on the scanned area. Thus, the reference SiO<sub>x</sub> coating exhibited the lowest roughness value of ~1 nm and the highest roughness values ( $R_a$  = 8.315 nm and  $R_q$  = 12.045 nm) were obtained from the sample prepared on the magnet stack (P0). Hence, it is regarded that the dimension of the plasma confined by magnetic flux has strong influence on the deposition kinetics during PECVD of HMDSO.

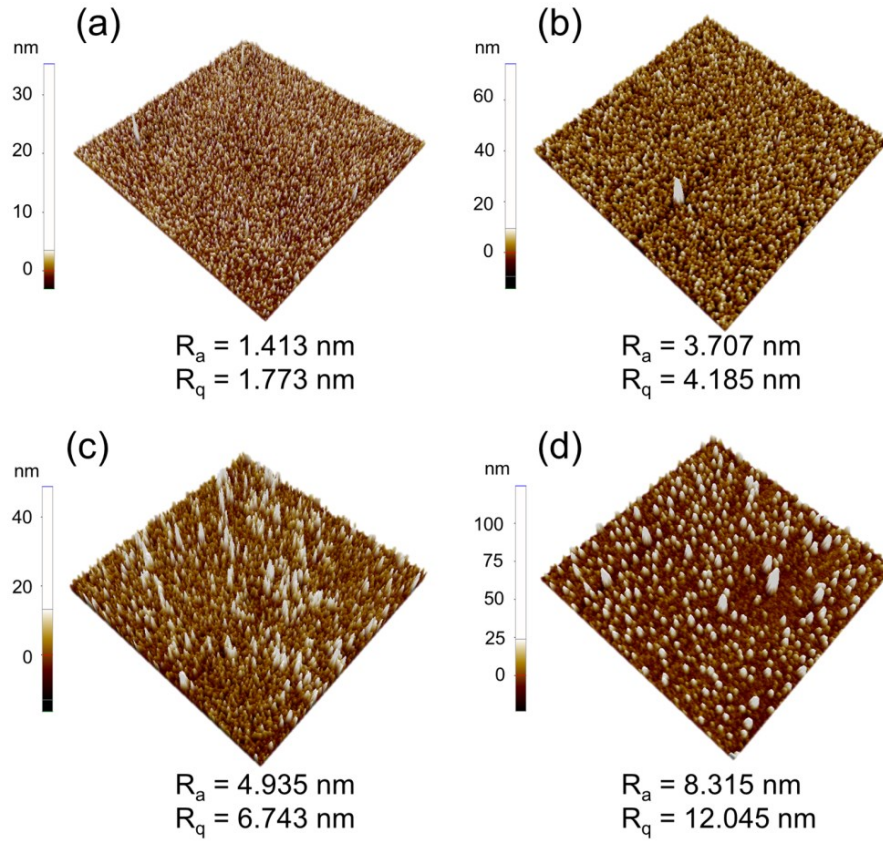


**Figure 40** Surface topographical images and roughness values ( $R_a$  and  $R_q$ ) obtained by AFM; (a) the reference  $\text{SiO}_x$  film,  $\text{SiO}_x$  films deposited (b) under the attractive field, (c) under the repulsive field, and (d) on the magnet stack (P0).

Functionality of the prepared  $\text{SiO}_x$  coatings was further evaluated by measuring static WCAs (water contact angles) that are listed in Table 12. Although silica, in general, performs as hydrophilic agent due to surface silanol groups ( $\text{Si-OH}$ ), the reference  $\text{SiO}_x$  film produced by PECVD exhibited the WCA of  $\sim 91^\circ$  which refers to a typical hydrophobic surface ( $>90^\circ$ ). It is also notable when comparing with a bare silicon wafer that exhibited hydrophilic nature ( $\text{WCA} = \sim 43^\circ$ ). The surface hydrophobicity of  $\text{SiO}_x$  in this case can be attributed to presence of surface hydrocarbons ( $\text{CH}_x$ ) that have low surface energy,<sup>178</sup> which could be inevitably derived from dissociation of the precursor. The chemical states of the films will be discussed in the following part. Furthermore, gradual increase in the WCA was obtained in order of attractive, repulsive and P0. It corresponds well to the surface roughness values that the rougher the microstructure exhibits, the more hydrophobic the surface becomes if the surface is chemically hydrophobic as stated by Wenzel.<sup>115,179</sup> There has been a variety of application areas reported, employing roughness control with hydrophobic coatings.<sup>180–184</sup> Hence, it is promising to achieve superhydrophobicity by controlling surface roughness thanks to intrinsic hydrophobic property of PECVD  $\text{SiO}_x$  film.

**Table 12 Static water contact angles obtained from the various SiO<sub>x</sub> coatings (amount of water droplet, 2  $\mu$ L).**

Conditions	No coating	No magnets	Disk-type magnets		
Samples	Bare Si	Reference	Attractive	Repulsive	P0
Water contact angle ( $^{\circ}$ )	$43.2 \pm 1$	$91.0 \pm 1$	$103.2 \pm 1$	$111.8 \pm 1$	$124.8 \pm 1$

To further corroborate the increased hydrophobicity of the SiO<sub>x</sub> films deposited under the magnetic fields, surface chemical states of the prepared films have been analyzed by quantifying XPS survey spectra (see Table 13). Based on quantification, the as-prepared films obtained from PECVD of HMDOS appear to be more likely SiOC than SiO<sub>x</sub> due to high carbon content exceeding 40 at%. It is probably due to low degree of fragmentation of HMDSO in the process conditions, leaving carbon on the surface.<sup>185</sup> The atomic concentration of Si, C and O as well as the atomic ration of C/O are illustrated in Figure 41. Increased concentration of carbon was obtained from the magnet-assisted samples where the P0 sample appeared to show the highest carbon contents on the surface (55.10 at%). In contrast, oxygen concentration decreased in order of reference, attractive, repulsive, and P0, which led to a tendency that higher C/O ratio was obtained from the magnet-assisted samples than from the reference sample. This surface elemental quantification can be combined with the roughness tendency to validate the wetting behavior of the SiO<sub>x</sub> coatings discussed above.

**Table 13 Elemental quantifications of XPS survey spectra obtained from the prepared SiO<sub>x</sub> films and calculated atomic ratios.**

Samples	Elements (at%)			Atomic ratios		
	Silicon	Carbon	Oxygen	O/Si	C/Si	C/O
Reference	24.68	44.80	30.52	1.24	1.82	1.47
Attractive	23.82	52.11	24.07	1.01	2.19	2.17
Repulsive	28.93	47.15	23.92	0.83	1.63	1.97
P0	23.26	55.10	21.64	0.93	2.37	2.55



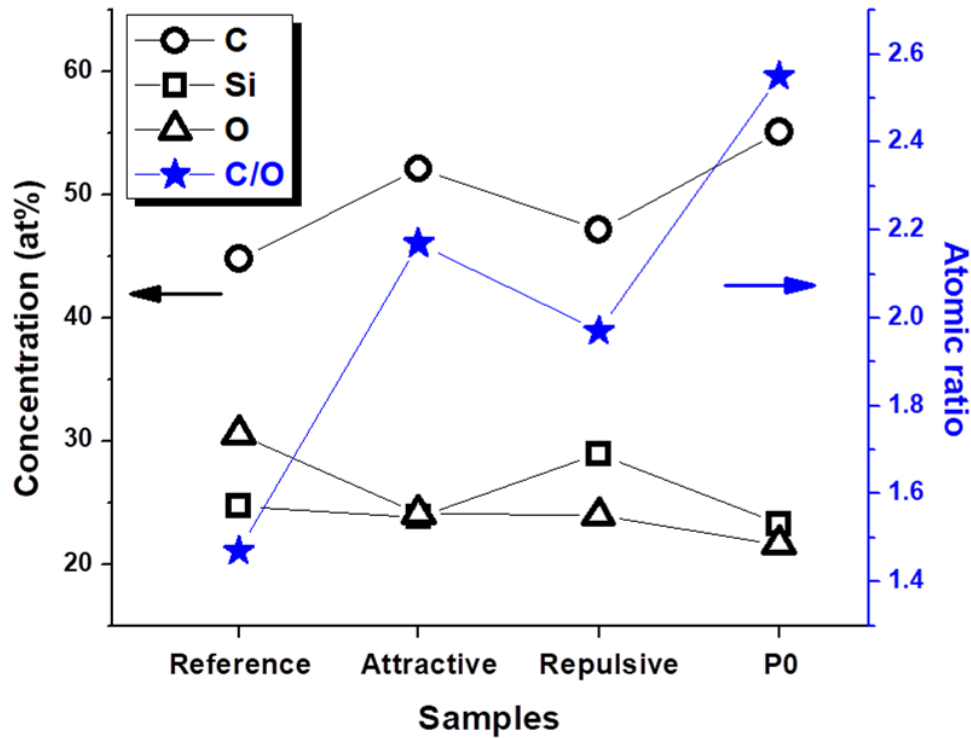


**Figure 41** Graphical illustration of atomic concentration and calculated atomic ratio of C/O.

An identical experiment was conducted on commercial fabric mats to verify feasibility of the PECVD process with magnetic fields. Aqueous solution was prepared by dissolving methylene blue into deionized water for demonstrations of wetting behaviors on various fabric samples (Figure 42). The as-received fabric showed high water absorption, led to complete wetting of the colored solution. However, the one coated with  $\text{SiO}_x$  without any magnetic field exhibited excellent water repellency as well as  $\sim 145^\circ$  of WCA as shown in Figure 42b. This significant enhancement in WCA is attributed to inherent high surface roughness of the fabric, compared to  $\text{SiO}_x$  coating on Si wafer. Furthermore, when the  $\text{SiO}_x$  was coated on the fabric with help of the magnet stack, increased contact angle of  $\sim 160^\circ$  was determined, which indicates that successful and reproducible production of  $\text{SiO}_x$  with better water repellency was achieved. It confirms effectiveness and facileness of employing commercial magnets in PECVD of HMDSO.

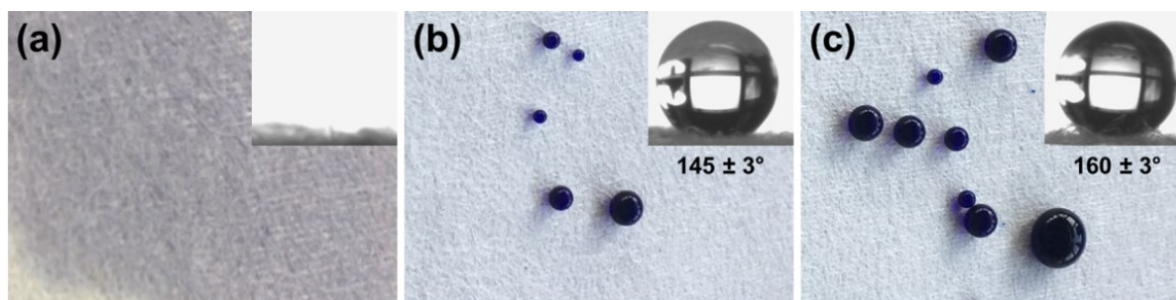


**Figure 42 Demonstration of wetting behavior of the SiO<sub>x</sub> coated fabric mats; (a) as-received fabric, (b) fabric coated with SiO<sub>x</sub> under no magnetic field and (c) fabric coated with SiO<sub>x</sub> under the magnetic field (P0). Insets are images obtained by contact angle measurement.**

## 4.2 Conclusions

Commercial magnets were used in PECVD of iron(0) pentacarbonyl ( $\text{Fe}(\text{CO})_5$ ) and hexamethyldisiloxane (HMDSO,  $\text{O}[\text{Si}(\text{CH}_3)_3]_2$ ). Depending on the type of magnets and the configuration of magnetic flux, not only the physical properties such as morphology, roughness and crystallinity but also the chemical composition of the resultant films varied. Hematite films prepared under magnetic fields that were evolved by rod-type magnets exhibited characteristic surface morphologies, i.e. densely packed particles for the attractive field and faceted nanoparticles with higher porosity for the repulsive field, while the reference hematite film showed randomly shaped particles. Moreover, crystallinity of the hematite film synthesized under the repulsive field for 2 min, displayed higher crystallinity of (110) plane compared to the reference sample. It was also intriguing that complete silent signal of (110) plane was observed for the hematite film deposited under the attractive field for the same deposition duration. These modified properties of the films led to improved PEC performance. As a secondary experimental setup, disk-type magnets were employed to evolve both attractive and repulsive magnetic field simultaneously. Again, there was certain extent of property modifications in morphology, crystallinity and consequently affected photoresponse.

In case of SiO<sub>x</sub> films produced by PECVD of HMDSO, noticeable variation in long-range surface roughness was obtained that the magnetic field seemed to yield rougher surface of SiO<sub>x</sub>. The statistical thickness values enabled us to estimate growth rates of the SiO<sub>x</sub> films during PECVD processes and it appeared that the film grew faster with presence of magnets, however, showing less film homogeneity. From the elemental quantification of the SiO<sub>x</sub> films' surfaces, higher carbon content was detected from the magnets-assisted processes, leading to higher C/O ratio that is strongly related with surface hydrophobicity. Indeed, both on silicon wafer and fabric substrate, superior water repellency was obtained from the films deposited with help of magnets.

## 5 Experimental

### 5.1 Synthesis of heterojunction $\text{Fe}_2\text{O}_3$ - $\text{TiO}_2$ films

#### 5.1.1 Design of heterojunction $\text{Fe}_2\text{O}_3$ - $\text{TiO}_2$ photoelectrodes for PEC water splitting

Prior to plasma enhanced chemical vapor deposition, fluorine-doped tin oxide ( $\text{F}:\text{SnO}_2$ , FTO) coated glass substrates ( $\sim 13 \text{ } \Omega/\text{sq}$ , 3 mm thickness, Sigma Aldrich) were cleaned by ultrasonification with soap water (diluted Hellmanex<sup>TM</sup> III in deionized water) for 10 min to remove organic pollutant on the surface. Then the substrates were rinsed with deionized water to remove remaining surfactants. After rinsing with the deionized water, the substrates were sonicated with acetone and isopropyl alcohol for another 10 min each and were dried up with a heat gun. In between every cleaning step, the substrates were additionally rinsed with the following solvent before ultrasonification to prevent from blending with the former solvent. As a final preparation step of the substrates, Ar plasma treatment was conducted to ensure removal of surface adsorbed molecules, of which process parameters are following; 20 sccm (standard cubic centimeter) of Ar flow rate, 50 W (Watt) of plasma power and 5 min of duration. The base pressure was  $\sim 1.0 \text{ Pa}$  before introduction of Ar. All the FTO substrates were masked with kapton tapes ( $\sim 5 \text{ mm}$  on an edge side) to secure electrical contact area for J-V analyses.

$\text{Fe}_2\text{O}_3$  and  $\text{TiO}_2$  films were prepared by starting with PECVD of  $\text{Fe}(\text{CO})_5$  (Iron(0) pentacarbonyl, 99.50%, Acros Organics<sup>TM</sup>) and  $\text{Ti}[\text{OCH}(\text{CH}_3)_2]_4$  (Titanium(IV) isopropoxide, 98+%, Acros Organics<sup>TM</sup>), respectively. There was no further purification of these precursors before using. These chemicals were fed into the reaction chamber by coupling a single neck round bottomed flask (10 or 15 mL) containing the precursors with a connection pipe equipped with a needle valve.

In the deposition of  $\text{Fe}(\text{CO})_5$ , 20 sccm of oxygen was introduced into the working chamber as oxidizing agent and plasma forming gas at the base pressure of  $\sim 1.0 \text{ Pa}$ . After the chamber pressure became stabilized with constant flow of the oxygen, reaching  $\sim 2.1 \text{ Pa}$ , r.f. power of 100 W was turned on to generate plasma glow in the chamber. Slight fluctuation in the chamber pressure was observed as soon as the plasma starts glowing. This is regarded as a consequence of shift in states of the matter from gas phase to plasma. When the constant pressure was obtained in a few seconds, the precursor was transferred to the PECVD chamber by slowly opening the needle valve. The control of flow rate of the precursor was achieved by monitoring the chamber pressure. The working pressure with the precursor flowing was adjusted to  $\sim 2.5 \text{ Pa}$ . The deposition time for  $\text{Fe}(\text{CO})_5$  was maintained as 5 min to synthesize  $\text{Fe}_2\text{O}_3$  films in this study,

which has been optimized by our group.<sup>104,105</sup> As-deposited films were heat treated to obtain crystalline phase of hematite ( $\alpha$ -Fe<sub>2</sub>O<sub>3</sub>). The annealing was carried out with a tube furnace (RE50-250/13, GERO) of which parameters were set as 10 °C/min of heating rate, 750 °C of annealing temperature and 120 min of dwell time.

For the preparation of TiO<sub>2</sub> films, 20 sccm of oxygen with the r.f. power of 100 W was introduced into the chamber and the rest of the set up procedure was identical to the case of Fe(CO)<sub>5</sub>. However, additional heating was necessary for Ti[OCH(CH<sub>3</sub>)<sub>2</sub>]<sub>4</sub> due to comparably low vapor pressure even under vacuum. A heating tape was wrapped from the precursor flask to the connection pipe for favorable transfer of the precursor and the temperature was maintained at ~70 °C. On the other hand, deposition time was varied to imply the effect of the thickness of intercalated TiO<sub>2</sub> layer on charge carrier behavior as reported (refer to Figure 6). As-deposited films were annealed at 550 °C for 5 h with 10 °C/min of heating rate.

Sequential depositions of Fe(CO)<sub>5</sub> and Ti[OCH(CH<sub>3</sub>)<sub>2</sub>]<sub>4</sub> to synthesize multilayers of TiO<sub>2</sub>//Fe<sub>2</sub>O<sub>3</sub>:FTO and Fe<sub>2</sub>O<sub>3</sub>//TiO<sub>2</sub>//Fe<sub>2</sub>O<sub>3</sub>:FTO were carried out. The annealing step with the parameters described above was involved for every single deposition, i.e. 2 and 3 times of annealing for the double- and triple-layered structures.

For fabrication of the patterned structure, a metallic mask (25 mm x 25 mm) with 6 striped holes (17 mm x 2 mm, spacing 1 mm) was employed. For the second layer of TiO<sub>2</sub>, the mask was placed on the primary hematite film and the PECVD of titanium(IV) isopropoxide was conducted. After annealing it at 550 °C for 5 h, the mask was again put 90° rotated to realize a cross line structure. And then, the PECVD of iron(0) pentacarbonyl was carried out, followed by annealing.

### 5.1.2 Core-shell structured heterojunction of Fe<sub>2</sub>O<sub>3</sub>-TiO<sub>2</sub> photoelectrodes

$\beta$ -FeOOH nanorod arrays were synthesized by a hydrothermal method reported elsewhere with a marginal modification.<sup>106,186</sup> First, under continuous stirring, 0.73 g of ferric chloride (FeCl<sub>3</sub>) and 2.55 g of sodium nitrate (NaNO<sub>3</sub>) were dissolved into 30 mL of deionized water. After obtaining homogeneous solution, it was adjusted to pH 1.5 using hydrochloric acid (HCl). The solution was then poured into an autoclave and a cleaned FTO substrate was also placed into the chamber. The autoclave was maintained at 120 °C for 24 h. The obtained film was rinsed with deionized water and ethanol several times to remove residue. Hematite nanorod arrays were obtained by annealing the as-prepared  $\beta$ -FeOOH film at 750 °C for 2 h (heating rate, 10 °C/min) and utilized as a reference sample in determining PEC performance.

To construct core-shell structure of  $\text{Fe}_2\text{O}_3\text{-TiO}_2$  photoelectrodes, PECVD of titanium(IV) isopropoxide on  $\beta\text{-FeOOH}$  nanorod arrays was performed with varied deposition time. One step annealing to crystallize both  $\beta\text{-FeOOH}$  nanorods and amorphous titanium oxide film was carried out at 750 °C for 2 h with 10 °C/min of heating rate. The deposition time for  $\text{TiO}_2$  using PECVD was varied to control the thickness and morphology. Pristine  $\text{TiO}_2$  film was grown via PECVD without  $\beta\text{-FeOOH}$  nanorods as a reference sample.

## **5.2 Surface modification of hematite films by post-treatment**

### **5.2.1 Post-treatments of hematite films via oxygen/argon plasma and short annealing**

Hematite films were prepared by PECVD followed by the thermal treatment as described above. After obtaining hematite films, additional oxygen or argon plasma process was applied. For the plasma treatment, the PECVD equipment that had been used for the deposition of  $\text{Fe}(\text{CO})_5$  was utilized. An identical flow rate and plasma power of 20 sccm and 100 W, respectively, was used both for oxygen and argon cases. The duration of plasma treatment on crystalline hematite films varied as 10, 20, and 30 min to elucidate morphology change and photocurrent density behavior. During the plasma treatment, the secured area on FTO substrates with kapton tapes was again masked to retain electrical property of the substrate. The short annealing step consisted of preheating of the tube furnace to 750 °C, loading of the samples that had been treated with and/or without plasma for 10 min and quenching of the samples at room temperature.

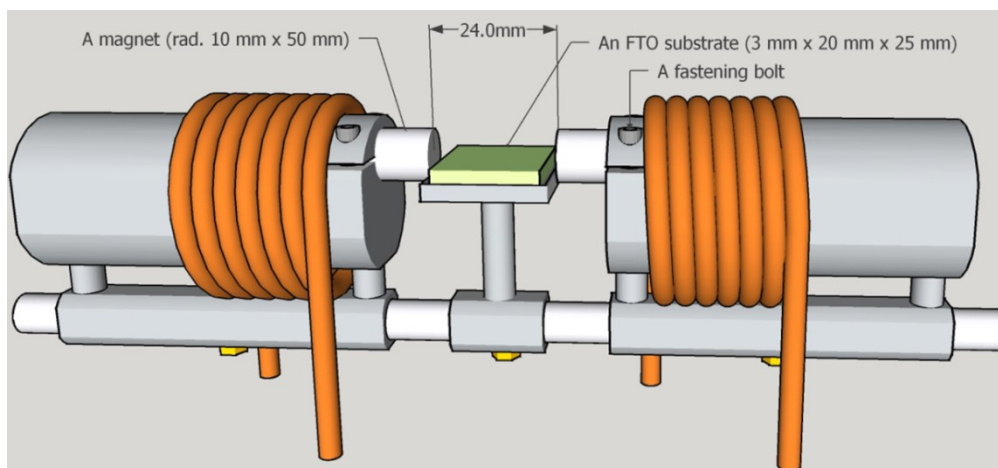
## **5.3 In-situ modification of metal oxides via magnetic field assisted PECVD**

### **5.3.1 Effect of magnetic fields on hematite photoelectrodes for PEC water splitting**

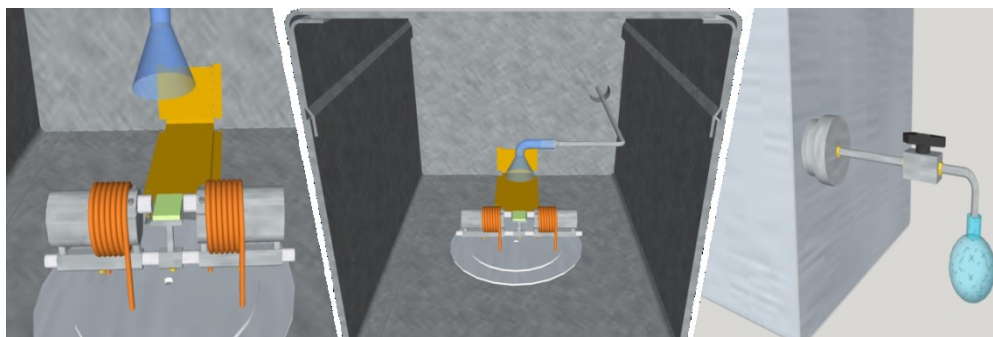
Both rod-type ( $\varnothing$  10 x 50 mm, N45, nickel plated) and disk-type ( $\varnothing$  30 x 6 mm, Y30) magnets were purchased from the MagnetMax (55444 Waldlaubersheim, Germany). To prevent undesired incorporation of magnets during the plasma processes, magnets were covered by kapton tapes.

Firstly, the rod-type magnets were equipped with a home-made apparatus which enables to secure the positions of the magnets and the FTO substrate (Scheme 12) and the actual feature of the PECVD chamber is depicted in Scheme 13. The distance between the magnet tips was fixed to 24 mm, where the magnetic forces existed, i.e. two magnets attracted and repelled each other spontaneously. For the deposition of a reference sample, the apparatus without the magnets was still used. However, there was a limitation by employing the sophisticated structure that the plasma became unstable due to high reflection. This reflection is ascribed to interference of the electric field, caused by the apparatus and yet inhomogeneous distribution of plasma glow.

Consequently, low plasma power of 20 W (r.f. bias  $\sim 25$  V) was applied to guarantee stability of the processes and the longest deposition time was set to 5 min. So it was important to choose a proper geometry of the supports to find out the optimum process parameters in PECVD. Indeed, it was observed that there was a variation up to  $\sim 150$  V difference in working bias voltage by simply altering the geometry of the magnet supports.



**Scheme 12** An illustration of the setup that utilized to apply magnetic fields in PECVD process. Rod-type magnets were used.



**Scheme 13** An experimental setup designed to utilize the rod-type magnets in PECVD; (left and right) enlarged graphics that depict the chamber electrode with the magnet support and the outer apparatus for feeding the precursor, respectively, and (middle) a feature of the reaction chamber.

A set of supplementary experiment was carried out to reveal tendency of bias voltage depending on the magnetic fields since the r.f. bias is one of the major factors to determine kinetics of film formation.<sup>37,187</sup>

A stack of magnets that consists of 3 disk-type magnets was prepared and covered with kapton tapes. Additionally, cylindrical-shaped blocks ( $\varnothing 30 \times 18$  mm each) made of aluminum and PVP

(polyvinylpyrrolidone) were fabricated as replicas of the magnet stack. The chamber pressure and the r.f. bias were recorded and are listed in Table 14. In the absence of blocks (of any types), the r.f. bias was in the range of 400~420 V throughout the process when the r.f. power was set to 25 W. Despite the slight increase in the voltage, 410~440 V of the r.f. bias was detected with the presence of Al or PVP block. This is a significant difference when comparing to the case of existence of the magnet stack where ~200 V of the r.f. bias was detected. Further attenuation of voltage applied was observed with the addition of the magnet stack, which exhibited ~170 V. It indicates that: 1) the magnets in the PECVD influence not only on the dimension of plasma but also on the r.f. bias that affects the films growth and 2) higher extent of plasma confinement, realized by increasing the number of the magnet stack decreased the r.f. bias voltage.

**Table 14 Working parameters of the chamber pressure (Pa) and the r.f. bias (V) in PECVD of Fe(CO)<sub>5</sub> under various conditions.**

Conditions	Working parameters	Vacuum	Feeding oxygen (20 sccm)	Starting plasma (25 W)	Feeding Fe(CO) <sub>5</sub> (0 min)	→			Process ending (15 min)
No magnets	Pressure (Pa)	1.17	2.22	2.23	2.57	2.46	2.42	2.40	
	Voltage (V)	-	-	403	421	399	409	413	
Al block	Pressure (Pa)	1.10	2.18	2.14	2.45			2.24	
	Voltage (V)	-	-	434	414			424	
PVP block	Pressure (Pa)	1.19	2.22	2.22	2.50	2.38	2.30	2.27	
	Voltage (V)	-	-	442	430	435	439	439	
One magnet stack	Pressure (Pa)	1.18	2.21	2.20	2.41	2.30	2.45	2.44	
	Voltage (V)	-	-	205	207	210	208	210	
Three magnet stacks	Pressure (Pa)	1.07	2.11	2.10	2.33	2.40		2.33	
	Voltage (V)	-	-	171	170	165		171	

Employing the disk-type magnets, a set of the second experiment was conducted. A single stack of magnets was put into the working chamber and the substrates (FTO or Si wafer) were placed either onto or beside the stack (refer to Figure 24). The deposition parameters were as following; 20 sccm of oxygen was fed into the chamber upon a specific base pressure and 25 W of plasma power was applied. Then, the needle valve that controls flow of the precursor was slowly opened till the chamber pressure reaches 0.2~0.3 Pa higher than the pressure set in the previous stage. The deposition time was set to 15 min. Furthermore, Instead of using the support for the rod-type magnets that enabled a single substrate per process, *in-situ* deposition of Fe(CO)<sub>5</sub> under different magnetic flux configuration could be achieved. Prior to elaborate the system Three magnet stacks were fixed on a piece of glass with distance of 24 mm between them and the substrates (FTO or Si wafer) were placed in between the stacks (refer to Scheme 11b).

### 5.3.2 Effect of magnetic fields on surface functionality of SiO<sub>x</sub> films

Hexamethyldisiloxane (HMDSO,  $\geq 98\%$ , Sigma Aldrich) was transferred to a reservoir that was connected to the PECVD and used as Si source without further purification. Additional oxygen was fed into the chamber simultaneously to form silicon oxide and the feeding ratio of HMDSO/O<sub>2</sub> was 10/1. To investigate the effect of the magnetic fields on formation of SiO<sub>x</sub> films, the disk-type magnets were employed as described above. Both one stack of magnets and the apparatus with three stacks were tested.

## 5.4 Characterization methods

**X-ray diffraction (XRD):** XRD measurements were performed on a STOE-STADI P using Cu K $\alpha$  ( $\lambda = 1.54 \text{ \AA}$ ) or Mo K $\alpha$  ( $\lambda = 0.71 \text{ \AA}$ ). The graphical analysis was performed using STOE WinXPOW and the graphical illustration using OriginPro 8.

**Scanning electron microscopy (SEM) and energy dispersive X-ray spectroscopy (EDS):** SEM pictures of section 2.1.1 were recorded on a Lyra 3-FEG by TESCAN, while the surface and cross sectional images in section 3.1.1, 4.1.1 and 4.1.2 were obtained by SEM (Zeiss Neon 40 CrossBeam), with the exception of Figure 30 (obtained from Zeiss EVO® LS-10). The elemental analysis of the films was determined using Lyra 3-GMU, TESCAN.

**Atomic force microscopy (AFM):** AFM topography measurements were performed using a Park Systems XE-100 in true non-contact mode with a cantilever (PPP-NCHR-20, Nanosensors).

**X-ray photoelectron spectroscopy (XPS):** X-ray photoelectron spectroscopy (XPS) measurements were carried out using an ESCA M-Probe spectrometer (Surface Science Instruments, SSI) under Al-K $\alpha$  excitation (1486.6 eV) at a pressure of  $10^{-9}$  mbar. Correction to the binding energies was done in reference to the C 1s-signal (284.8 eV). Spectral corrections and composition calculations were performed using CasaXPS.

**Transient absorption spectroscopy (TAS):** The kinetics of the charge carriers was evaluated by flash-photolysis transient absorption spectroscopy (TAS) in a PEC cell in 0.1 M NaOH aqueous solution at the Tampere University of Technology (in section 3.1.1). A Nd:YAG laser (LF117, Solar TII, 10 ns pulse width, 0.33 Hz



repetition rate) was used to generate third harmonic (F015, Solar TII) 355 nm wavelength pulses used as excitation source (attenuated to  $0.54 \text{ mJ/cm}^2$ ). A stabilized halogen lamp (SLS201/M, Thorlabs, 9 W) was used to provide the white light probe beam. The monochromatic (CM110, Digikröm, Spectral Products) transient signal was detected with a silicon photoreceiver (2051-FS, New Focus) and recorded on a digitizing oscilloscope (TDS5032B, 350 MHz, Tektronix). The transient absorption decays were averaged over 300 laser shots at 575 and 650 nm probe wavelengths, using 50,000 points per decay and 40  $\mu\text{s}$  per point for a total of 2 s decay length. A 100 kHz high-frequency filter was used in the photoreceiver amplifier, joined with a 35  $\mu\text{s}$  RC-filter that was connected to the oscilloscope to reduce high-frequency noise in the decays. The decays were averaged with a running 10-base logarithmic average to smooth the longer timescale decays.

**Photoelectrochemical (PEC) analysis:** Electrochemical measurements were performed in a flat three-electrode electrochemical cell using a saturated calomel electrode (SCE) as the reference, a Pt wire as the counter electrode and 1 M NaOH as the electrolyte (pH = 13.6). **(I-V) curves:** Linear sweep voltammetry (10 mV/s) was carried out in a potential range from -1 to 1 V vs. SCE using a potentiostat (PAR, Versa state IV) in the dark and under simulated solar illumination (Xe lamp, 150 W, Oriel with a Schott KG-3 filter). Potentials with respect to the reversible hydrogen electrode (RHE) scale were calculated using the Nernst equation.

To evaluate the prepared samples in photoelectrochemical water splitting performance, current-voltage (I-V) curves were obtained both under illumination and under darkness, which was employed to overall sections. The current values were transformed into current density values by applying an illuminated area of  $\sim 0.64 \text{ cm}^2$ . Three-electrode system consisting of a working electrode (WE, PECVD hematite films), a reference electrode (RE, saturated calomel electrode) and a counter electrode (CE, Pt coil) were connected to a potentiostat (Versastat 4, AMETEK). A simulated light source (a Xenon lamp, 150 W, Oriel) equivalent to 1 SUN was calibrated by a silicon photodetector. Voltage scan rate was fixed as 10 mV/s and  $V_{\text{onset}}$  was determined by reading the voltage where the current density reached  $20 \mu\text{A/cm}^2$ .

**Water contact angle (WCA) measurement:** For determination hydrophobicity of  $\text{SiO}_x$  films, water contact angle was measured by a drop shape analyzer (DSA 100, KRÜSS). Static water contact angle was measured by approaching the coated surface to the water droplet (2  $\mu\text{L}$ ) and the average values

were obtained by measuring 5 points.

## 6 Summary and outlook

Taking strong advantages of PECVD that involve high deposition rate, wide range of usable precursors and reasonable process controllability so on, several projects have been conveyed in this thesis. Especially,  $\text{Fe}_2\text{O}_3$ ,  $\text{TiO}_2$  and  $\text{SiO}_x$  were chosen as target materials due to their unique properties, applicable for PEC water splitting and achieving hydrophobic surfaces, respectively.

Overall, three strategies utilizing PECVD were performed to verify effectiveness on enhanced PEC water splitting performances. In Chapter 2, formation of heterojunctions with patterned structure and construction of core-shell structured 1D heterojunctions were tested. It was to cope with charge separation issue in semiconductors through letting photocarriers be driven to opposite directions for efficient redox reactions. As a result, planar heterojunction photoanodes with macro-scaled patterns led to higher photocurrent density than those without patterns. Regarding 1D core-shell structured photoanodes consisting of  $\text{Fe}_2\text{O}_3$ - $\text{TiO}_2$ , there were optimum process parameters for determining thickness of PECVD  $\text{TiO}_2$  on hematite nanorods for efficient photoelectrochemical reactions. Next, Chapter 3 dealt with surface modification of hematite photoanodes for PEC water splitting, originally motivated by a failure of forming  $\text{Fe}_2\text{O}_3$ - $\text{SnO}_2$  heterojunction as mentioned in the Experimental Chapter. It turned out additional oxygen plasma on crystalline hematite films and sequential short annealing step altered not only morphology but surface states that led to noticeable shift in PEC activity, specifically oxygen evolution rate that was evidenced by TAS. By examining argon plasma as comparison, it was concluded that surface treatment by PECVD was effective as a modification route. Lastly, a facile approach employing magnets in PECVD was introduced in Chapter 4. Starting from evaluation of magnetic field strength and flux geometry, deposition behaviors of  $\text{Fe}_2\text{O}_3$  and  $\text{SiO}_x$  were observed and their independent performances were verified. This work revealed that plasma confined by magnets influenced on morphology and crystallinity of hematite films, consequently improved PEC performance. Moreover,  $\text{SiO}_x$  deposited with help of magnets exhibited rougher surface than the control sample and its growth rate was increased. Higher amount of carbon on surface of magnets-assisted PECVD  $\text{SiO}_x$  which was quantified by XPS might be another factor that led to superior hydrophobicity along with roughened surface.

To sum up, fabrication and modification of metal oxides using PECVD have been studied and the modification strategy stepped down complexity of the process from multiple processes to single (in-situ) step. An overall road map of the works is presented in .

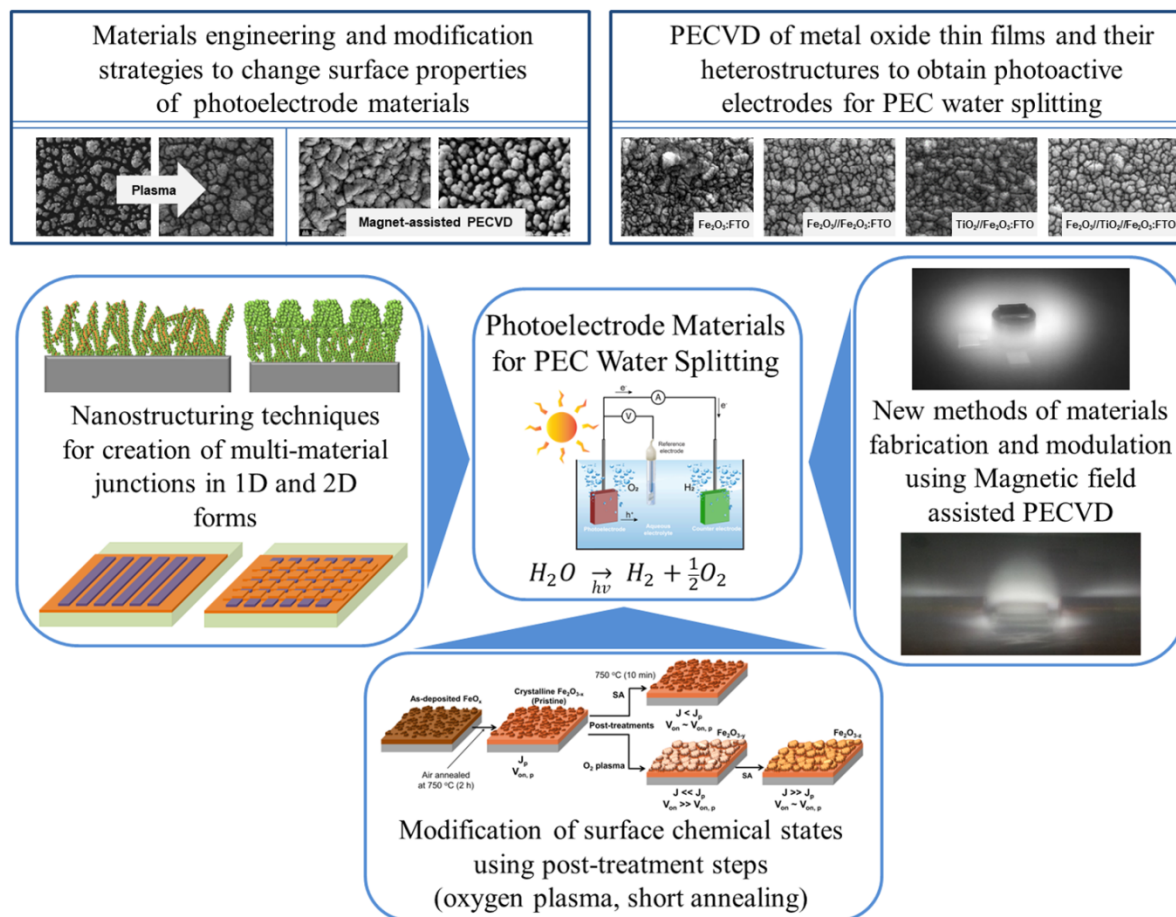


**Figure 43 Summary of the works for producing photoelectrode materials for PEC water splitting.**

Now it is essential not only to remind the overall works but to seek for betterment of the scheme, including missing pieces in each work.

In general, it would be more in control of carrying the precursors if the PECVD setup utilized throughout this work had mass flow controller, since the control of precursor feeding relied only on monitoring interior pressure. We believe that the minor discrepancy in properties of samples produced under the same PECVD parameters could be handled, which will enable us to have more reproducibility in depositions. In terms of the works displayed in this thesis, effects of heterostructuring theme could have been more systematic and informative if masks with various geometries were used. It could have given insight to relate geometric effect of the patterns with PEC activity. Moreover, it is necessary to find a way to equip the mask properly on the substrate. By doing that, we can rule out the possibility of smearing of active species during PECVD, which will enable us to conclude the existence of counter atoms was not from the deposition but from the thermally driven diffusion. In analyses aspect, author regrets that morphology the heterostructure in cross-sectional view was not obtained. This was due to lack of skills to prepare

clean sample. Moving to post-deposition treatment with plasma and short annealing, verification of charge carrier dynamics using TAS is missing in case of Ar plasma treated photoanode. Even if we could speculate that oxygen involved surface states played a crucial role in PEC performance by showing high resolution Fe 2p spectra of Ar plasma treated hematite, it would strengthen the argument by evaluating oxygen evolution rate by TAS. In addition, plasma with e.g. N<sub>2</sub>, H<sub>2</sub> might have been other options to test. Despite mind blowing idea casting magnets in PECVD, there are some missing pieces. First of all, we should have tried to run PECVD with the bias voltage regulation mode that the bias voltage is fixed since the bias voltage applied in the chamber changed depending on apparatus placed in the working chamber as seen in Table 14 that mainly influences on growth of films. This would help compare cases between with and without magnets at fixed bias voltage. For SiO<sub>x</sub> films, evaluation of the coatings is insufficient that only XPS quantification to reveal elemental composition is presented.

Based on this awareness, a project has been planned and is ongoing in PEC water splitting. Currently, a large-scaled PEC cell to demonstrate evolution of oxygen and hydrogen is designed. The cell design is inspired by the PEC cell used in this work and is modified to equip parts, consisting of electrolyte circulation line, gas outputs and a bipolar membrane to separate anode and cathode baths. Author currently studies on controlling microprocessors to evaluate gas evolution and the system for remote monitoring.



## 7 References

1. Ball, M. (Ed.) The Hydrogen Economy. *Cambridge Core* (2009).
2. Miller, E. L. Solar Hydrogen Production by Photoelectrochemical Water Splitting: The Promise and Challenge. in *On Solar Hydrogen & Nanotechnology*, Wiley-Blackwell, 1–35 (2010).
3. Liu, C.-F., Lu, Y.-J. and Hu, C.-C. Effects of Anions and pH on the Stability of ZnO Nanorods for Photoelectrochemical Water Splitting. *ACS Omega* **3**, 3429–3439 (2018).
4. Hamedani, Y., Macha, P., Bunning, T. J., Naik, R. R., Vasudev, R. R. N., and M. C. Plasma-Enhanced Chemical Vapor Deposition: Where we are and the Outlook for the Future. *Chemical Vapor Deposition - Recent Advances and Applications in Optical, Solar Cells and Solid State Devices* 247–280 (2016).
5. Shandilya, M., Rai, R. and Singh, J. Review: hydrothermal technology for smart materials. *Advances in Applied Ceramics* **115**, 354–376 (2016).
6. Auciello, O. and Kingon, A. I. A critical review of physical vapor deposition techniques for the synthesis of ferroelectric thin films. in *Proceedings of the Eighth IEEE International Symposium on Applications of Ferroelectrics, 1992. ISAF '92* 320–331 (1992).
7. Prabu, R., Ramesh, S., Savitha, M., and Balachandra, M. Review of physical vapour deposition (PVD) techniques. in *Proceedings of the International Conference on 'Sustainable Manufacturing'* 427–434 (2013).
8. Pedersen, H. and Elliott, S. D. Studying chemical vapor deposition processes with theoretical chemistry. *Theoretical Chemistry Accounts* **133**, 1476 (2014).
9. Jones, A. C. and Hitchman, M. L. (Eds.) Chapter 1: Overview of Chemical Vapour Deposition. in *Chemical Vapour Deposition*, Royal Society of Chemistry, 1–36 (2009).
10. Greve, D. W., Misra, R., Strong, R., and Schlesinger, T. E. Ultrahigh vacuum/chemical vapor deposition epitaxy of silicon and germanium–silicon heterostructures. *Journal of Vacuum Science & Technology A* **12**, 979–985 (1994).
11. Luo, G. Zhu, P., Chen, P., Liu, Z., Lin, H., and Qian, P. An ultrahigh vacuum chemical vapor deposition system and its application to growth of nMOSFET and HBT structures. *Vacuum* **59**, 927–931 (2000).
12. Sheng, S. R., Dion, M., McAlister, S. P., and Rowell, N. L. Growth and characterization of ultrahigh vacuum/chemical vapor deposition SiGe epitaxial layers on bulk single-crystal SiGe and Si substrates. *Journal of Vacuum Science & Technology A* **20**, 1120–1124 (2002).
13. Sherman, A. Plasma-assisted chemical vapor deposition processes and their semiconductor applications. *Thin Solid Films* **113**, 135–149 (1984).
14. Salvadori, M. C., Mammana, V. P., Martins, O. G., and Degasper, F. T. Plasma-assisted chemical vapour deposition in a tunable microwave cavity. *Plasma Sources Science and Technology* **4**, 489–494 (1995).
15. Langmuir, I. Oscillations in Ionized Gases. *PNAS* **14**, 627–637 (1928).
16. Crookes, W. *On radiant matter: a lecture delivered to the British Association for the Advancement of Science.* (1879).
17. THE TRUE CATHODE RAYS – an article in *The New York Times* (1896).
18. Elementary Plasma-Chemical Reactions. in *Plasma Chemistry* (Ed. Fridman, A.), Cambridge University Press, 12–91 (2008).

19. Martinu, L., Zabeida, O. and Klemberg-Sapieha, J. E. Chapter 9 - Plasma-Enhanced Chemical Vapor Deposition of Functional Coatings. in *Handbook of Deposition Technologies for Films and Coatings (Third Edition)* (Ed. Martin, P. M.), William Andrew Publishing, 392–465 (2010).
20. Tomie, T. Tin laser-produced plasma as the light source for extreme ultraviolet lithography high-volume manufacturing: history, ideal plasma, present status, and prospects. *Journal of Micro/Nanolithography, MEMS, and MOEMS* **11**, 021109 (2012).
21. Feng, J., Nasiatka, J., Wong, J., Chen, X., Hidalgo, S., Vecchione, T., Zhu, H., Javier Palomares F., and Padmore H. A. A stigmatic ultraviolet-visible monochromator for use with a high brightness laser driven plasma light source. *Review of Scientific Instruments* **84**, 085114 (2013).
22. Prakash, R., Hossain, A. F., Pal, U. N., Kumar, N., Khiarnar, K., and Mohan, M. K. Dielectric Barrier Discharge based Mercury-free plasma UV-lamp for efficient water disinfection. *Scientific Reports* **7**, 17426 (2017).
23. Foster, J. E. Plasma-based water purification: Challenges and prospects for the future. *Physics of Plasmas* **24**, 055501 (2017).
24. Jones, B. J. and Nelson, N. Sticking non-stick: Surface and Structure control of Diamond-like Carbon in Plasma Enhanced Chemical Vapour Deposition. *Journal of Physics: Conference Series* **768**, 012011 (2016).
25. Varade, A., Krishna, A., Reddy, K. N., Chellamalai, M., and Shashikumar, P. V. Diamond-like Carbon Coating Made by RF Plasma Enhanced Chemical Vapour Deposition for Protective Antireflective Coatings on Germanium. *Procedia Materials Science* **5**, 1015–1019 (2014).
26. Roy, R. K. and Lee, K.-R. Biomedical applications of diamond-like carbon coatings: A review. *Journal of Biomedical Materials Research Part B: Applied Biomaterials* **83B**, 72–84
27. Liskiewicz, T. and Al-Borno, A. DLC Coatings in Oil and Gas Production. *Journal of Coating Science and Technology* **1**, 59–68 (2015).
28. Varade, A., Reddy, K. R., Sasen, D., Krishna, A., Chellamalai, M., and Shashikumar, P. V. Detailed Raman Study of DLC Coating on Si (100) Made by RF-PECVD. *Procedia Engineering* **97**, 1452–1456 (2014).
29. Ward, L., Junge, F., Lampka, A., Dobbertin, M., Mewes, C., and Wienecke, M. The Effect of Bias Voltage and Gas Pressure on the Structure, Adhesion and Wear Behavior of Diamond Like Carbon (DLC) Coatings With Si Interlayers. *Coatings* **4**, 214–230 (2014).
30. Holland, L. and Ojha, S. M. Deposition of hard and insulating carbonaceous films on an r.f. target in a butane plasma. *Thin Solid Films* **38**, L17–L19 (1976).
31. Amaratunga, G., Putnis, A., Clay, K., and Milne, W. Crystalline diamond growth in thin films deposited from a CH<sub>4</sub>/Ar rf plasma. *Applied Physics Letters* **55**, 634–635 (1989).
32. Spencer, E. G., Schmidt, P. H., Joy, D. C., and Sansalone, F. J. Ion-beam-deposited polycrystalline diamondlike films. *Applied Physics Letters* **29**, 118–120 (1976).
33. Miyake, S., Saito, T., Yasuda, Y., Okamoto, Y., and Kano, M. Improvement of boundary lubrication properties of diamond-like carbon (DLC) films due to metal addition. *Tribology International* **37**, 751–761 (2004).
34. Lee, N. R., Jun, Y. S., Moon, K. I., and Lee, C. S. Ti-doped hydrogenated diamond like carbon coating deposited by hybrid physical vapor deposition and plasma enhanced chemical vapor deposition. *Japanese Journal of Applied Physics* **56**, 035506 (2017).



35. Fu, R. K. Y., Mei, Y. F., Fu, M. Y., Liu, X. Y., and Chu, P. K. Thermal stability of metal-doped diamond-like carbon fabricated by dual plasma deposition. *Diamond and Related Materials* **14**, 1489–1493 (2005).
36. McCauley, T. G., Gruen, D. M. and Krauss, A. R. Temperature dependence of the growth rate for nanocrystalline diamond films deposited from an Ar/CH<sub>4</sub> microwave plasma. *Applied Physics Letters* **73**, 1646–1648 (1998).
37. Amaratunga, G. A. J., Silva, S. R. P. and McKenzie, D. R. Influence of dc bias voltage on the refractive index and stress of carbon-diamond films deposited from a CH<sub>4</sub>/Ar rf plasma. *Journal of Applied Physics* **70**, 5374–5379 (1991).
38. Clay, K. J., Speakman, S. P., Morrison, N. A., Tomozeiu, N., Milne, W. I., and Kapoor, A. Material properties and tribological performance of rf-PECVD deposited DLC coatings. *Diamond and Related Materials* **7**, 1100–1107 (1998).
39. Meyerson, B. and Smith, F. W. Electrical and optical properties of hydrogenated amorphous carbon films. *Journal of Non-Crystalline Solids* **35–36**, 435–440 (1980).
40. Ladwig, A. M., Koch, R. D., Wenski, E. G., and Hicks, R. F. Atmospheric plasma deposition of diamond-like carbon coatings. *Diamond and Related Materials* **18**, 1129–1133 (2009).
41. Marciano, F. R., Bonetti, L. F., Santos, L. V., Da-Silva, N. S., and Trava-Airoldi, V. J. Antibacterial activity of DLC and Ag–DLC films produced by PECVD technique. *Diamond and Related Materials* **18**, 1010–1014 (2009).
42. Caschera, D., Federici, F., Kaciulis, S., Pandolfi, L., Cusmà, A., and Padeletti, G. Deposition of Ti-containing diamond-like carbon (DLC) films by PECVD technique. *Materials Science and Engineering: C* **27**, 1328–1330 (2007).
43. Buršíková, V., Navrátil, V., Zajičková, L., and Janča, J. Temperature dependence of mechanical properties of DLC/Si protective coatings prepared by PECVD. *Materials Science and Engineering: A* **324**, 251–254 (2002).
44. Ahmed, M. H., Byrne, J. A. and McLaughlin, J. Evaluation of glycine adsorption on diamond like carbon (DLC) and fluorinated DLC deposited by plasma-enhanced chemical vapour deposition (PECVD). *Surface and Coatings Technology* **209**, 8–14 (2012).
45. Gordillo-Vázquez, F. J. Special Issue on Low-Pressure Plasma-Enhanced CVD. *Chemical Vapor Deposition* **13**, 265–266 (2007).
46. Poenar, C. I. and D. P. Chapter 5: PECVD Amorphous Silicon Carbide ( $\alpha$ -SiC) Layers for MEMS Applications. in *Physics and Technology of Silicon Carbide Devices* (ed. Hijikata, Y.), InTech, 131–148 (2012).
47. Habuka, H. Chapter 3: Low Temperature Chemical Vapour Deposition of Polycrystalline Silicon Carbide Film Using Monomethylsilane Gas. in *Properties and Applications of Silicon Carbide* (Ed. Gerhardt, R.), InTech, 55–76 (2011).
48. Flannery, A. F., Mourlas, N. J., Storment, C. W., Tsai, S., Tan, S. H., Heck, J., Monk, D., Kim, T., Gogoi, B., and Kovacs, G. T. A. PECVD silicon carbide as a chemically resistant material for micromachined transducers. *Sensors and Actuators A: Physical* **70**, 48–55 (1998).
49. Yamada, K. and Mohri, M. Chapter 2: Properties and Applications of Silicon Carbide Ceramics. in *Silicon Carbide Ceramics-I* (Eds. Sömiya, S. et al.), Elsevier Science Publishers Ltd, 13–44 (1991).
50. Li, J., Tian, J. and Dong, L. Synthesis of SiC precursors by a two-step sol–gel process and their

conversion to SiC powders. *Journal of the European Ceramic Society* **20**, 1853–1857 (2000).

51. Yang, Y., Lin, Z.-M. and Li, J.-T. Synthesis of SiC by silicon and carbon combustion in air. *Journal of the European Ceramic Society* **29**, 175–180 (2009).
52. Liu, J., Qiao, Y., Zhang, P., Xue, Y., and Cai, Z. Synthesis of SiC ceramics from polysilazane by laser pyrolysis. *Surface and Coatings Technology* **321**, 491–495 (2017).
53. Cogan, S. F., Edell, D. J., Guzelian, A. A., Liu, Y. P., and Edell, R. Plasma-enhanced chemical vapor deposited silicon carbide as an implantable dielectric coating. *Journal of Biomedical Materials Research Part A* **67A**, 856–867
54. Gubernat, A., Pichór, W., Lach, R., Zientara, D., Sitarz, M., and Springwald, M. Low-temperature synthesis of silicon carbide powder using shungite. *Boletín de la Sociedad Española de Cerámica y Vidrio* **56**, 39–46 (2017).
55. Keski-Kuha, R. A. M., Osantowski, J. F., Toft, A. R., and Partlow, W. D. Grazing incidence reflectance of SiC films produced by plasma-assisted chemical vapor deposition. *Applied Optics* **27**, 1499–1502 (1988).
56. Derst, G., Kalbitzer, S., Krötz, G., and Müller, G. Preparation of crystalline SiC thin films by plasma-enhanced chemical vapour deposition and by ion beam modification of silicon. *Materials Science and Engineering: B* **11**, 79–82 (1992).
57. Nakano, M., Takano, A., Kawasaki, M., and Koinuma, H. Hydrogenated amorphous silicon/hydrogenated amorphous silicon carbide superlattice prepared continuously by pulsed plasma and photo chemical vapor deposition. *Journal of Applied Physics* **71**, 5257–5259 (1992).
58. Filatova, E. A., Hausmann, D. and Elliott, S. D. Understanding the Mechanism of SiC Plasma-Enhanced Chemical Vapor Deposition (PECVD) and Developing Routes toward SiC Atomic Layer Deposition (ALD) with Density Functional Theory. *ACS Applied Materials & Interfaces* **10**, 15216–15225 (2018).
59. Windischmann, H. Intrinsic stress and mechanical properties of hydrogenated silicon carbide produced by plasma-enhanced chemical vapor deposition. *Journal of Vacuum Science & Technology A* **9**, 2459–2463 (1991).
60. Brassard, D. and El Khakani, M. A. Dielectric properties of amorphous hydrogenated silicon carbide thin films grown by plasma-enhanced chemical vapor deposition. *Journal of Applied Physics* **93**, 4066–4071 (2003).
61. Huran, J. Zaťko, B., Hotový, I., Pezoldt, J., Kobzev, A. P., and Balalykin, N. I. PECVD silicon carbide deposited at different temperature. *Czechoslovak Journal of Physics* **56**, B1207–B1211 (2006).
62. Pandraud, G., French, P. J. and Sarro, P. M. PECVD Silicon Carbide Waveguides for Multichannel Sensors. in *SENSORS, 2007 IEEE* **43**, 395–398 (2007).
63. Chen, E. Du, G., Zhang, Y., Qin, X., Lai, H., and Shi, W. RF-PECVD deposition and optical properties of hydrogenated amorphous silicon carbide thin films. *Ceramics International* **40**, 9791–9797 (2014).
64. Ivashchenko, V. I., Dub, S. N., Porada, O. K., Ivashchenko, L. A., Skrynsky, P. L., and Stegny, A. I. Mechanical properties of PECVD a-SiC:H thin films prepared from methyltrichlorosilane. *Surface and Coatings Technology* **200**, 6533–6537 (2006).
65. Choi, W. K., Lee, L. P., Foo, S. L., Gangadharan, S., Chong, N. B., and Tan, L. S. Oxidation study of plasma-enhanced chemical vapor deposited and rf sputtered hydrogenated amorphous silicon carbide films. *Journal of Applied Physics* **89**, 1942–1947 (2001).

- 
66. Pierson, H. O. (Ed.) Chapter 11: The CVD of Ceramic Materials: Oxides. in *Handbook of Chemical Vapor Deposition (CVD) (Second Edition)*, William Andrew Publishing, 295–322 (1999).
67. Rao, C. N. R. Transition Metal Oxides. *Annual Review of Physical Chemistry* **40**, 291–326 (1989).
68. Bao, X.-M., Cui, J.-F., Sun, H.-X., Liang, W.-D., Zu, Z.-Q., An, J., Yang, B.-P., La, P.-Q., and Li, A. Facile preparation of superhydrophobic surfaces based on metal oxide nanoparticles. *Applied Surface Science* **303**, 473–480 (2014).
69. Kanzler, C. H. Urban, S., Zalewska-Wierzbivka, K., Hess, F., Rohrlack, S. F., Wessel, C., Ostermann, R., Hofmann, J. P., Smarsly, B. M., and Over, H. Electrospun Metal Oxide Nanofibres for the Assessment of Catalyst Morphological Stability under Harsh Reaction Conditions. *ChemCatChem* **5**, 2621–2626 (2013).
70. Bulusu, A., Paniagua, S. A., MacLeod, B. A., Sigdel, A. K., Bery, J. J., Olson, D. C., Marder, S. R., and Graham, S. Efficient Modification of Metal Oxide Surfaces with Phosphonic Acids by Spray Coating. *Langmuir* **29**, 3935–3942 (2013).
71. Dong, Z., Lai, X., Halpert, J. E., Yang, N., Yi, L., Zhai, J., Wang, D., Tang, Z., Jiang, L. Accurate Control of Multishelled ZnO Hollow Microspheres for Dye-Sensitized Solar Cells with High Efficiency. *Advanced Materials* **24**, 1046–1049 (2012).
72. Park, S.-K., Seong, C.-Y. and Piao, Y. A Simple Dip-coating Approach for Preparation of Three-dimensional Multilayered Graphene-Metal Oxides Hybrid Nanostructures as High Performance Lithium-Ion Battery Electrodes. *Electrochimica Acta* **176**, 1182–1190 (2015).
73. Wu, L., Yang, D., Fei, L., Huang, Y., Wu, F., Sun, Y., Shi, J., and Xiang, Y. Dip-Coating Process Engineering and Performance Optimization for Three-State Electrochromic Devices. *Nanoscale Research Letters* **12**, 390 (2017).
74. Sun, H. B., Yang, J., Zhou, Y. Z., Zhao, N., and Li, D. Preparation of reduced graphene oxide films by dip coating technique and their electrical conductivity. *Materials Technology* **29**, 14–20 (2014).
75. Xu, D., Luo, L., Ding, Y., and Xu, P. Sensitive electrochemical detection of glucose based on electrospun  $\text{La}_{0.88}\text{Sr}_{0.12}\text{MnO}_3$  nanofibers modified electrode. *Analytical Biochemistry* **489**, 38–43 (2015).
76. Xu, G., Zhang, S., Zhang, Q., Gong, L., Dai, H., and Lin, Y., Magnetic functionalized electrospun nanofibers for magnetically controlled ultrasensitive label-free electrochemiluminescent immune detection of aflatoxin B1. *Sensors and Actuators B: Chemical* **222**, 707–713 (2016).
77. Olson, D. C., Piris, J., Collins, R. T., Shaheen, S. E., and Ginley, D. S. Hybrid photovoltaic devices of polymer and ZnO nanofiber composites. *Thin Solid Films* **496**, 26–29 (2006).
78. Kuai, L., Wang, J., Ming, T., Fang, C., Sun, Z., Geng, B., and Feng, J. Aerosol-spray diverse mesoporous metal oxides from metal nitrates. *Scientific Reports* **5**, 9923 (2015).
79. Pattanasattayavong, P., Thomas, S., Adamopoulos, G., McLachlan, M. A., and Anthopoulos, T. D. p-channel thin-film transistors based on spray-coated  $\text{Cu}_2\text{O}$  films. *Applied Physics Letters* **102**, 163505 (2013).
80. Yu, X., Smith, J., Zhou, N., Zeng, L., Guo, P., Xia, Y., Alvarez, A., Aghion, S., Lin, H., Yu, J., Chang, R. P. H., Bedzyk, M. J., Ferragut, R., Marks, T. J., and Facchetti, A. Spray-combustion synthesis: Efficient solution route to high-performance oxide transistors. *Proceedings of the National Academy of Sciences* **112**, 3217–3222 (2015).
81. Ito, S., Makari, Y., Kitamura, T., Wada, Y., and Yanagida, S. Fabrication and characterization of mesoporous  $\text{SnO}_2/\text{ZnO}$ -composite electrodes for efficient dye solar cells. *Journal of Materials Chemistry* **14**, 385–390 (2004).

- 
82. Stubhan, T., Krantz, J., Li, N., Guo, F., Litzov, I., Steidl, M., Richter, M., Matt, G. J., and Brabec, C. J. High fill factor polymer solar cells comprising a transparent, low temperature solution processed doped metal oxide/metal nanowire composite electrode. *Solar Energy Materials and Solar Cells* **107**, 248–251 (2012).
83. Wang, H., Wei, W. and Hu, Y. H. Efficient ZnO-based counter electrodes for dye-sensitized solar cells. *Journal of Materials Chemistry A* **1**, 6622–6628 (2013).
84. Kage, H., Abe, R., Hattanda, R., Zhou, T., Ogura, H., and Matsuo, Y., Effect of solid circulation rate on coating efficiency and agglomeration in circulating fluidized bed type coater. *Powder Technology* **130**, 203–210 (2003).
85. Gürsoy, M. and Karaman, M. Hydrophobic coating of expanded perlite particles by plasma polymerization. *Chemical Engineering Journal* **284**, 343–350 (2016).
86. Karaman, M., Gürsoy, M., Kuş, M., Özel, F., Yenel, E., Şahin, Ö, G., and Kivrak, H. D. Chemical and Physical Modification of Surfaces. in *Surface Treatments for Biological, Chemical, and Physical Applications*, Wiley-Blackwell, 23–66 (2016).
87. Ren, Y., Ma, Z. and Bruce, P. G. Ordered mesoporous metal oxides: synthesis and applications. *Chemical Society Reviews* **41**, 4909–4927 (2012).
88. Zhai, T., Fang, X., Liao, M., Xu, X., Zeng, H., Yoshio, B., and Goldberg, D. A Comprehensive Review of One-Dimensional Metal-Oxide Nanostructure Photodetectors. *Sensors* **9**, 6504–6529 (2009).
89. Piyadasa, A., Wang, S. and Gao, P.-X. Band structure engineering strategies of metal oxide semiconductor nanowires and related nanostructures: A review. *Semiconductor Science and Technology* **32**, 073001 (2017).
90. Runnerstrom, E. L., Bergerud, A., Agrawal, A., Johns, R. W., Dahlman, C. J., Singh, A., Selbach, S. M., and Miliron D. J. Defect Engineering in Plasmonic Metal Oxide Nanocrystals. *Nano Letters* **16**, 3390–3398 (2016).
91. Wang, D., Zhang, Y., Peng, C., Wang, J., Huang, Q., Su, S., Wang, L., Huang, W., and Fan, C. Crystallinity Engineering of Hematite Nanorods for High-Efficiency Photoelectrochemical Water Splitting. *Advanced Science* **2**, 1500005 (2015).
92. Statistical Review of World Energy | Energy economics | BP. *bp.com* Available at: <https://www.bp.com/en/global/corporate/energy-economics/statistical-review-of-world-energy.html>.
93. LeRoy, R. L. Industrial water electrolysis: Present and future. *International Journal of Hydrogen Energy* **8**, 401–417 (1983).
94. Dutta, S. Technology assessment of advanced electrolytic hydrogen production. *International Journal of Hydrogen Energy* **15**, 379–386 (1990).
95. Cho, S., Jang, J.-W., Lee, K.-H., and Lee, J. S. Research Update: Strategies for efficient photoelectrochemical water splitting using metal oxide photoanodes. *APL Materials* **2**, 010703 (2014).
96. Yang, Y., Shuwen, N., Han, D., Liu, T., Wang, G., Li, Y. Progress in Developing Metal Oxide Nanomaterials for Photoelectrochemical Water Splitting. *Advanced Energy Materials* **7**, 1700555 (2017).
97. Jafari, T., Moharreri, E., Amin, A. S., Miao, R., Song, W., Suib, S. L. Photocatalytic Water Splitting-The Untamed Dream: A Review of Recent Advances. *Molecules* **21**, 900 (2016).
98. Fujishima, A. and Honda, K. Electrochemical Photolysis of Water at a Semiconductor Electrode. *Nature* **238**, 37–38 (1972).

99. Ahn, K.-S., Shet, S., Deutsch, T., Jiang, C.-S., Yan, Y., Al-Jassim, and Turner, J. Enhancement of photoelectrochemical response by aligned nanorods in ZnO thin films. *Journal of Power Sources* **176**, 387–392 (2008).
100. Khan, S. U. M. and Sultana, T. Photoresponse of n-TiO<sub>2</sub> thin film and nanowire electrodes. *Solar Energy Materials and Solar Cells* **76**, 211–221 (2003).
101. Pan, Z., Qui, Y., Yang, J., Liu, M., Zhou, L., Xu, Y., Sheng, L., Zhao, X., and Zhang, Y. Synthesis of three-dimensional hyperbranched TiO<sub>2</sub> nanowire arrays with significantly enhanced photoelectrochemical hydrogen production. *Journal of Materials Chemistry A* **3**, 4004–4009 (2015).
102. Yan, L., Zhao, W. and Liu, Z. 1D ZnO/BiVO<sub>4</sub> heterojunction photoanodes for efficient photoelectrochemical water splitting. *Dalton Transactions* **45**, 11346–11352 (2016).
103. Grigioni, I., Stampelcoskie, K. G., Jara, D. H., Dozzi, M. V., Oriana, A., Cerullo, G., Kamat, P. V., and Selli, E. Wavelength-Dependent Ultrafast Charge Carrier Separation in the WO<sub>3</sub>/BiVO<sub>4</sub> Coupled System. *ACS Energy Letters* **2**, 1362–1367 (2017).
104. Singh, A. P., Mettenbörger, A., Golus, P., and Mathur, S. Photoelectrochemical properties of hematite films grown by plasma enhanced chemical vapor deposition. *International Journal of Hydrogen Energy* **37**, 13983–13988 (2012).
105. Mettenbörger, A., Singh, T., Sing, A. P., Järvi, T. T., Moseler, M., Valldor, M., and Mathur, S. Plasma-chemical reduction of iron oxide photoanodes for efficient solar hydrogen production. *International Journal of Hydrogen Energy* **39**, 4828–4835 (2014).
106. Wang, M., Pyeon, M., Gönüllü, Y., Kaouk, A., Shen, S., Guo, L., and Mathur, S. Constructing Fe<sub>2</sub>O<sub>3</sub>/TiO<sub>2</sub> core-shell photoelectrodes for efficient photoelectrochemical water splitting. *Nanoscale* **7**, 10094–10100 (2015).
107. Kaouk, A., Ruoko, T.-P., Gönüllü, Y., Mettenbörger, A., Gurevich, E., Lemmetyinen, H., Ostendorf, A., and Mathur, S. Graphene-intercalated Fe<sub>2</sub>O<sub>3</sub>/TiO<sub>2</sub> heterojunctions for efficient photoelectrolysis of water. *RSC Advances* **5**, 101401–101407 (2015).
108. Mettenbörger, A., Gönüllü, Y., Fischer, T., Heisig, T., Sasinska, A., Maccato, C., Carraro, G., Sada, C., Barreca, D., Mayrhofer, L., Moseler, M., Held, A., Mathur, S. Interfacial insight in multi-junction metal oxide photoanodes for water-splitting applications. *Nano Energy* **19**, 415–427 (2016).
109. Kaouk, A., Ruoko, T.-P., Pyeon, M., Gönüllü, Y., Kaunisto, K., Lemmetyinen, H., Mathur, S. High Water-Splitting Efficiency through Intentional In and Sn Codoping in Hematite Photoanodes. *The Journal of Physical Chemistry C* **120**, 28345–28353 (2016).
110. Sivula, K., Zboril, R., Le Formal, F., Robert, R., Weidenkaff, A., Tucek, J., Frydrych, J., and Grätzel, M. Photoelectrochemical Water Splitting with Mesoporous Hematite Prepared by a Solution-Based Colloidal Approach. *Journal of the American Chemical Society* **132**, 7436–7444 (2010).
111. Ling, Y., Wang, G., Wheeler, D. A., Zhang, J. Z., and Li, Y. Sn-Doped Hematite Nanostructures for Photoelectrochemical Water Splitting. *Nano Letters* **11**, 2119–2125 (2011).
112. Simpson, J. T., Hunter, S. R. and Aytug, T. Superhydrophobic materials and coatings: a review. *Reports on Progress in Physics* **78**, 086501 (2015).
113. Young, T. III. An essay on the cohesion of fluids. *Philosophical Transactions of the Royal Society London* **95**, 65–87 (1805).
114. Good, R. J. A Thermodynamic Derivation of Wenzel’s Modification of Young’s Equation for Contact

- Angles; Together with a Theory of Hysteresis<sup>1</sup>. *Journal of the American Chemical Society* **74**, 5041–5042 (1952).
115. Wenzel, R. N. RESISTANCE OF SOLID SURFACES TO WETTING BY WATER. *Industrial & Engineering Chemistry* **28**, 988–994 (1936).
116. Cassie, A. B. D. & Baxter, S. Wettability of porous surfaces. *Transactions of the Faraday Society* **40**, 546–551 (1944).
117. Palumbo, F., Mundo, R. D., Cappelluti, D., and d'Agostino, R. SuperHydrophobic and SuperHydrophilic Polycarbonate by Tailoring Chemistry and Nano-texture with Plasma Processing. *Plasma Processes and Polymers* **8**, 118–126 (2011).
118. Hnilica, J., Schäfer, J., Foest, R., Zajíčková, L. and Kudrle, V. PECVD of nanostructured SiO<sub>2</sub> in a modulated microwave plasma jet at atmospheric pressure. *Journal of Physics D: Applied Physics* **46**, 335202 (2013).
119. Pan, J., Song, X., Zhang, J., Shen, H., and Xiong, Q. Switchable Wettability in SnO<sub>2</sub> Nanowires and SnO<sub>2</sub>@SnO<sub>2</sub> Heterostructures. *The Journal of Physical Chemistry C* **115**, 22225–22231 (2011).
120. Nguyen, T. P. N., Dufour, R., Thomy, V., Senez, V., Boukherroub, R., Coffinier, Y. Fabrication of superhydrophobic and highly oleophobic silicon-based surfaces via electroless etching method. *Applied Surface Science* **295**, 38–43 (2014).
121. Liu, G., Fu, L., Rode, A. V., and Craig, V. S. J. Water Droplet Motion Control on Superhydrophobic Surfaces: Exploiting the Wenzel-to-Cassie Transition. *Langmuir* **27**, 2595–2600 (2011).
122. Fanelli, F., Mastrangelo, A. M. and Fracassi, F. Aerosol-Assisted Atmospheric Cold Plasma Deposition and Characterization of Superhydrophobic Organic–Inorganic Nanocomposite Thin Films. *Langmuir* **30**, 857–865 (2014).
123. Choudhary, S., Upadhyay, S., Kumar, P., Singh, N., Satsangi, V. R., Shrivastav, R., Dass, S. Nanostructured bilayered thin films in photoelectrochemical water splitting – A review. *International Journal of Hydrogen Energy* **37**, 18713–18730 (2012).
124. Grätzel, M. Photoelectrochemical cells. *Nature* **414**, 338–344 (2001).
125. Sivula, K., Le Formal, F. and Grätzel, M. Solar Water Splitting: Progress Using Hematite ( $\alpha$ -Fe<sub>2</sub>O<sub>3</sub>) Photoelectrodes. *ChemSusChem* **4**, 432–449
126. Warren, S. C., Voitchovsky, K., Dotan, H., Leroy, C. M., Cornuz, M., Stellacci, F., Hébert, C., Rothschild, A., Grätzel, M. Identifying champion nanostructures for solar water-splitting. *Nature Materials* **12**, 842–849 (2013).
127. Lee, E.-T., Jang, G.-E., Kim, C. K., and Yoon, D.-H. Fabrication and gas sensing properties of  $\alpha$ -Fe<sub>2</sub>O<sub>3</sub> thin film prepared by plasma enhanced chemical vapor deposition (PECVD). *Sensors and Actuators B: Chemical* **77**, 221–227 (2001).
128. Carraro, G., Gasparotto, A., Maccato, C., Bontempi, E., and Barreca, D. PECVD of Hematite Nanoblades and Nanocolumns: Synthesis, Characterization, and Growth Model. *Chemical Vapor Deposition* **21**, 294–299 (2015).
129. Borrás, A., Sanchez-Valencia, J. R., Widmer, R., Rico, V. J., Justo, A., Gonzalez-Eliphe, A. R. Growth of Crystalline TiO<sub>2</sub> by Plasma Enhanced Chemical Vapor Deposition. *Crystal Growth & Design* **9**, 2868–2876 (2009).

- 
130. Li, D., Goullet, A., Carette, M., Granier, A., Zhang, Y., and Landesman, J. P. Structural and optical properties of RF-biased PECVD TiO<sub>2</sub> thin films deposited in an O<sub>2</sub>/TTIP helicon reactor. *Vacuum* **131**, 231–239 (2016).
131. Tilley, S. D., Cornuz, M., Sivula, K., and Grätzel, M. Light-Induced Water Splitting with Hematite: Improved Nanostructure and Iridium Oxide Catalysis. *Angewandte Chemie International Edition* **49**, 6405–6408 (2010).
132. Zhong, D. K., Cornuz, M., Sivula, K., Grätzel, M., and Gamelin, D. R. Photo-assisted electrodeposition of cobalt–phosphate (Co–Pi) catalyst on hematite photoanodes for solar water oxidation. *Energy & Environmental Science* **4**, 1759–1764 (2011).
133. Deng, J., Zhong, J., Pu, A., Zhang, D., Li, M., Sun, X., and Lee, S.-T. Ti-doped hematite nanostructures for solar water splitting with high efficiency. *Journal of Applied Physics* **112**, 084312 (2012).
134. Wang, D., Chen, H., Chang, G., Lin, X., Zhang, Y., Aldalbahi, A., Peng, C., Wang, J., and Fan, C. Uniform Doping of Titanium in Hematite Nanorods for Efficient Photoelectrochemical Water Splitting. *ACS Applied Materials & Interfaces* **7**, 14072–14078 (2015).
135. Wang, C., Chen, Z., Jin, H., Cao, C., Li, J., and Mi, Z. Enhancing visible-light photoelectrochemical water splitting through transition-metal doped TiO<sub>2</sub> nanorod arrays. *Journal of Materials Chemistry A* **2**, 17820–17827 (2014).
136. Zhang, Z., Hossain, M. F. and Takahashi, T. Photoelectrochemical water splitting on highly smooth and ordered TiO<sub>2</sub> nanotube arrays for hydrogen generation. *International Journal of Hydrogen Energy* **35**, 8528–8535 (2010).
137. Zhang, X., Cui, H., Humayun, M., Qu, Y., Fan, N., Sun, X., Jing, L. Exceptional performance of photoelectrochemical water oxidation of single-crystal rutile TiO<sub>2</sub> nanorods dependent on the hole trapping of modified chloride. *Scientific Reports* **6**, 21430 (2016).
138. Liang, S., He, J., Sun, Z., Liu, Q., Jiang, Y., Cheng, H., He, B., Xie, Z., and Wei, S. Improving Photoelectrochemical Water Splitting Activity of TiO<sub>2</sub> Nanotube Arrays by Tuning Geometrical Parameters. *The Journal of Physical Chemistry C* **116**, 9049–9053 (2012).
139. Fitch, A., Strandwitz, N. C., Brunschwig, B. S., and Lewis, N. S. A Comparison of the Behavior of Single Crystalline and Nanowire Array ZnO Photoanodes. *The Journal of Physical Chemistry C* **117**, 2008–2015 (2013).
140. Kalanur, S. S., Hwang, Y. J., Chae, S. Y., and Joo, O. S. Facile growth of aligned WO<sub>3</sub> nanorods on FTO substrate for enhanced photoanodic water oxidation activity. *Journal of Materials Chemistry A* **1**, 3479–3488 (2013).
141. Kim, H. G., Borse, P. H., Jang, J. S., Ahn, C. W., Jeong, E. D., Lee, J. S. Engineered Nanorod Perovskite Film Photocatalysts to Harvest Visible Light. *Advanced Materials* **23**, 2088–2092 (2011).
142. Li, Z., Lai, X., Wang, H., Mao, D., Xing, C., Wang, D. Direct hydrothermal synthesis of single-crystalline hematite nanorods assisted by 1,2-propanediamine. *Nanotechnology* **20**, 245603 (2009).
143. Cui, X., Liu, T., Zhang, Z., Wang, L., Zuo, S., Zhu, W. Hematite nanorods with tunable porous structure: Facile hydrothermal-calcination route synthesis, optical and photocatalytic properties. *Powder Technology* **266**, 113–119 (2014).
144. Kuang, S., Yang, L., Luo, S., and Cai, Q. Fabrication, characterization and photoelectrochemical properties of Fe<sub>2</sub>O<sub>3</sub> modified TiO<sub>2</sub> nanotube arrays. *Applied Surface Science* **255**, 7385–7388 (2009).

145. Hung, W.-H., Chien, T.-M. and Tseng, C.-M. Enhanced Photocatalytic Water Splitting by Plasmonic  $\text{TiO}_2\text{-Fe}_2\text{O}_3$  Cocatalyst under Visible Light Irradiation. *The Journal of Physical Chemistry C* **118**, 12676–12681 (2014).
146. Peter, L. M. and Wijayantha, K. G. U. Photoelectrochemical Water Splitting at Semiconductor Electrodes: Fundamental Problems and New Perspectives. *ChemPhysChem* **15**, 1983–1995 (2014).
147. Ahmed, M. G., Kretschmer, I. M., Kandiel, T. A., Ahmed, A. Y., Rashwan, R. A., and Bahnemann, D. W. A Facile Surface Passivation of Hematite Photoanodes with  $\text{TiO}_2$  Overlayers for Efficient Solar Water Splitting. *ACS Applied Materials & Interfaces* **7**, 24053–24062 (2015).
148. Shen, S., Li, M., Guo, L., Jiang, J., and Mao, S. S. Surface passivation of undoped hematite nanorod arrays via aqueous solution growth for improved photoelectrochemical water splitting. *Journal of Colloid and Interface Science* **427**, 20–24 (2014).
149. Pujari, S. P., Scheres, L., Marcelis, A. T. M., and Zuilhof, H. Covalent Surface Modification of Oxide Surfaces. *Angewandte Chemie International Edition* **53**, 6322–6356 (2014).
150. Mathur, S., Ganesan, R., Grobelsek, I., Shen, H., Ruegamer, T., and Barth, S. Plasma-Assisted Modulation of Morphology and Composition in Tin Oxide Nanostructures for Sensing Applications. *Advanced Engineering Materials* **9**, 658–663 (2007).
151. Kim, J. Y., Magesh, G., Youn, D. H., Jang, J.-W., Kubota, J., Domen, K., and Lee, J. S. Single-crystalline, wormlike hematite photoanodes for efficient solar water splitting. *Scientific Reports* **3**, 2681 (2013).
152. Kment, S., Schmuki, P., Hubicka, Z., Machala, L., Kirchgeorg, R., Liu, N., Wang, L., Lee, K., Olejnick, J., Cada, M., Gregora, I., and Zboril, R. Photoanodes with Fully Controllable Texture: The Enhanced Water Splitting Efficiency of Thin Hematite Films Exhibiting Solely (110) Crystal Orientation. *ACS Nano* **9**, 7113–7123 (2015).
153. Iandolo, B., Zhang, H., Wickman, B., Zorić, I., Conibeer, G., and Hellman, A. Correlating flat band and onset potentials for solar water splitting on model hematite photoanodes. *RSC Advances* **5**, 61021–61030 (2015).
154. Dang, K., Wang, T., Li, C., Zhang, J., Liu, S., and Gong, J. Improved Oxygen Evolution Kinetics and Surface States Passivation of Ni-Bi Co-Catalyst for a Hematite Photoanode. *Engineering* **3**, 285–289 (2017).
155. Wandelt, K. Photoemission studies of adsorbed oxygen and oxide layers. *Surface Science Reports* **2**, 1–121 (1982).
156. Grosvenor, A. P., Kobe, B. A., Biesinger, M. C., and McIntyre, N. S. Investigation of multiplet splitting of Fe 2p XPS spectra and bonding in iron compounds. *Surface and Interface Analysis* **36**, 1564–1574 (2004).
157. Yamashita, T. and Hayes, P. Analysis of XPS spectra of  $\text{Fe}^{2+}$  and  $\text{Fe}^{3+}$  ions in oxide materials. *Applied Surface Science* **254**, 2441–2449 (2008).
158. Fondell, M., Gorgoi, M., Boman, M., and Lindblad, A. Surface modification of iron oxides by ion bombardment – Comparing depth profiling by HAXPES and Ar ion sputtering. *Journal of Electron Spectroscopy and Related Phenomena* **224**, 23–26 (2018).
159. Moreira, G. F., Peçanha, E. R., Monte, M. B. M., Leal Filho, L. S., and Stavale, F. XPS study on the mechanism of starch-hematite surface chemical complexation. *Minerals Engineering* **110**, 96–103 (2017).
160. Zhu, C., Li, C., Zheng, M., and Delaunay, J.-J. Plasma-Induced Oxygen Vacancies in Ultrathin Hematite Nanoflakes Promoting Photoelectrochemical Water Oxidation. *ACS Applied Materials & Interfaces* **7**,



22355–22363 (2015).

161. Hu, Y., Boudoire, F., Hermann-Geppert, I., Bogdanoff, P., Tsekouras, G., Mun, B. S., Fortunato, G., Grätzel, M., and Braun, A. Molecular Origin and Electrochemical Influence of Capacitive Surface States on Iron Oxide Photoanodes. *The Journal of Physical Chemistry C* **120**, 3250–3258 (2016).
162. Zhang, X., Klaver, P., van Santen, R., van de Sanden, M. C. M., and Bieberle-Hütter, A. Oxygen Evolution at Hematite Surfaces: The Impact of Structure and Oxygen Vacancies on Lowering the Overpotential. *The Journal of Physical Chemistry C* **120**, 18201–18208 (2016).
163. Forster, M., Potter, R. J., Ling, Y., Yang, Y., Klug, D. R., Li, Y., and Cowan, A. J. Oxygen deficient  $\alpha$ -Fe<sub>2</sub>O<sub>3</sub> photoelectrodes: a balance between enhanced electrical properties and trap-mediated losses. *Chemical Science* **6**, 4009–4016 (2015).
164. Yamakata, A., Vequizo, J. J. M. and Kawaguchi, M. Behavior and Energy State of Photogenerated Charge Carriers in Single-Crystalline and Polycrystalline Powder SrTiO<sub>3</sub> Studied by Time-Resolved Absorption Spectroscopy in the Visible to Mid-Infrared Region. *The Journal of Physical Chemistry C* **119**, 1880–1885 (2015).
165. Ruoko, T.-P. Charge Carrier Dynamics in Solar Water Oxidation - Tampere University of Technology. (Tampere University of Technology, 2017).
166. Ruoko, T.-P., Kaunisto, K., Bärtsch, M., Pohjola, J., Hiltunen, A., Niederberger, M., Tkachenko, N. V. and Lemmetyinen, H. Subpicosecond to Second Time-Scale Charge Carrier Kinetics in Hematite–Titania Nanocomposite Photoanodes. *The Journal of Physical Chemistry Letters* **6**, 2859–2864 (2015).
167. Barroso, M., Pendlebury, S. R., Cowan, A. J., and Durrant, J. R. Charge carrier trapping, recombination and transfer in hematite ( $\alpha$ -Fe<sub>2</sub>O<sub>3</sub>) water splitting photoanodes. *Chemical Science* **4**, 2724–2734 (2013).
168. Pendlebury, S. R., Wang, X., Le Formal, F., Cornuz, M., Kafizas, A., Tilley, S. D., Grätzel, M., and Durrant, J. R. Ultrafast Charge Carrier Recombination and Trapping in Hematite Photoanodes under Applied Bias. *Journal of the American Chemical Society* **136**, 9854–9857 (2014).
169. Pendlebury, S. R., Cowan, A. J., Barroso, M., Sivula, K., Ye, J., Grätzel, M., Klug, D. R., Tang, J., and Durrant, J. R. Correlating long-lived photogenerated hole populations with photocurrent densities in hematite water oxidation photoanodes. *Energy & Environmental Science*. **5**, 6304–6312 (2012).
170. Pyeon, M., Ruoko, T.-P., Leduc, J., Goenuellue, Y., Deo, M., Tkachenko, N. V., and Mathur, S. Critical role and modification of surface states in hematite films for enhancing oxygen evolution activity. *Journal of Materials Research* **33**, 455–466 (2018).
171. Zhang, J. and Pan, C. Magnetic-field-controlled Alignment of Carbon Nanotubes from Flames and Its Growth Mechanism. *The Journal of Physical Chemistry C* **112**, 13470–13474 (2008).
172. Luo, C., Fu, Q. & Pan, C. Strong magnetic field-assisted growth of carbon nanofibers and its microstructural transformation mechanism. *Scientific Reports* **5**, 9062 (2015).
173. Zhao, H., Zhang, B., Zhang, J., Zhang, L., Han, X., Xu, P., and Zhou, Y. Field-Assisted Synthesis and Electromagnetic Properties of Aligned Magnetic Nanostructures by  $\gamma$ -Irradiation Induced Reduction. *The Journal of Physical Chemistry C* **114**, 21214–21218 (2010).
174. Hu, H. and Sugawara, K. Magnetic-field-assisted synthesis of Ni nanostructures: Selective control of particle shape. *Chemical Physics Letters* **477**, 184–188 (2009).
175. Xiao, W., Liu, X., Hong, X., Yang, Y., Lv, Y., Fang, J., and Ding, J. Magnetic-field-assisted synthesis

of magnetite nanoparticles via thermal decomposition and their hyperthermia properties. *CrystEngComm* **17**, 3652–3658 (2015).

176. Tamirat, A. G., Rick, J., Dubale, A. A., Su, W.-N., and Hwang, B.-J. Using hematite for photoelectrochemical water splitting: a review of current progress and challenges. *Nanoscale Horiz.* **1**, 243–267 (2016).

177. Wang, M., Wang, H., Wu, Q., Zhang, C., and Xue, S. Morphology regulation and surface modification of hematite nanorods by aging in phosphate solutions for efficient PEC water splitting. *International Journal of Hydrogen Energy* **41**, 6211–6219 (2016).

178. Wei, Q., Wang, Y.-L., Nie, Z.-R., Yu, C.-X., Li, Q.-Y., Zou, J.-X., and Li, C.-J. Facile synthesis of hydrophobic microporous silica membranes and their resistance to humid atmosphere. *Microporous and Mesoporous Materials* **111**, 97–103 (2008).

179. Marmur, A. Wetting on Hydrophobic Rough Surfaces: To Be Heterogeneous or Not To Be? *Langmuir* **19**, 8343–8348 (2003).

180. Sun, C., Ge, L.-Q. and Gu, Z.-Z. Fabrication of super-hydrophobic film with dual-size roughness by silica sphere assembly. *Thin Solid Films* **515**, 4686–4690 (2007).

181. Kosak Söğüt, C., Yilgör, E. & Yilgör, I. Influence of the average surface roughness on the formation of superhydrophobic polymer surfaces through spin-coating with hydrophobic fumed silica. *Polymer* **62**, 118–128 (2015).

182. Niu, Y., Yu, M., Meka, A., Liu, Y., Zhang, J., Yang, Y., and Yu, C. Understanding the contribution of surface roughness and hydrophobic modification of silica nanoparticles to enhanced therapeutic protein delivery. *Journal of Materials Chemistry B* **4**, 212–219 (2015).

183. Ebert, D. and Bhushan, B. Durable Lotus-effect surfaces with hierarchical structure using micro- and nanosized hydrophobic silica particles. *Journal of Colloid and Interface Science* **368**, 584–591 (2012).

184. Jeong, S. A. and Kang, T. J. Superhydrophobic and transparent surfaces on cotton fabrics coated with silica nanoparticles for hierarchical roughness. *Textile Research Journal* **87**, 552–560 (2017).

185. Mota, R. P., Galvão, D., Durrant, S. F., De Moraes, M. A. B., Dantas, S., de O., Cantão, M. HMDSO plasma polymerization and thin film optical properties. *Thin Solid Films* **270**, 109–113 (1995).

186. Vayssieres, L., Beermann, N., Lindquist, S.-E., and Hagfeldt, A. Controlled Aqueous Chemical Growth of Oriented Three-Dimensional Crystalline Nanorod Arrays: Application to Iron(III) Oxides. *Chemistry of Materials* **13**, 233–235 (2001).

187. Shin, H., Okamoto, K., Miyazaki, S., and Hirose, M. Effect of Substrate Bias on Silicon Thin-Film Growth in Plasma-Enhanced Chemical Vapor Deposition at Cryogenic Temperatures. *Japanese Journal of Applied Physics* **31**, 1953 (1992).

## 8 Indices

### 8.1 Figures index

Figure 1 Classification of various CVD processes. ....	7
Figure 2 A typical PEC system consisting of three electrodes showing production of hydrogen and oxygen. ....	20
Figure 3 Illustrations of semiconductor-electrolyte interfaces at stages of (a) before contact, (b) after contact and (c) under illumination. ....	21
Figure 4 A diagram with Young's equation for determination of surface hydrophobicity. ....	24
Figure 5 Contact angle determination on a rough surface in (left) Wenzel's model and (right) Cassie-Baxter model. ....	25
Figure 6 Surface morphologies of the patterned triple photoanode ( $\text{Fe}_2\text{O}_3/\text{TiO}_2/\text{Fe}_2\text{O}_3:\text{FTO}$ ). ....	31
Figure 7 Elemental distributions on the patterned structure; (a) an SEM image of the scanned area, (b) collective elemental distribution of Fe (orange) and Ti (blue), (c) and (d) selective elemental distribution of Fe and Ti, respectively. (Rectangular areas with numbers represent the scanned regions for quantitative analysis in Table 10 and scale bars represent 200 $\mu\text{m}$ .) ....	32
Figure 8 (a) XPS survey spectra of the patterned areas and enlarged spectra of (b) Fe 2p and (c) Ti 2p. ....	34
Figure 9 J-V curves of the prepared photoelectrodes under darkness (dashed lines) and under illumination (solid lines): (a) $\text{Fe}_2\text{O}_3:\text{FTO}$ -black, unpatterned $\text{TiO}_2/\text{Fe}_2\text{O}_3:\text{FTO}$ -green and $\text{Fe}_2\text{O}_3/\text{TiO}_2/\text{Fe}_2\text{O}_3:\text{FTO}$ -purple, (b) $\text{Fe}_2\text{O}_3:\text{FTO}$ -black, patterned $\text{TiO}_2/\text{Fe}_2\text{O}_3:\text{FTO}$ -magenta and $\text{Fe}_2\text{O}_3/\text{TiO}_2/\text{Fe}_2\text{O}_3:\text{FTO}$ -orange, (c) comparison of J-V curves between unpatterned and patterned multilayers, and (d) photocurrent density values at water redox potential of 1.23 V vs. RHE. ....	36
Figure 10 Dependence of $\text{TiO}_2$ thickness on J-V behavior of double/triple photoelectrodes: (a, d) 15 min, (b, e) 30 min and (c, f) 60 min of deposition times for $\text{TiO}_2$ layer. ....	37
Figure 11 SEM images of (a) $\text{Fe}_2\text{O}_3$ -(0 min) $\text{TiO}_2$ , (b) $\text{Fe}_2\text{O}_3$ -(10 min) $\text{TiO}_2$ , (c) $\text{Fe}_2\text{O}_3$ -(30 min) $\text{TiO}_2$ , and (d) $\text{Fe}_2\text{O}_3$ -(60 min) $\text{TiO}_2$ composites (Reproduced from Ref. <sup>106</sup> with permission from The Royal Society of Chemistry). ....	40
Figure 12 J-V characteristics of the core-shell $\text{Fe}_2\text{O}_3$ - $\text{TiO}_2$ composites depending on deposition time of $\text{Ti}[\text{OCH}(\text{CH}_3)_2]_4$ . Pure $\text{TiO}_2$ and $\text{Fe}_2\text{O}_3$ produced by PECVD (30 min) and hydrothermal synthesis, respectively, were also tested as comparisons. ....	41
Figure 13 Upper row: Optical micrographs of (a) pristine hematite and post-treated hematite by oxygen plasma for (b) 10 min, (c) 20 min, and (d) 30 min; Lower row: hematite films post-treated by short annealing (750 $^\circ\text{C}$ for 10 min) after oxygen plasma processes for corresponding duration. Scale bars are 500 nm. ....	44
Figure 14 Surface topography images obtained by AFM and corresponding diagonal line profiles of	

(a) pristine hematite and oxygen plasma treated for (b) 10 min, (c) 20 min and (d) 30 min followed by short annealing. ....	45
Figure 15 Roughness of the prepared hematite films obtained from the diagonal line profiles given in Figure 9. $R_{pv}$ , $R_q$ and $R_a$ refer to peak-valley, root mean square and average roughness values, respectively.....	46
Figure 16 J-V curves of the prepared hematite photoelectrodes treated with (a) oxygen plasma, (b) oxygen plasma followed by short annealing and (c) only short annealing; (d) a graphical demonstration of onset potential (red) and photocurrent density at 1.23 V vs. RHE (blue) based on insets in (a) and (b). ....	47
Figure 17 XRD patterns of the pristine hematite (black), hematite treated with oxygen plasma for 20 min (blue) and oxygen plasma followed by short annealing (red). ....	48
Figure 18 High resolution XPS spectra obtained from the pristine hematite, the oxygen plasma treated hematite and the hematite treated with oxygen plasma followed by short annealing of (a) Fe 2p and (b, c and d) O 1s. ....	49
Figure 19 Transient absorption decays at an applied voltage of 1.50 V vs. RHE, probed (a) at 575 nm and (b) at 650 nm.....	52
Figure 20 J-V curves of the hematite photoanodes that were treated with Ar plasma for (a) 10 min, (b) 20 min and (c) 30 min followed by short annealing. ....	53
Figure 21 High resolution XPS spectra of the post-treated hematite photoanodes with Ar plasma. ...	54
Figure 22 Photographs of the plasma generated under (a) the attractive field and (b) the repulsive field, induced by rod-type magnets. ....	58
Figure 23 Hematite films coated on FTO substrates from different parameters, including applied magnetic fields and deposition time and corresponding surface morphologies of the selected films.....	59
Figure 24 J-V curves plotted as a function of (a) magnetic fields at a fixed deposition time and (b) deposition times under specific magnetic fields.....	60
Figure 25 Photocurrent density values (at 1.23 V vs. RHE) of the prepared hematite films.....	60
Figure 26 Surface morphologies of the hematite films deposited for 2 min (a) without magnets, (b) under the attractive field and (c) under the repulsive field. ....	61
Figure 27 Surface morphologies of the hematite films deposited under (a) attractive field and (b) repulsive field with deposition time of 5 min; Tilted side view images of the films under the repulsive field for (c) 2 min and (d) 5 min. ....	62
Figure 28 XRD patterns of the hematite films deposited for 2 min under different magnetic fields. Asterisks (*) represent $\text{SnO}_2$ (PDF 41-1445) from FTO substrates. ....	63
Figure 29 A photograph of an experimental setup using stacked disk-type magnets with samples placed at different positions and an inset illustrating the expected magnetic flux lines.....	64
Figure 30 Surface morphologies of the hematite films deposited on Si wafers (a) without magnets, (b) at P0 and (c) at P1.....	64

Figure 31 Crystallinity of the hematite films prepared with a stack of disk-type magnets.....	65
Figure 32 J-V curves obtained from hematite films synthesized with (a) the magnet stack and (b) Al block. ....	66
Figure 33 Determination of magnetic field strength using the magnetometer where (a and b) the attractive force and (c and d) the repulsive force exist between the magnet stacks. ....	67
Figure 34 (a) A photograph taken during a PECVD process with the set of magnet stacks and (b) a simplified scheme of the expected magnetic flux lines. ....	68
Figure 35 Surface morphologies of the hematite films prepared on FTO substrates under different plasma environment, formed by the designed configuration with magnet stacks; (a) without magnets, (b) under the attractive field and (c) under the repulsive field. ....	68
Figure 36 XRD patterns of the films prepared with the set of the magnet stacks.....	69
Figure 37 PEC performances of the prepared hematite with the set of the magnet stacks. ....	70
Figure 38 (upper row) Illustration of PECVD process under various conditions and (lower row) optical images of the prepared SiO <sub>x</sub> coatings on silicon wafers.....	71
Figure 39 Cross-section images of the SiO <sub>x</sub> coatings deposited (a) without magnets, (b) under the attractive field, (c) under the repulsive field, and (d) using one stack of magnets. ....	71
Figure 40 Surface topographical images and roughness values (R <sub>a</sub> and R <sub>q</sub> ) obtained by AFM; (a) the reference SiO <sub>x</sub> film, SiO <sub>x</sub> films deposited (b) under the attractive field, (c) under the repulsive field, and (d) on the magnet stack (P0). ....	73
Figure 41 Graphical illustration of atomic concentration and calculated atomic ratio of C/O. ....	75
Figure 42 Demonstration of wetting behavior of the SiO <sub>x</sub> coated fabric mats; (a) as-received fabric, (b) fabric coated with SiO <sub>x</sub> under no magnetic field and (c) fabric coated with SiO <sub>x</sub> under the magnetic field (P0). Insets are images obtained by contact angle measurement.....	76
Figure 43 Summary of the works for producing photoelectrode materials for PEC water splitting....	86

## 8.2 Schemes index

Scheme 1 Complex interplay of material properties and device integration in the development of new materials for photoelectrochemical water splitting (PEC-WS) reactions.....	2
Scheme 2 An illustration of a typical thermal CVD system. ....	6
Scheme 3 A scheme of reactive species generated in plasma.....	9
Scheme 4 A schematic procedure of the preparation steps to fabricate a patterned Fe <sub>2</sub> O <sub>3</sub> -TiO <sub>2</sub> multilayer with inset presenting a photograph of the Fe <sub>2</sub> O <sub>3</sub> //TiO <sub>2</sub> //Fe <sub>2</sub> O <sub>3</sub> :FTO photoelectrode. ....	30
Scheme 5 Illustrations of side views during the processes, describing imperfect isolation of (a) the second (TiO <sub>2</sub> ) and (b) the third (Fe <sub>2</sub> O <sub>3</sub> ) layers which resulted in existence of elements on neighboring area. ....	33

Scheme 6 Proposed charge transfer schemes through interface in bi-layer structures of $\text{TiO}_2/\text{Fe}_2\text{O}_3:\text{FTO}$ depending on thickness of $\text{TiO}_2$ layer and overpotential.....	38
Scheme 7 Proposed charge transfer schemes through interface in triple-layer structures of $\text{Fe}_2\text{O}_3/\text{TiO}_2/\text{Fe}_2\text{O}_3:\text{FTO}$ depending on thickness of $\text{TiO}_2$ layer and overpotential value....	38
Scheme 8 A schematic process to prepare 1D heterostructure of $\text{Fe}_2\text{O}_3\text{-TiO}_2$ photoelectrode.....	39
Scheme 9 A simplified model depicting formation of $\text{Fe}_2\text{O}_3\text{-TiO}_2$ core-shell composites.....	40
Scheme 10 A proposed scheme of the hematite surface during the post-treatments based on XPS analyses. ....	50
Scheme 11 Illustrations of the experimental setups for PECVD processes, employing (a) rod-type and (b) disk-type magnets. ....	57
Scheme 12 An illustration of the setup that utilized to apply magnetic fields in PECVD process. Rod-type magnets were used.....	80
Scheme 13 An experimental setup designed to utilize the rod-type magnets in PECVD; (left and right) enlarged graphics that depict the chamber electrode with the magnet support and the outer apparatus for feeding the precursor, respectively, and (middle) a feature of the reaction chamber. ....	80

### 8.3 Tables index

Table 1 A comparison list of various techniques applied for fabrication of thin films.....	3
Table 2 Classification of ionization processes in plasma (An atomic radical is presented as $\text{A}^*$ ). ....	10
Table 3 Dissociation mechanisms of neutral molecules. ....	12
Table 4 Various applications of PECVD functional coatings (adapted from Ref. <sup>19</sup> ).....	14
Table 5 Various DLC coatings produced by PECVD.....	15
Table 6 Silicon carbide films prepared by PECVD. ....	16
Table 7 A list of metal oxides synthesized by wet-chemical processes for applications. ....	18
Table 8 Metal oxides synthesized by various methods for PEC water splitting with their performances. ....	22
Table 9 Metal oxides synthesized by PECVD for obtaining hydrophobic surfaces. ....	27
Table 10 Quantitative analysis of elemental distributions on the patterned area (Rectangular areas with numbers in Figure 7) obtained by EDS. ....	33
Table 11 Calculated deposition rates of the $\text{SiO}_x$ coatings under various conditions.....	72
Table 12 Static water contact angles obtained from the various $\text{SiO}_x$ coatings (amount of water droplet, 2 $\mu\text{L}$ ).....	74
Table 13 Elemental quantifications of XPS survey spectra obtained from the prepared $\text{SiO}_x$ films and	

calculated atomic ratios. ....	74
Table 14 Working parameters of the chamber pressure (Pa) and the r.f. bias (V) in PECVD of Fe(CO) <sub>5</sub> under various conditions. ....	81





## 9 Appendix

### 9.1 Abbreviations (in order of appearance)

PECVD	plasma enhanced chemical vapor deposition
PEC	photoelectrochemical
RHE	reversible hydrogen electrode
XPS	X-ray photoelectron spectroscopy
TAS	transient absorption spectroscopy
XRD	X-ray diffraction
HMDSO	hexamethyldisiloxane
AFM	atomic force microscopy
PVD	physical vapor deposition
MPCVD	microwave plasma-assisted CVD
RPECVD	remote plasma enhanced CVD
APCVD	atmospheric pressure CVD
LPCVD	low-pressure CVD
UHVCVD	ultrahigh vacuum CVD
AACVD	aerosol-assisted CVD
DLICVD	direct liquid injection CVD
PACVD	plasma-assisted CVD
EEDF	electron energy distribution function
AC	alternating current
MW	microwave
RF or r.f.	radio frequency
DLC	diamond-like carbon
LED	light-emitting diode
MEMS	micro-electomechanical systems
DFT	density functional theory

---

IGZO	Indium-gallium-zinc-oxide
1(2, 3) D	1(2, 3)-dimensional
FTO	fluorine doped tin oxide
PC	polycarbonate
EDS	energy dispersive X-ray spectroscopy
SEM	scanning electron microscopy
OER	oxygen evolution reaction
WCA	water contact angle
PVP	polyvinylpyrrolidone
WE	working electrode
RE	reference electrode
CE	counter electrode

## 9.2 Lebenslauf

Personliche Daten	
<ul style="list-style-type: none"> <li>• <b>Name:</b></li> <li>• <b>Geburtsdatum und ort:</b></li> <li>• <b>Staatsangehörigkeit:</b></li> <li>• <b>Familienstand:</b></li> <li>• <b>Contact:</b></li> </ul>	<p>Myeongwhun Pyeon  12. 12. 1985 / Yeonggwang  Koreanisch  Ledig  admiremh@gmail.com</p>
Bildungsweg	
<ul style="list-style-type: none"> <li>• <b>Master of Science (MSc):</b> Materials Science and Engineering (Inha University, Incheon, Republic of Korea, Mar. 2012-Feb. 2014)  <i>Thesis title: Syntheses of hollow silica spheres and composites encapsulating secondary materials in hollow silica spheres; In water-in-oil microemulsion solution through sol-gel reaction</i></li> <li>• <b>Bachelor of Science (BSc):</b> Materials Science and Engineering (Inha University, Incheon, Republic of Korea, Mar. 2004-Feb. 2011)</li> <li>• <b>Jeonnam Science High school:</b> Naju, Jellanam-do, Süd Korea, Mar. 2001-Feb. 2004</li> </ul>	
Erfahrung	
<ul style="list-style-type: none"> <li>• <b>Research assistant</b> at Surface Treatment R&amp;D Group, Korea Institute of Industrial Technology (KITECH, Sep 2011-Feb 2012)</li> <li>• <b>Military service</b> at Republic of Korea Army, 35 Division, Jeonju, Jeollabukdo, Republic of Korea (Feb 2005-Feb 2007)</li> </ul>	

## 9.3 Publication list

- 1) **\*Constructing Fe<sub>2</sub>O<sub>3</sub>/TiO<sub>2</sub> core-shell photoelectrodes for efficient photoelectrochemical water splitting**, M. Wang, M. Pyeon, Y. Goenuellue, A. Kaouk, S. Shen, L. Guo, S. Mathur, *Nanoscale* 2015, 7, 10094.
- 2) **Chapter 23. Perspectives of Nanostructured Metal Oxides and Their Heterostructures in Photoelectrochemical Water Splitting for Solar Hydrogen Production**, in *Engineered Ceramics: Current Status and Future Prospects* (Editors: T. Ohji and M. Singh), The American Ceramic Society and John Wiley & Sons 2015, Part 4, 457.
- 3) **\*Design of multi-layered TiO<sub>2</sub>-Fe<sub>2</sub>O<sub>3</sub> photoanodes for photoelectrochemical water splitting: patterning effects on photocurrent density**, M. Pyeon, M. Wang, Y. Gönüllü, A. Kaouk, S. Jäckle, S. Christiansen, T. Hwang, K. Moon, S. Mathur, *MRS Communications* 2016, 6, 442.
- 4) **High Water-Splitting Efficiency through Intentional In and Sn Codoping in Hematite Photoanodes**, A. Kaouk, T.-P. Ruoko, M. Pyeon, Y. Gönüllü, K. Kaunisto, H. Lemmetyinen, S. Mathur, *J. Phys. Chem. C* 2016, 120, 28345.
- 5) **Subvalent Iridium Precursors for Atom-Efficient Chemical Vapor Deposition of Ir and IrO<sub>2</sub> Thin Films**, L. Jürgensen, M. Frank, M. Pyeon, L. Czympiel, S. Mathur, *Organometallics* 2017, 36, 2331.
- 6) **\*Critical role and modification of surface states in hematite films for enhancing oxygen evolution activity**, M. Pyeon, T.-P. Ruoko, L. Jennifer, Y. Gönüllü, M. Deo, N. V. Tkachenko, S. Mathur, *J. Mater. Res.* 2018, 33, 455.
- 7) **Trace Amount of Platinum Supported on Carbonized Biomorphic Wood for Efficient Electrochemical Hydrogen Evolution in Alkaline Condition**, M. Wang, Y. Gönüllü, M. Pyeon, Z. Diao, L. Czympiel, M. Singh, S. Shen, S. Mathur, *ChemistrySelect* 2018, 3, 2140.

\*Works in Chapter 2 have been published in *MRS Communicaitons* (3) and *Nanoscale* (1).  
 Works in Chapter 6 have been published in *Journal of Materials Research* (6).

---

#### 9.4 Presentations

- 1) (Oral) **Structural effect of TiO<sub>2</sub>-Hematite multilayer anode on water splitting efficiency fabricated by PECVD**, M. Pyeon, Y. Goenuellue, A. Kaouk, T. Hwang, K. Moon, S. Mathur, *ICACC 2015*, Florida, USA, 25/01-30/01.
- 2) (Oral) **Effect of multi-structured layer consisting of TiO<sub>2</sub> and hematite ( $\alpha$ -Fe<sub>2</sub>O<sub>3</sub>) on photoelectrochemical (PEC) performance using PECVD**, M. Pyeon, Y. Gönüllü, A. Kaouk, T. Hwang, K. Moon, S. Mathur, *MCARE 2015*, Jeju, S. Korea, 24/02-27/02.
- 3) (Poster) **Macro- and Microscopic Modification of Photoanodes for Enhanced Photoelectrochemical Performance via PECVD process**, M Pyeon, M. Wang, T.-P. Ruoko, Y. Gönüllü, S. Mathur, *AMAES NANOmed 2016*, 01/09-02/09.
- 4) (Oral) **Investigation of Post treatments on Hematite Photoanodes for Enhanced Photoelectrochemical (PEC) Water Splitting: Control of Morphology, Surface states and Charge carrier behavior**, M. Pyeon, M. Wang, T.-P. Ruoko, Y. Goenuellue, S. Mathur, *MRS Fall Meeting 2016*, Boston, USA, 27/11-02/12.
- 5) (Poster) **Improving water splitting efficiency of PECVD hematite via magnetic fields**, M. Pyeon, M. Guersoy, Y. Goenuellue, S. Mathur, *AMAES NANOmed 2017*, 05/07-07/07.
- 6) (Poster) **Critical role and modification of surface states in PECVD hematite films for improving oxygen evolution reaction**, M. Pyeon, T.-P. Ruoko, J. Leduc, Y. Goenuellue, M. Deo, Nikolai V. Tkachenko, S. Mathur, *ISEPD 2018*, Jaipur, India, 21/02-24/02.



## Erklärung

Ich erkläre, dass ich die Dissertation mit bestimmten Ratschlägen zur Übersetzung von Kurzfassung und Erklärung allein erstellt habe. Verweise im Text wurden korrekt zitiert und Berechtigungen aus Journalen wurden erhalten, wenn der Inhalt ohne Änderung verwendet wurde. Diese Dissertation ist originell und wurde nicht an anderen Fakultäten oder Universitäten für Prüfungen eingereicht. Mit Ausnahme der in den oben genannten Zeitschriften veröffentlichten Arbeiten (siehe 9.3) ist in dieser Dissertation keine Veröffentlichung mit Inhalten vorgesehen. Dem Autor ist das Bestimmungsprotokoll der Promotionsordnung bekannt.

---

(Myeongwhun Pyeon